

ABSTRACT

Title of Document: KINEMATICS OF THE MAYFLY NYMPH
GILL ARRAY: AN INTERMEDIATE
REYNOLDS NUMBER VENTILATION
PUMP

Andrew T. Sensenig, Doctor of Philosophy 2009

Directed By: Dr. Jeffrey Shultz, Department of Entomology
Dr. Kenneth Kiger, Department of Mechanical
Engineering

Abstract:

Comparative studies encompassing a wide range of aquatic animals have shown that rowing is exclusively used at low Reynolds numbers ($Re < 1$) while flapping is predominantly used at $Re > 100$, but few studies have been undertaken to document the transition in individual species that traverse the intermediate Re regime using a single set of appendages. Thus, it is not generally known whether a gradual increase in Re within a system results in a gradual or sudden shift between rowing and flapping. Here I document both the kinematics of the appendages and the surrounding fluid of a nymphal mayfly *Centroptilum triangulifer* that uses a serial array of seven pairs of abdominal gill plates and operates at Reynolds numbers ranging from 2-22 during ontogeny. I found that some kinematic variables (stroke frequency and metachronal phase lag) did not change during ontogeny but that others changed substantially. Specifically, gills in small instars used strokes with large pitch

and stroke-plane deviations, while larger instars used strokes with minimal pitch and minimal stroke-plane deviation. Gills in larger instars also acquired an intrinsic hinge that allowed passive asymmetric movement between half strokes. Net flow in small animals was directed ventrally and essentially parallel to the stroke plane (i.e. rowing), but net flow in large animals was directed dorsally and essentially transverse to the stroke plane (i.e. flapping). The metachronal phasing of the gills produced a time-dependent array of vortices associated with a net ventilatory current, a fluid kinematic pattern here termed a “phased vortex pump”. Significantly, absolute vortex size did not change with increasing animal size or Re , indicating that the vortex diameter (L_v) decreased relative to intergill spacing (L_{is}) during mayfly growth. Given that effective flapping requires organized flow between adjacent appendages, I proposed the hypothesis that rowing should be favored when $L_{is} / L_v < 1$ and flapping should be favored when $L_{is} / L_v > 1$. Significantly, the rowing-to-flapping transition in *Centroptilum* occurs at $Re \sim 5$, when maximum dynamic intergill distance equals vortex diameter. This result suggests that the Re -based rowing-flapping demarcation observed in a wide array of aquatic organisms is determined by the relative size of the propulsive mechanism and its self-generated vortices.

KINEMATICS OF THE MAYFLY NYMPH GILL ARRAY: AN INTERMEDIATE
REYNOLDS NUMBER VENTILATION PUMP

By

Andrew T. Sensenig

Dissertation submitted to the Faculty of the Graduate School of the
University of Maryland, College Park, in partial fulfillment
of the requirements for the degree of
Doctor of Philosophy
2009

Advisory Committee:
Professor Jeffrey Shultz, Chair
Professor Kenneth Kiger, Co-Chair
Professor William Lamp
Professor Elias Balaras
Dr. Brent Kent

© Copyright by
Andrew T. Sensenig
2009

Foreword

Chapter 2 of this dissertation was previously published as:
Sensenig, A. T., J. W. Shultz, and K. Kiger. in press 2009. The rowing-to-flapping transition: ontogenetic changes in gill-plate kinematics in the nymphal mayfly *Centroptilum triangulifer* (Ephemeroptera, Baetidae). *Biological Journal of the Linnean Society*.

The student, Andrew Sensenig, made substantial contributions to all aspects of the publication, justifying its inclusion in this dissertation.

Acknowledgements

I thank David Funk at the Stroud Water Research Center for supplying animals, James Duncan (Dept. of Mechanical Engineering, University of Maryland) for the use of high-speed camera equipment, and Charles Mitter (Dept. of Entomology, University of Maryland) for the use of microscopes. This work was supported by the Gahan Scholarship Fund (Dept. of Entomology, University of Maryland) and a grant from the National Science Foundation (CBET 0730907).

Table of Contents

Foreword.....	ii
Acknowledgements.....	iii
Table of Contents.....	iv
List of Tables.....	vi
List of Figures.....	vii
1.A. Problem and Objectives: Explaining Kinematic Transitions at Intermediate Reynolds numbers ($Re = 1-100$).....	1
1.B. Model system and Measurement Techniques.....	4
1.B.1. Previous work on gill arrays in nymphal mayflies.....	4
1.B.2. <i>Centroptilum triangulifer</i>	6
1.B.3. 3-D stroke kinematic measurement.....	8
1.B.4. Flow measurement through Particle Image Velocimetry.....	9
1.C. Objective and Scope of this Study.....	11
1.D. Conclusions from this Thesis.....	12
1.E. Background: Hydrodynamics of oscillating appendages.....	15
1.E.1. Influence of Reynolds number on flow behavior.....	15
1.E.2. Basic division of kinematics: Rowing vs. flapping.....	15
1.E.3. Vorticity: definition and why it is a useful description.....	17
1.F. Review of stroke mechanics and mechanisms.....	19
1.F.1. Drag-based mechanisms.....	19
1.F.2. Lift-based mechanisms:.....	21
Chapter 2: Gill-plate stroke kinematics.....	27
2.A Introduction.....	27
2.B Materials and Methods.....	30
2.B.1 Study organism and cinematography.....	30
2.B.2 Experimental set up.....	31
2.B.3 Gill-plate kinematics.....	35
2.B.4 Gill-plate morphology.....	39
2.C Results.....	39
2.C.1 Generalized kinematics of the gill array.....	39
2.C.2 Kinematics specific to nymphs with $Re_f < 5$	41
2.C.4 Gradual and abrupt changes between $Re_f > 20$ (large) and $Re_f < 5$ (small) nymphs.....	46
2.C.5 Morphological results.....	48
2.D. Discussion.....	50
2.D.1 Gill oscillation frequency scaling.....	54
2.D.2 The significance of the gill hinge in <i>Centroptilum</i>	55
Chapter 3: Phase resolved flow fields and the rowing to flapping transition.....	58
3.A. Introduction.....	58
3. B. Materials and Methods.....	62
3.B.1 Nymph preparation.....	62
3.B.2 PIV implementation and gill tracking.....	63

3.B.3 Hydrodynamic definitions.....	67
3.B.4 Vorticity and circulation calculation.....	69
3.B.5 Inter-gill sectional flux and time-averaged array flux calculation.....	72
3.B.6 Statistical treatment of gill flow characteristics.....	73
3.C. Results.....	74
3.C.1 General observations and steady flow field.....	74
3.C.2 Unsteady flow structure.....	78
3.C.3 Gill circulation history.....	84
3.C.4 Inter-gill sectional flux.....	86
3.D. Discussion.....	90
3.D.1 Phased vortex pump.....	90
3.D.2 Potential shift in component dynamic mechanisms over ontogeny.....	100
3.D.3 Implications of specialization for ventilation.....	103
Chapter 4: Conclusion.....	106
List of symbols.....	108
Bibliography.....	111

List of Tables

Table 1. Size and plate kinematic data of all nymphs examined.

Table 2. Fluid kinematic parameters of all nymphs examined.

List of Figures

Figure 1. The length of locomotory appendages plotted against their respective Reynolds numbers to show the wide range of biologically relevant Re numbers, in addition to several examples of human made machines. Mayfly nymphs operate within what is typically denoted as the intermediate Re regime.

Figure 2. Schematic illustration of the kinematic distinction between flapping and rowing type motions (after Walker and Westneat, 2000).

Figure 3. Intermediate ontogenetic stage nymph of *Centroptilum triangulifer*. Photograph courtesy David Funk.

Figure 4. Spatial axes and angles used in characterizing gill-plate kinematics in the nymphal mayfly.

A. Diagrammatic mayfly nymph from an oblique lateral perspective showing spatial coordinates relative to the body (\hat{x} , anterior-posterior axis; \hat{y} , transverse axis; \hat{z} , dorsal-ventral axis) and parallel coordinates originating at the gill root (x, y, z).

B-C. Key kinematic parameters. The stroke plane (SP) for each cycle - indicated in blue - is defined by three points: the gill root and the anterior and posterior extrema of the gill mid-hinge point. The orientation of the SP is defined by the stroke plane inclination angle (β), measured between the SP and the horizontal (x - y) plane within a mutually orthogonal plane, and the stroke plane lateral offset angle (ϵ), which indicates where the SP crosses the horizontal (x - y) plane. The instantaneous position of the mid-chord point (path indicated by the red curve) is then given by the combination of the stroke angle, Φ , and stroke plane deviation, θ , which measures the angular displacement along and normal to the SP , respectively. The stroke angle origin ($\Phi = 0$) is reference to the position where the SP intersects the transverse-vertical (y - z) plane, and the respective posterior/anterior excursion limits are given by $\Phi_{\min} / \Phi_{\max}$. The orientation of the gill plate is referred to as the pitch, α , which is defined as the angle between the gill plate and the SP , as measured in a mutually orthogonal plane.

D. Gills in larger nymphs have a distinct transverse hinge flex line. The hinge angle, γ , is defined as the deflection of the distal gill plate (flap) from the nominally planar configuration. The hinge angle is positive when the hinge is flexed posteriorly and negative when flexed anteriorly.

Figure 5. Example of the flow field reconstruction possible through ensemble correlation. Vectors (arrows in black) were calculated at every 16 pixels, for 102x75 vectors in full field. Shown is one frame within a sequence of 34 frames required to complete one array oscillation cycle. Vortices were identified automatically in each frame, with blue outline indicating negative (clockwise) vortices and red indicating positive (counter-clockwise) vortices.

Figure 6. Plot showing the relationship between vortex size (dark squares) and measures of intergill spacing. The hypothesis generated here maintains that the

organized intergill flow required for effective flapping can only occur when the diameter of self-generated vortices is smaller than the intergill spacing. Significantly, the vortices do not change absolute size during mayfly growth and intergill spacing exceeds vortex size at $Re \sim 6$. This value corresponds to the Re at which mayfly nymphs transition from rowing to flapping.

Figure 7.

- A. Ratio of gill 4 (width/height).
- B. Gill 4 surface area as a function of gill length.

Figure 8.

Kinematic parameters for gill 4 (brown) and gill 5 (orange) over a stroke cycle. Initiation of retraction of gill 4 marks time=0 ms. Stroke angle angular velocity is negative during retraction. Re_c number is that associated with the space between the gill indicated and its posterior partner. Thin lines represent individual strokes, while thick or dotted line represent mean of individual strokes ($n=4$). Curved green arrows represent the mean flow at that phase, while straight red arrows indicate gill velocity at that phase.

A-F. $Re=2.3$

G-L. $Re=21.6$.

Figure 9.

A-F. Mean kinematic parameters for gill 4 plotted as a function of frequency Re number (Re_f) for nine individuals. Means were determined from 4 strokes; error bars indicate ± 2 S.D. Extrema indicated by red error bars occurred entirely during protraction; extrema indicated by black error bars occurred entirely during retraction; extrema indicated by blue error bars occurred at various points in the stroke and were not limited to either protraction or retraction.

Figure 10.

Volumetric sweep rate, defined as $VSR = [A_{prox} \mathbf{n}_{prox} + A_{flap} \mathbf{n}_{flap}] \cdot \mathbf{v}$, where A and \mathbf{n} are the plan area and unit normal vectors of the gill plate sections (*proximal* and *distal flap*) and \mathbf{v} is the mid-span velocity of the gill. The inset figures on the left show the orbital trajectories of the gill relative to the stroke plane for three different Re_f cases. The orientation of the gill is indicated by the thin line, while the size of the red arrow gives the magnitude of the VSR at the indicated position. The graph on the right depicts a VSR as a function of stroke angle for each of the three cases given. Each case is normalized by its respective maximum VSR magnitude to facilitate relative comparison in stroke symmetry.

Figure 11.

A. Flow field through and around the gill array in the vertical plane quantified by ensemble correlation PIV for $Re_f=20.2$. Mean gill positions over a stroke cycle for gills 1-7 and abdomen outline shown by solid black lines. Gill 4 protraction and retraction maximal positions shown for both the proximal and distal plates as dotted lines.

B. Flow field through and around the gill array in the vertical plane quantified by ensemble correlation PIV for $Re_f=2.3$. Mean gill positions over a stroke cycle for gills 1-7 and abdomen outline shown by solid black lines. Gill 4 extreme protraction and retraction positions shown as dotted lines. There is no measurable flexion about a hinge in any of the gill plates at this Re_f .

Figure 12.

Change in flow direction as a function of Re_f for 13 individuals. Mean flow direction was calculated as the average of the flow over the entire imaged area. A 90 degree angle is expected for an idealized flapping stroke, and a 0 degree angle for an idealized rowing stroke. Flow angle increases with Re_f ($r^2=0.76$, $F_{1,7}=22$, $p=0.002$, linear regress on $Re_f < 12.3$), ($r^2=0.37$, $F_{1,11}=6.3$, $p=0.03$, linear regress on all Re_f). (5/9 individuals from the 3D kinematics study were included in this graph (Re_f 2.1, 8.4, 12.2, 20.2, and 21.6). The remaining individuals (8/13) depicted were collected from the wild.

Figure 13.

A.,D. Mean vertical and horizontal flow field at $Re_f=21.6$

B.,E. Mean vertical and horizontal flow field at $Re_f=6.3$, smaller resolution camera and vector spacing, total field 52x52 vectors.

C. Mean horizontal flow field at $Re_f=2.3$, total field is 105x75 vectors.

Figure 14. Vorticity at phase $t/T=0$ in small nymph $Re=2.7$. Each posterior gill is 0.25 period phase leading anterior gill. Gill bars are white, except gill 4 denoted by black bar. Individual vortices indicated by their dorsal or ventral position and protraction or retraction phase. Ventral induced flow (V) into gill 4 and 5 interspace as gill 5 retracts. Dorsal induced flow is much lower in magnitude (D). High counterclockwise circulation produced by gill 5 retraction (DR5).

Figure 15. Vorticity at phase $t/T=0$ in large nymph $Re=20$. Individual vortices indicated by their dorsal or ventral position and protraction or retraction phase. Important fluid jet/jets indicated by large arrows. Gill 6 is midway through protraction (phase 0.6 for that gill), gill 5 is ending retraction and negative vortex VR5 is moving from proximal to distal plate (phase 0.3). Gill 4 has just begin retraction, and is generating a new negative vortex (VR4) at its leading edge. Gill 3 is nearing end of protraction, and positive (counter-clockwise) vortex VP3 is moving from proximal to distal plate. Gill 2 is midway through protraction, and in approximate synchrony with gill 6. The flow in the interspace of gill 1-2 is approximately in phase with that through interspace 5-6, producing a dorsal jet D from both spaces. Lines through which intergill flux was tracked over the cycle shown as dashed lines, and labeled lower case d(dorsal),m(middle),and v(ventral).

Figure 16. Phase resolved flow at $Re_f=21.6$. Vertical plane images (left column of each double column) and horizontal plane images are shown at ~ 3 ms intervals, with the dimensionless time (t/T) also indicated for each frame. The period was slightly

longer (35 vs 29 ms) in the horizontal imaging of the array, as the animal changed frequency in the several minutes between image capture.
 Figure 17. Phase resolved vertical plane flow at $Re_f=2.3$. Only vertical plane flow was imaged at individuals so small that $Re_f < 5$.

Figure 18. A-B. Vertical plane circulation history of positive and negative vortices at 3 representative Re_f . Time is plotted as fraction of period T . Retraction occurs rapidly over about 0-0.35 t/T in the smaller nymphs, but over 0-0.5 t/T in the large nymphs. The retraction and protraction phases are thus approximately equal length in the largest nymphs. A normalized and unitless value of circulation ($\Gamma/(L_g^2/f)$), where Γ is circulation of the vortex, L_g is gill length, and f is plate oscillation frequency is plotted for comparison of different size nymphs generating 10 fold range in maximum absolute circulation (0.3-3 mm^2/s). Curves denote the mean \pm 1 St.D of gills 2,3,4,5 ($n=4$).

Figure 19.A. Dorsal and ventral vortex p:r circulation ratio as function of Re_f . The p:r ratio is the maximum circulation achieved by the vortex at the designated location over protraction divided by the maximum achieved over retraction. Rowing mechanics of the small nymphs are indicated by the lower p:r ratio.
 B. Flux magnitude as function of Re_f . The influx is defined as the sum of all incoming vectors on the control box drawn in Figure 17-18. The outflux is defined as the sum of all outflowing vectors of the control box. Flux is standardized by the insect volume, showing that flow per volume can vary approximately 5 fold over ontogeny, but is not dependent on ontogenetic stage.

Figure 20. A-C. Vertical plane intergill flux history at 3 representative Re_f and through dorsal, mid, and ventral apertures. Period was normalized to 30 ms for comparison. 1-15 ms is approximately retraction, 15-30 ms is protraction. A normalized and unitless value of flux ($\text{flux}/(L_g^2/f)$), where flux is the flux through the gill interspace, L_g is gill length, and f is plate oscillation frequency is plotted for comparison of different size nymphs generating 14 fold range in maximum absolute intergill flux (0.45-6.2 mm^2/s). The lower normalized intergill flux for the intermediate Re_f case ($Re=6.3$) may correlate with higher horizontal flow rates at this stage. Curves denote the mean \pm 1 St.D of gill interspaces 2,3,4,5 ($n=4$).

Figure 21. Figure 22. The time-averaged array flux through control volume at $Re_f=2.3$. Blue vectors at control volume edge indicate outflow, while red vectors at the control volume edge indicate inflow. The stroke plane of gill plates 2-6 is indicated by the green line, with the mean flow vector over control volume as the thick black vector. The mean flow angle is the angle between the mean flow vector and the mean stroke plane.

Figure 23. Gill plate oscillation frequency as a function of Reynolds number (left) and gill 4 length (right). Each point represents an individual animal. The data-set represents an approximately equal sampling of wild and lab reared nymphs.

Figure 24. Isosurface of positive (red) and negative (blue) vorticity as a function of x - z - t for $Re_f=21.6$. Surface value corresponds to $|\omega_y|=0.2(\omega_y)_{\text{max}}$. Gills are shown at each

instant in the cycle as a gray line, with black (red for gill 4) used for the last slice in the section. The “endcap” of the surface shows the vorticity magnitude at the given instant in the cycle. A. complete section ending at $t/T = 1$; B. slice depicting $t/T = 0.07$; C. slice depicting $t/T = 0.31$; D. slice depicting $t/T = 0.52$; E. slice depicting $t/T = 0.75$. The inset shows the stroke position of gill 4 and 5, with a green bar indicating the phase of the cycle.

Figure 25. Isosurface of positive (red) and negative (blue) vorticity as a function of x - z - t for $Re_f = 1.8$. Surface value corresponds to $|\omega_y| = 0.2(\omega_y)_{\max}$. Gills are shown at each instant in the cycle as a gray line, with black (red for gill 4) used for the last slice in the section. The “endcap” of the surface shows the vorticity magnitude at the given instant in the cycle. A. Complete section ending at $t/T = 1$; B. slice depicting $t/T = 0.04$; C. slice depicting $t/T = 0.2$; D. slice depicting $t/T = 0.4$; E. slice depicting $t/T = 0.69$; E. slice depicting $t/T = 0.86$. The inset shows the stroke position of gill 4 and 5, with a green bar indicating the phase of the cycle.

Figure 26. Array derived rowing kinematics. Results from 3D kinematics demonstrate the concerted rowing due to the combination of high retraction speeds and metachronal phase lag at low Re ($Re=2.3$)(right column), but absence or less evidence of this feature at higher Re (left column). Top plots are the x location (dorsal-ventral axis) of the gill tip motion. Bottom plots are the y location (anterior-posterior axis) of the gill tip motion. Only during protraction at low Re can more than 2 adjacent gills be identified as moving together in a common direction (pink shaded time). At this phase, shared vorticity is prominent across the adjacent gills.

Chapter 1: Project Summary and Background

1.A. Problem and Objectives: Explaining Kinematic Transitions at Intermediate Reynolds numbers ($Re = 1-100$)

Organisms ranging in size from bacteria to whales interact with fluid media in order to locomote, filter-feed, or enhance diffusion of waste, nutrients or metabolic gases. Flows can be internal, such as cilia lining respiratory passages, or external, generated by oscillating appendages such as legs and wings. The use of particular kinematic patterns or morphologies can be generally predicted by certain physical scaling principles. Predominant among these is the scaling of the importance of the inertia of the fluid relative to the viscosity. Small appendages operate in mainly viscous flows while large, fast appendages experience mainly inertial forces (Videler, 1993). The ratio of inertial to viscous forces is expressed by the Reynolds number Re , derived from the appendage or body speed U , body or appendage length L , and kinematic viscosity of the fluid: $Re=UL/\eta$. Organisms operating in an intermediate range (Re 1-100) are impacted strongly by both inertia and viscosity. Oscillating appendage systems that perform diverse fluid dynamic functions do so at a wide range of Re numbers due to the tremendous size range of aquatic and aerial organisms, and due to the necessity of both cellular and multi-cellular scale fluid motion within a single organism.

The evolutionary adaptation of appendage kinematics at both the species and ontogenetic scale may in most cases strongly reflect the physical scaling of these two force categories. It is not known to what extent appendage systems may utilize kinematics that can be used successfully at different Re , or what modifications or required to execute this transition.

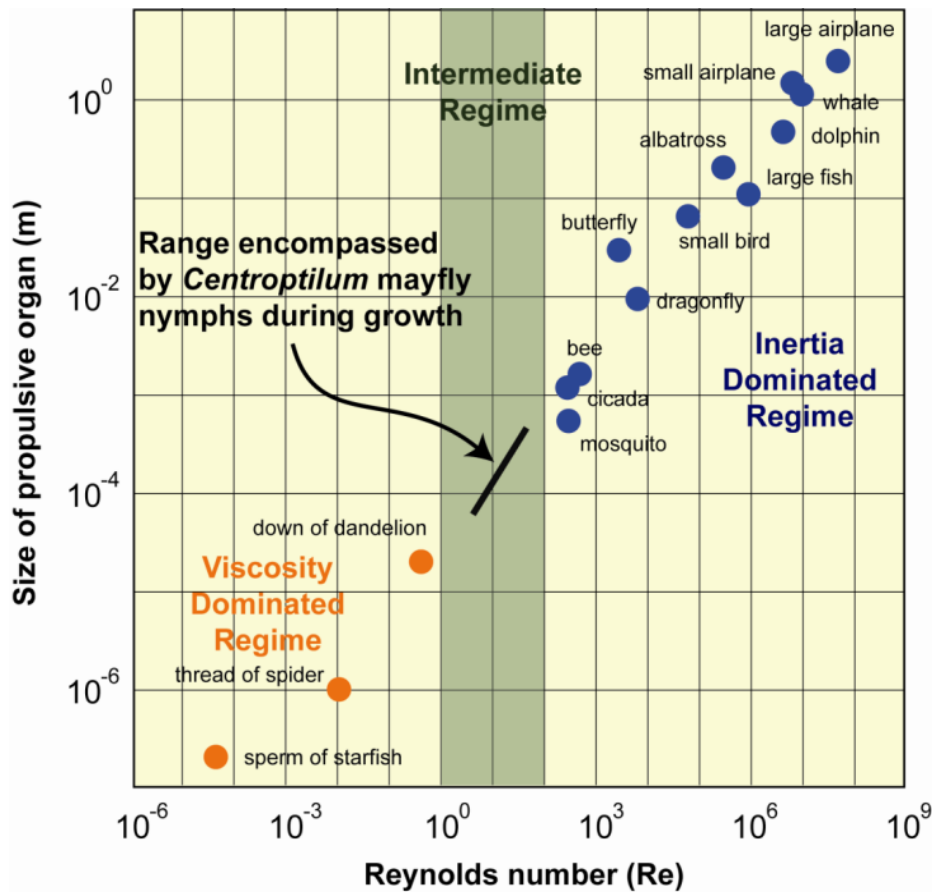


Figure 1. The length of locomotory appendages plotted against their respective Reynolds numbers to show the wide range of biologically relevant Re numbers, in addition to several examples of human made machines. Mayfly nymphs operate within what is typically denoted as the intermediate Re regime.

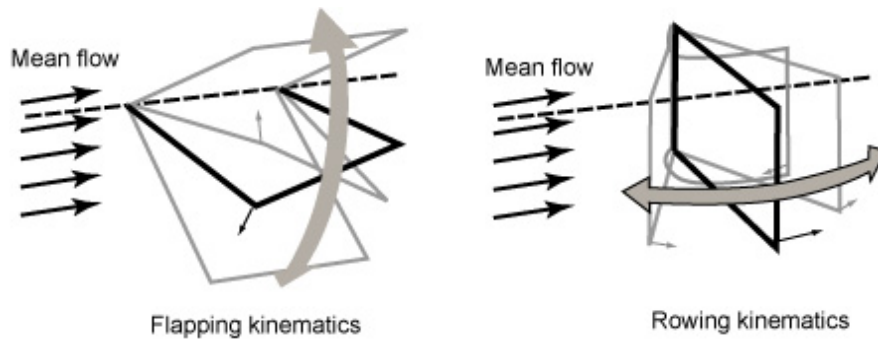


Figure 2. Schematic illustration of the kinematic distinction between flapping and rowing type motions (after Walker and Westneat, 2000).

A specific example of the dichotomy presented by changing importance of various forces is the rowing/flapping category of biological or machine motions. Pure flapping is defined as appendage stroking perpendicular to flow or to the direction of motion (Figure 2). Flapping works by generating forces that are normal to the flow over the appendage through the mechanism of circulatory lift (Dickinson, 1996). By pitching the appendage leading edge down on the down stroke (negative pitch) and leading edge up on the up stroke (positive pitch), a flapping appendage can generate thrust throughout the stroke cycle. In rowing, a net thrust is generated by separating strokes into a power half-stroke that produces high thrust through drag, and a recovery half-stroke that reduces drag via changes in appendage shape, orientation or speed (van Duren and Videler, 2003; Kohlhage and Yager, 1994). Flapping motions are more prevalent in organisms operating at high Re (Walker, 2002; Walker and Westneat, 2002).

Here I provide a detailed PIV-based description of one such multi-appendage system, the gill array of nymphs of the mayfly *Centroptilum trangulifer* (Baetidae). My goal is to associate major changes in gill kinematics and gross flow structure with

fine-scale hydrodynamic phenomena to generate more precise biomechanical explanations of general patterns, which can then be tested in *Centroptilum* and other systems. While comparative studies across animals are invaluable for identifying general trends, they do not address precisely how inertial and viscous effects are manifested in flow structure or how such effects interact among and between themselves within an array of appendages. This is, in part, due to the fact that most of the studied animals do not commonly transit this intermediate regime, but rather spend their life on one side or the other of the boundary. Those examples that do cross the intermediate regime typically use a separate appendage set on either side of the boundary [(e.g. ciliary to wing propulsion in arctic pteropod (Childress and Dudley, 2004) and antennal to leg propulsion in some crustaceans (Williams, 1994b)].

In theory, the broad association between kinematics and Re could be produced in many system-specific ways. Consequently, visualizing and describing flow at fine scales of resolution, such as the level of individual appendages, is an essential step toward greater understanding of how general patterns, such as the rowing-flapping dichotomy, are produced. With such data, basic hypotheses concerning Re -driven behavioral shifts and appendage interactions can be tested to allow for improved understanding of functional performance and model development.

1.B. Model system and Measurement Techniques

1.B.1. Previous work on gill arrays in nymphal mayflies

For this study, I examined the nymphal stages of the relatively primitive order of insects, the mayflies (Order Ephemeroptera). Certain mayfly species can live in

relatively warm, stagnant water, environmental conditions that drive oxygen concentration very low. Unlike air, with relatively fixed ratios of gases, the ability of water to hold dissolved gases is strongly dependent on temperature. Additionally, the much smaller diffusivity of oxygen within a liquid (in comparison to a gas) can lead to regions locally depleted of oxygen that can only be readily replenished by convective mixing. Those species of mayfly nymphs living in such low-oxygen conditions are typically equipped with an array of external appendages that both increase the surface area for gas exchange and actively mix the water adjacent to the animal. The morphology and kinematics of these fluid mixing/pump plate arrays varies dramatically with species. Those species equipped with solid plates can vary in the degree of plate flexibility and shape of the individual plates, and the distribution of respiratory tracheae. The mechanisms by which the water is pumped have been speculatively described variously as rowing or suction generated by specifically timed opening and closing phases of neighboring plates (Eastham, 1932; Eastham, 1936; Eastham, 1937; Eastham, 1958; Eastham, 1939), based purely on visual observation of the gill motion and qualitative flow visualization. The individual flow phases have been difficult to resolve prior to the advent of high-speed imaging and automated particle tracking.

Most aquatic organisms larger than 1 mm have structures which increase surface area and are highly permeable to dissolved oxygen. Branchiopod crustaceans, Xiphosura and Ephemeroptera (Williams 1994) are prominent examples of such organisms that actively oscillate these structures. Previous studies of mayfly nymph gill arrays have examined plate structure and kinematics as a function of species diversity in mayfly nymphs (Eastham 1934, 1936, 1937, 1939, 1958, (Eriksen and

Moeur, 1990)). The gill plates of mayfly nymphs are used in the generation of ventilation current in some species but are passive in others (Baumer et al., 2000). In some, if not all species, gill plates are retracted against the abdomen to reduce drag during escape swimming, with propulsive power generated by whole body dorsal-ventral undulation (Brackenbury, 2004; Kutash and Craig, 1998)(original observation for *C. triangulifer*). Thus, mobile gill plates are potentially a low-power system relative to the demands of locomotion. Because of their large surface area, the appendages perform an important diffusion role that can function independently of active motion. In such a system, appendages can develop ontogenetically and over evolutionary time, performing vital roles whether or not they are actuated. Within mayfly abdominal tracheal gills, both respiratory strategy and external morphology (size, shape) have likely undergone many changes as species radiated into more or less oxygenated water (Baumer et al., 2000; Gillies, 1997), as illustrated by differences in closely related taxa. Therefore, we might expect that gills are primarily adapted to function in a non-actuated (passive) role, and secondarily designed for actuated fluid dynamics. In many organisms, ventilation is a low-power continuous process where mechanical efficiency may be at more of a premium (Riisgård and Goldson, 1997) than in the high-speed but intermittent escape reactions common in zoo-plankton (van Duren and Videler, 2003).

1.B.2. *Centroptilum triangulifer*

For this study, I examined the nymphal stages of one species of mayfly, *Centroptilum triangulifer*, a parthenogenetic species common in slow-flowing streams in eastern North America(Figure 3). It is multi-voltine, and nymphs can be found year-round (Sweeney et al., 1992; Funk et al., 2006). This species has an

intermediate tolerance to high temperatures, stagnant water, and industrial pollution. Eggs of *Centroptilum* were obtained from a stock population of Stroud Water Research Center (Avondale, Pennsylvania, USA), and nymphs were reared at 20° C in 1 cm of water within covered petri dishes. The water was a mixture of distilled and stream water (White Clay Creek, Avondale, Pennsylvania, USA), and the stream water contained the nymph's primary food of diatoms and other microbial debris. The shallow water precluded the need for an aerator, and a few hours of sunlight was sufficient to maintain the diatoms. After several instars (15 days), nymphs were about 1 mm long and single lamellar gills developed on the lateral edges of seven adjacent abdominal segments. Following the standard numbering scheme (Eastham, 1936; Eastham, 1937), gill pairs of each segment (1-7) are designated by order from anterior to posterior position. At about 20 days, nymphs were about 2 mm long with actively oscillating gills.



Figure 3. Intermediate ontogenetic stage nymph of *Centroptilum triangulifer*. Photograph courtesy David Funk.

1.B.3. 3-D stroke kinematic measurement

In order to capture high-speed images of the ventilation behavior, nymphs were captured from their petri dish, restrained using a small pin and then *Re-*immersed in a special glass viewing chamber. Nymphs initiated periods of ventilation as the oxygen diminished in the chamber. Lateral and dorsal images (4 x 4 mm field of view) of the ventilating array were captured by two synchronized cameras (Phantom v9, 1632 x 1200 pixels; V.4, 512 x 512 pixels) operated at 1000 fps and attached to Leica dissecting microscopes (30 x magnification zoom lens). The cameras captured a dorsal and lateral perspective of the animal. Along with the root location (R), the tip (T), medial edge (ME), and lateral edge (LE) of each gill were digitized in each frame (see landmarks defined in Figure 4) in order to track the motion of these points through time.

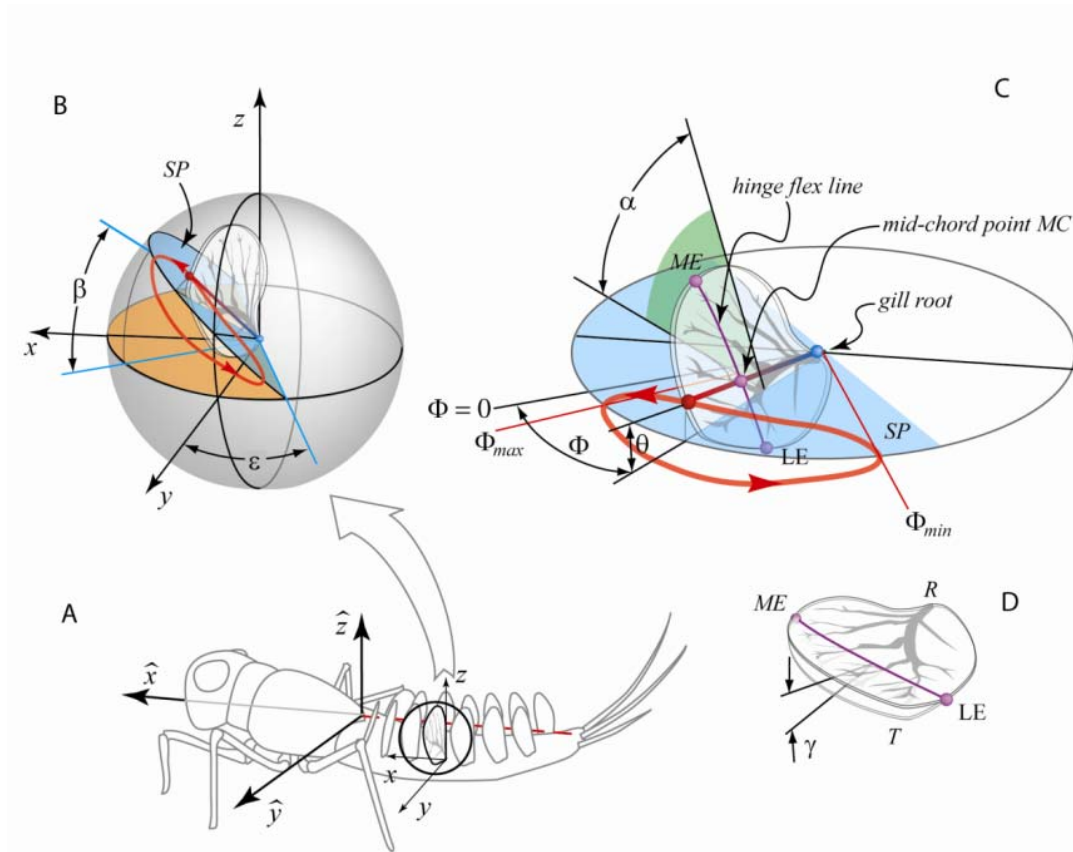


Figure 4. Spatial axes and angles used in characterizing gill-plate kinematics in the nymphal mayfly. A. Diagrammatic mayfly nymph from an oblique lateral perspective showing spatial coordinates relative to the body (\hat{x} , anterior-posterior axis; \hat{y} , transverse axis; \hat{z} , dorsal-ventral axis) and parallel coordinates originating at the gill root (x, y, z). B-C. Key kinematic parameters. The stroke plane (SP) for each cycle - indicated in blue - is defined by three points: the gill root and the anterior and posterior extrema of the gill mid-hinge point. The orientation of the SP is defined by the stroke plane inclination angle (β), measured between the SP and the horizontal (x - y) plane within a mutually orthogonal plane, and the stroke plane lateral offset angle (ϵ), which indicates where the SP crosses the horizontal (x - y) plane. The instantaneous position of the mid-chord point (path indicated by the red curve) is then given by the combination of the stroke angle, Φ , and stroke plane deviation, θ , which measures the angular displacement along and normal to the SP, respectively. The stroke angle origin ($\Phi = 0$) is reference to the position where the SP intersects the transverse-vertical (y - z) plane, and the respective posterior/anterior excursion limits are given by $\Phi_{\min} / \Phi_{\max}$. The orientation of the gill plate is referred to as the pitch, α , which is defined as the angle between the gill plate and the SP, as measured in a mutually orthogonal plane. D. Gills in larger nymphs have a distinct transverse hinge flex line. The hinge angle, γ , is defined as the deflection of the distal gill plate (flap) from the nominally planar configuration. The hinge angle is positive when the hinge is flexed posteriorly and negative when flexed anteriorly.

1.B.4. Flow measurement through Particle Image Velocimetry

Hollow glass beads (11 μm mean diameter) were added to the same viewing chamber used for the appendage kinematic imaging. Too few beads would not give

enough points for the computer to track, while too many beads would also restrict imaging by increasing the opacity of the fluid through which light travels from the specimen to the camera. Glass beads were gradually added to the water until several dozen beads were in focus within each intergill space. Beads were only slightly higher density than water, descending to the chamber floor after several minutes. The velocity of this descent was so small as to be insignificant compared to the ventilation velocities of interest. We generated a light sheet from the beam of a continuous Argon ion laser, and used this light sheet to quantify flow in a dorsal plane cutting through the gills just above the center of the abdomen and in a lateral plane cutting through the gills just lateral to the gill roots. High resolution was possible through ensemble-correlation PIV (Meinhart et al., 2000), since the observed flow is ostensibly laminar and highly repeatable from cycle to cycle. Ensemble correlation works by artificially “increasing” the density of beads in the imaged region by using multiple equivalent phases of a motion to reconstruct the flow field. Thus, it is only appropriate for low and intermediate Re flows, where turbulence does not introduce stochastic effects between stroke cycles.

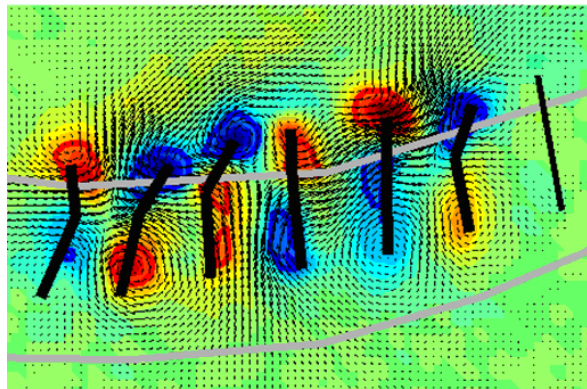


Figure 5. Example of the flow field reconstruction possible through ensemble correlation. Vectors (arrows in black) were calculated at every 16 pixels, for 102x75 vectors in full field. Shown is one frame within a sequence of 34 frames required to complete one array oscillation cycle. Vortices were identified automatically in each frame, with blue outline indicating negative (clockwise) vortices and red indicating positive (counter-clockwise) vortices.

1.C. Objective and Scope of this Study

Studies of flapping wings in diverse aerial taxa; fruit flies (Birch and Dickinson, 2003), hawkmoths (Usherwood and Ellington, 2002), butterflies (Brodsky, 1991), birds (Spedding et al., 2003) and some aquatic taxa (Borrell et al., 2005) are almost entirely concerned with flow around a single wing or single pair of wings and have generally been conducted in systems operating at $Re > 10$. The question remains as to how organisms that grow from $Re \sim 1$ to $Re \sim 10$ cope with the necessity of non-reciprocal motion at one end of the scale, the ability to use both skin friction and form drag, and the potentially high efficiency of certain types of reciprocal motion at higher Re .

While comparative studies across animals are invaluable for identifying general trends, they do not address precisely how inertial and viscous effects are manifested in flow structure or how such effects interact among and between themselves within an array of appendages. This is, in part, due to the fact that most of the studied animals do not commonly transit this intermediate regime, but rather spend their life on one side or the other of the boundary. Those examples that do cross the intermediate regime typically use a separate appendage set on either side of the boundary [(e.g. ciliary to wing propulsion in arctic pteropod (Childress and Dudley, 2004) and antennal to leg propulsion in some crustaceans (Williams, 1994b)].

In theory, the broad association between kinematics and Re could be produced in many system-specific ways. Consequently, visualizing and describing flow at fine scales of resolution, such as the level of individual appendages, is an essential step toward greater understanding of how general patterns, such as the rowing-flapping dichotomy, are produced. It would therefore be instructive to study a single species

that transits the intermediate Re regime using a single set of appendages and undergoes a shift from rowing to flapping. Understanding the details of how Re regime limits kinematics is complicated by several factors. In particular, even for idealized or model systems, intermediate Re propulsion mechanisms are a challenge to study, as the simplifying assumption of high Re (viscosity free) or low Re (inertia free) flow does not apply. In addition, many of the basic kinematic patterns of organisms have been described in systems based on a single airfoil blade or paired wing interaction. Multiple appendages organized into an array introduce some new possibilities for mechanisms and pumping effectiveness. Those aquatic arrays that have been studied have generally lacked sufficient resolution of the fluid motion within the array to test hypotheses about kinematic shifts.

1.D. Conclusions from this Thesis

Throughout the final ontogenetic stages, from 2-6 mm body lengths, nymphs oscillated gill plates and generated vortex structures approximately 1/5 of a cycle out of phase with adjacent plates. This is the first intensive analysis of directed pumping by such a metachronal biological array. I propose calling this pumping phenomenon a “phased vortex pump”. Despite the use of a basic plate array plan over ontogeny, our high speed imaging revealed that ventilation was maintained with multiple changes in the mechanics of the array, including plate kinematics, plate morphology, phasic coordination of gill plates, and the fluid kinematics. A majority of these changes occurred at a nymph size of about 3 mm body length. The main conclusions from this study are as follows:

1. Plate kinematic changes

On the level of the individual plates, change occurred through reductions in the range of pitch motion, the ratio of peak protraction/retraction speeds and stroke plane deviation over a narrow range of $Re \sim 4-9$. The combined effect of these plate-level changes was to increase temporal symmetry of gill stroke with increasing Re . Together, the individual plate kinematics (pitch and stroke plane deviation) and array phasing resulted in a powerstroke phase in the small nymphs. Notably, the pitch change, stroke plane deviation, and array phasing are all time-irreversible components of the motion that enable function in viscous flow, as is the asymmetric stroke velocity of individual plates in the context of the phasic array.

2. Morphological changes

Plates developed from relatively low aspect ratio, stiff wing-like structures into broad plates with flexibility about a clearly defined distal hinge. The plate kinematic and morphological adaptations over ontogeny are the focus of Chapter 2.

3. Fluid kinematic changes

Vortices advected dorsally and shed in the large nymphs, but traveled ventrally in the smallest nymphs, dissipating entirely before shedding could be identified. Vortex structures enveloped several gills simultaneously only for the recovery half-stroke in large nymphs, but for both the recovery and some of the powerstroke in the small nymphs. These fluid kinematic differences over ontogeny are the focus of Chapter 3.

4. The combination of Reynolds number change and nymph adaptations produce a change from posterior/ventral flow to dorsal/transverse flow at higher Re_f , essentially a transition from a rowing stroke to a flapping stroke. While the measured

vorticity may be generated by similar unsteady processes in small and large nymphs, the timing and scale of the structures changed due to the increased effects of diffusion relative to appendage size. The rowing-to-flapping kinematic transition in *Centroptilum* occurred at $Re \sim 5$, when the maximum dynamic intergill distance equalled vortex diameter (Figure 6). While the intermediate Re range 1-100 has been identified as having fundamental effects on biological appendages, I identify more specifically the range of $Re \sim 3-8$ as the crucial range for the onset of effective transverse pumping, and furthermore the specific mechanism behind this transition. Significant flow between appendages may only occur when the viscous effects are not so great as to extend across the appendage gap in the form of independent vortices. This fluid kinematic feature may be a useful predictor of shifts in functional performance for all those organisms equipped with oscillating arrays of legs, paddles, or other plate-like structures.

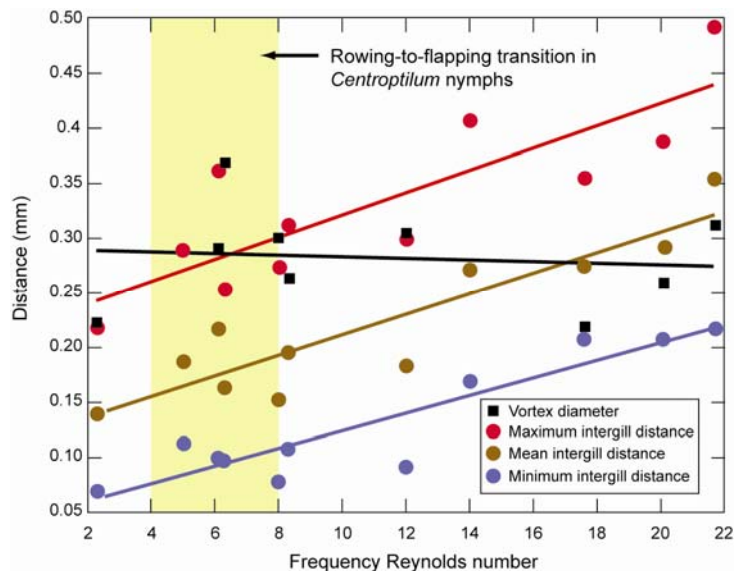


Figure 6. Plot showing the relationship between vortex size (dark squares) and measures of intergill spacing. The hypothesis generated here maintains that the organized intergill flow required for effective flapping can only occur when the diameter of self-generated vortices is smaller than the intergill spacing. Significantly, the vortices do not change absolute size during mayfly growth and intergill spacing exceeds vortex size at $Re \sim 6$. This value corresponds to the Re at which mayfly nymphs transition from rowing to flapping.

1.E. Background: Hydrodynamics of oscillating appendages

1.E.1. Influence of Reynolds number on flow behavior

One of the challenges in developing a comprehensive theory of biological fluid dynamics is to understand how fluid dynamic mechanisms change with body size. The primary method of studying the effect of body size on fluid mechanics has been to examine species that differ in size. The diversity of flying insects are characterized by Re regimes ranging from 10 to 10 000, while arthropods and larval vertebrates in water can range far lower than this, down to Re 0.01. Microorganisms have been studied which move at $Re \ll 1$, such as bacterial locomotion with flagella. In such organisms, the role of inertia is virtually nil, and locomotion is accomplished entirely by mechanics based on the differential drag on different orientations of an appendage.

Two main forces are at play on a body moving in fluid (Shapiro, 1961). Skin friction is generated by the resistance of a fluid to shearing and is proportional to speed of the flow. Form force is generated by the differences in pressure on the surface of the body, varying with the square of the velocity. At low Reynolds number ($Re \sim 1$), skin friction accounts for nearly all of the force between an appendage and fluid. Both skin friction and form force are important in the production of drag and thrust at intermediate Reynolds number ($Re \sim 10$). At high Reynolds number ($Re \sim 100$), form force is the only significant contributor to thrust, but skin friction remains as an important component of the drag on the moving body (McHenry et al., 2003).

1.E.2. Basic division of kinematics: Rowing vs. flapping

Appendages generate force in fluids through net action of the viscous stress and pressure distribution across its surface. At high Re , the net viscous contribution

is typically small in comparison to that of the pressure, which is effectively generated by the change in inertia of the fluid surrounding the appendage. Under these conditions, the inviscid concept of circulatory lift force is the dominant effect, so that an appendage translating at a small angle of attack relative to oncoming flow experiences a high force perpendicular to this flow (lift). Due to the unsteady motion, a component of the instantaneous lift is directed along the flow such that there is a net production of positive thrust. This corresponds to a simplified view of the case for a flapping type motion, and here we take pure flapping to occur when appendage strokes are perpendicular to flow or to the direction of motion (Figure 2). In contrast, at very low Re , viscous stresses become dominant, and inviscid mechanisms such as circulatory lift become ineffective. Under these conditions, a net thrust is generated by separating strokes into a power half-stroke that produces high thrust through drag, and a recovery half-stroke that reduces drag via changes in appendage shape, orientation or speed (van Duren and Videler, 2003; Kohlhage and Yager, 1994). A rowing type motion then corresponds to an appendage stroke that is along the direction of the flow or net thrust. It should be noted that rowing strokes and mechanisms are also possible at higher Re (the oar of a rowboat being a classic example), but under these cases it is the inertia reaction of the fluid, and not viscous forces which are responsible for the thrust. Typically, it has been observed that flapping motions are more prevalent for high Re conditions, as speculated for a net gain in efficiency (Walker, 2002; Walker and Westneat, 2002).

Comparative studies encompassing a wide range of aquatic animals have shown that rowing is exclusively used at low Reynolds numbers ($Re < 1$) while flapping is predominantly used at $Re > 100$, but few studies have been undertaken to

document the transition in individual species that traverse the intermediate Re regime using a single set of appendages. Thus, it is not generally known whether a gradual increase in Re within a system results in a gradual or sudden shift between rowing and flapping.

1.E.3. Vorticity: definition and why it is a useful description

Vorticity is the local angular rate of rotation in a fluid. The vorticity ω at a point in fluid is the limit as the area approaches zero:

$$\omega = d\Gamma/dA$$

where Γ is the circulation of that fluid region, and A is the area of that region.

All fluid forces acting on a submerged body result from physical interactions succinctly expressed in the Navier–Stokes equation. A version of this equation derived by (Wu, 1981) captures all aerodynamic force (F) acting on a solid body within a fluid:

$$F = -\rho \frac{d\gamma}{dt} + m' \frac{dU}{dt},$$

where ρ is fluid density, t is time, m' is the mass of the fluid displaced by the solid body, and U is the velocity of the body. The γ in the first term represents the first moment of vorticity (ω), defined as:

$$\gamma = \int_{R_\infty} \mathbf{r} \times \omega dR,$$

where r is the position vector, ω is the vorticity and dR is the element of area. The first term of the force equation encompasses all components of the current quasi-steady model of flapping flight (translation, rotation, wake capture and the volume-independent component of acceleration reaction) (Birch and Dickinson, 2003). The second term in the equation is the component of the total force generated by the volume of an accelerating body as it displaces fluid. This component is known as the added mass force. The contribution of the second term (added mass force) is negligible for objects with minimal volume, such as thin plates. Thus forces on thin plates result predominantly from time-dependent changes in the magnitude and the distribution of vorticity (the first term). For example, in the case of a wing moving with constant bound vorticity, the vector r is the only time-dependent variable, which increases as the wing moves away from the shed starting vortex. Under these conditions, equation 1 reduces to the Kutta–Joukowski equation (Wu, 1981), which states that the force is proportional to the bound circulation multiplied by the wing velocity. Under more complicated conditions, such as during an impulsive start or stroke reversals of a flapping wing, the growth and decay of vorticity at fixed locations within the flow field will also contribute to force production, as will the shedding of vortices. This equation can be useful in an experimental context in which only the velocity field is known. The Navier–Stokes equation, in contrast, requires quantification of the pressure field.

Those models of biological fluid mechanics that have proved useful, such as clap fling and steady state lift, encompass most of the dynamic relations in a mathematically tractable way. These models typically require specific conditions for this to occur. However, the total force on an unsteady moving appendage can be

calculated directly with a complete unsteady history of the vorticity field, independent of the specific categorization of the force components that would be identified in component models. However, accurate calculation of force from the vorticity field requires tracking vorticity not only in 3 dimensions but in all of space and thus may be cumbersome to measure and/or calculate.

Flow evolution at low Re is dominated by viscous diffusion. In contrast, vorticity diffusion is less significant relative to the length scale of other flow structures at high Re , and instead vorticity is distributed predominantly through advection. Regardless of the source of vorticity, at a set frequency of oscillation, the distance that vorticity can diffuse in one oscillation is given by the viscous diffusion length: $L_{vd}=(2\nu/\omega)^{0.5}$ where ν is kinematic viscosity and ω is frequency (Morton, 1984). The vorticity diffusion length is comparable to appendage size in many intermediate Re organisms (Taylor, 1951). Ontogenetic growth of appendages through a viscous diffusive length comparable to appendage length may mandate a shift in the mechanisms and/or kinematics utilized by an organism, and this is another reason that viscous diffusion length (vortex size and tracking) is a relevant perspective from which to examine biological fluid pump diversity.

1.F. Review of stroke mechanics and mechanisms

1.F.1. Drag-based mechanisms

The Reynolds number determines many general features of a flow pattern, including the roles of viscous stress and pressure on a moving structure. As a result, there exist some general rules that relate kinematics to Re , both in theory and in surveys of the range of behaviors and structures seen in nature.

A general principle regarding flow in the classical creeping flow regime, $Re \ll 1$, where viscosity and thus skin friction dominate, is that time-reversible motion is not effective at generating net propulsion. The simplest description of time reversible motion is a kinematic pattern which looks the same when a movie is played forward or backward. This principle is known as the “Scallop theorem” (Purcell, 1977), after the swimming motion performed by this organism. Scallops swim by opening and then rapidly closing the shell, expelling a jet of fluid out of the shell and propelling the animal in the direction of the shell hinge. Swimming with these kinematics can only occur at high Re , where the momentum generated by the rapid closing of the shell is greater than that generated by the slower opening. More specifically, the “Scallop theorem” states that no time reversible sequence of boundary configurations can swim at low Re . To achieve propulsion at low Reynolds number, a swimmer must deform in a way that is not invariant under time-reversal symmetry. The undulatory motion of flagella by many bacteria species (Wiggins and Goldstein, 1998; Tony et al., 2006) and the undulation by the tails of tadpoles and fish at intermediate Re (Tytell, 2004) can accomplish locomotion by assigning time/space direction to the motion in the form of a traveling wave against the direction of propulsion.

Although all oscillating appendages use drag to generate force at low Re , the term rowing is typically reserved for those appendages that separate appendage stroke cycles into a powerstroke and recovery stroke. Using a power and recovery stroke distinguished solely by speed changes will only be effective at sufficiently high Re , and few, if any organisms utilize only this kinematic differentiation of the stroke half cycles. On the other hand, creating asymmetry by reducing paddle surface area and

limb span during the recovery stroke produces a non-time reversible kinematic pattern, a rowing stroke that can be utilized at all Re by generating both skin friction and form drag (Nachtigall, 1974; Zaret and Kerfoot, 1980; Hessler, 1985; Fryer, 1991; Kohlhage and Yager, 1994; Vogel, 1994).

Two active particles undergoing reciprocal deformations can swim collectively (Lauga and Bartolo, 2008). There is, therefore, no “many-scallop” theorem. Thus the limitations imposed by the scallop theorem can be overcome by placing a reciprocal motion near another such motion that is slightly out of phase, such as in an array of appendages.

1.F.2. Lift-based mechanisms:

Quasi-steady flow

Flapping works by generating forces that are normal to the flow over the appendage through the mechanism of circulatory lift (Dickinson, 1996). By pitching the appendage leading edge down on the down stroke (negative pitch) and leading edge up on the up stroke (positive pitch), a flapping appendage can generate thrust throughout the stroke cycle. Thus, even aquatic animals can be described as flying if the kinematics incorporate a flapping stroke.

The computed force due to classical steady-state lift on an aerofoil was famously insufficient to account for the actual force generated by insects that were clearly using flapping kinematics. This discrepancy has been explained by the importance of time dependent (unsteady) effects (Dickinson and Gotz, 1993). Unsteady effects produce or diminish lift and drag forces when an appendage oscillates over relatively short distances, so that the effect of previously generated

vorticity remains important. Ultimately, unsteady effects are based on the concept that the growth rate of circulation, rather than total circulation, describes the force generated during wing oscillation. The turn around or halfstroke switch point phases of an insect wing have thus been intensively studied in order to properly account for the average force over the full stroke cycle (Sane and Dickinson, 2002). The well studied field of ‘classical’ airfoil theory (Kutta–Joukowski theorem, etc.) must be complimented by the more empirical approach of quasi-steady models of forces on translating appendages. In one such quasi-steady model, the “blade element” model (Sane and Dickinson, 2002), the total lift force generated by a wing is the sum of the contribution of discrete segments (‘blade elements’). The lift and drag force generated by each of these elements is calculated with relationships that are rooted in classical translating airfoil theory, but which are corrected using empirical constants for unsteady and three-dimensional effects.

Leading Edge Vortex

Unlike the smooth flow and bound circulation around the classical model, insect wings appeared to operate with most of the circulation concentrated in a bubble of vorticity just above and behind the leading edge. This leading edge vortex (LEV) was confirmed as crucial to lift (Ellington *et al.*, 1996), and resembled that seen in the classical high Re wing at near stall. In 2D simulations, leading edge vortex on insect wing models grows to an unstable size and shed into the wake quite early in the stroke (Dickinson and Gotz, 1993), resulting in large loss in lift as in the classical stall phenomena. Several subsequent 3D simulations have shown that at the Re relevant to insect flight, the LEV remains attached until stroke reversal, maintaining high lift on the wing throughout the stroke (Poelma *et al.*, 2006; Lehmann *et al.*, 2005). The

delayed separation of the LEV has thus been attributed to 3D effects such as the strong spanwise flow through the LEV (Ellington *et al.*, 1996), and most recently by the constant draining of circulation by two counterrotating vortices shedding near the wing tip (Poelma et al 2006).

Clap-fling

The basic LEV concept involves only a single wing. Other unsteady interactions based on paired wing interactions also supplement the force calculated from steady-state mechanisms. These phenomena include wake recapture and clap-fling (Dickinson, 1996). The clap-fling mechanism was inspired by a study of a small flying wasp (Weis-Fogh 1973). The smallest insects, including members of the fairy flies (Hymenoptera: mymaridae) and feather-winged beetles (Coleoptera: Ptiliidae), have been suggested to row through air with a downward power stroke and upward recovery stroke (Bennett, 1966; Thompson, 1917; Horridge, 1956), since circulatory forces calculated from classical theory were so low. However, Weis-Fogh (1973) reported that the wasp *Encarsia formosa* (wing length approximately 0.6–0.7 mm, $Re=17$), 3 times larger than the smallest flying insects, flies with a largely dorsoventrally oriented, flapping stroke during both fast forward flight and hovering. This kinematic observation ruled out rowing as a primary mechanism in this species, and inspired the novel mechanism of clap-fling. The approach (clap) and then rapid separation (fling) of contralateral wings was predicted to produce high lift force, based on the concept that during fling, the conservation of zero circulation is met by the equal and opposite circulation of the LEV of each wing, so that no vortex need be generated at the trailing edge as must occur in isolated aerofoils starting motion from rest (Lighthill, 1973; Weis-Fogh, 1973; Spedding and Maxworthy, 1986; Miller and

Peskin, 2005). Since then, the lift enhancing effect of clap fling has been verified in physical models and simulation (Miller and Peskin, 2005; Lehmann et al., 2005). Lift enhancement during clap-and-fling required an angular separation between the two wings as low as 10–12° and increased total lift production by up to 17% (Lehmann et al., 2005). While the clap fling mechanism has historically referred to paired aerial wings in close proximity, its basic mechanics could apply to many other morphologies with closely spaced appendages. However, there are many variations of this basic mechanism in flying organisms; a particularly important variation is the clap-peel by flexible wings (Cooter and Baker, 1977; Brackenbury, 1990). The fling phase is equivalent to a suction generating phase as plates separate. Studies suggest that most of the lift enhancement occurs due to the fling phase, rather than the clap.

Squeeze

A little studied component of the clap-fling mechanism is the squeeze force that occurs at the end of the clap phase. In this clap phase, the approaching wings form a wedge that creates a downward jet of fluid consistent with the desired upward propulsive force direction (Gotz, 1987). These appendages would generate force as they approach an adjacent appendage or body wall and force fluid out of the narrowing space. Jet propulsion, such as by squid, consists of ejecting fluid from a body cavity at high speed and is thus an idealized version of a 2-sided volume represented by external oscillating appendages.

Squeezing forces are particularly relevant to those appendage systems with a plate-like morphology and with individual plates operating in close proximity (i.e. an array). Other oscillating appendage systems besides clap-fling wing systems that could produce squeeze force occur in pectoral fins (Westneat and Walker, 1997) or

legs slapping against the body (Nachtigall, 1974), gill plates (Eastham, 1932; Eastham, 1936; Eastham, 1937), parapodia of sea-hares (Bell, 1984), fused ciliar plates of comb jellies (Barlow et al., 1993), and curling of tail and abdomen during decapod crustacean escapes (Daniel and Meyhofer, 1989). Most studies of fish pectoral fins and crayfish tail curling have ignored the effects of the narrowing space between the appendage and the body wall, and assumed that drag or circulatory lift associated solely with appendage motion relative to the fluid dominate the force balance. In any case, it is clear that for oscillations with large stroke range, the squeeze force should be most significant only in the phases of a stroke in which the appendage approaches the body wall or neighboring appendage. The analytical solution for a large plate closing against a flat surface at high Re (Brennen, 1982) was used to predict significant thrust generation as a shrimp tail and abdomen closed together. However, the high squeeze force predicted was not verified by force measurements in a similar animal *Panulirus interruptus* (Nauen and Shadwick, 2001). Corroborating this, there was no evidence of a significant squeeze force by the flapping appendage of a bird wrasse (Walker and Westneat, 1997) or the rowing appendage of a threespine stickleback (Walker, 1999). Thus, the squeeze force may play a minimal role at these high Re ($>1,000$) behaviors. While the jet from the clap phase has not been studied in detail, the overall clap-fling mechanism was shown to increase in importance as Re was lowered (Miller and Peskin 2005). The possibility remains that the jet produced by rapid approach of appendages may be quite significant especially for systems that use a low stroke range at low Re . The rapid dissipation of circulation implied by lower Re operation diminishes the role of any steady-state translational circulation so that paired appendages may capitalize on the

opening or closing squeeze force rather than the translational circulation based component that dominates the classical clap fling model.

Chapter 2: Gill-plate stroke kinematics

2.A Introduction

Animals use diverse mechanisms to generate currents for ventilation, feeding and locomotion, but comparative studies have revealed trends associated with animal size that transcend differences in morphology and phylogeny (Strathmann, 1993; Walker, 2002). The Reynolds number ($Re = \rho UL/\mu$) is a key dimensionless parameter in fluid dynamics that reflects the relative importance of the fluid's inertia in comparison to viscous effects (i.e., internal friction of the fluid). For the same working fluid, the form of the Reynolds number indicates that the inertia dominates at large sizes and high velocities ($Re \gg 1$), while viscous forces control the flow dynamics for small sizes or relatively low speed ($Re \ll 1$). Indeed, the basic mechanisms operating at the biological extremes of Re are relatively well understood, as exemplified by studies based on inviscid models for relatively fast and/or large swimming or flying vertebrates ($Re > 1000$) (Spedding et al., 2003; Daniel, 1992; Motani, 2002) and the classical studies of viscous flow around flagella and cilia ($Re \ll 1$) (Taylor, 1951; Gray and Hancock, 1955; Lighthill, 1976; Brennen and Winet, 1977). Definitions of intermediate Re vary among workers (Daniel TL, 1987; Daniel, 1992; Fuiman and Batty, 1997; Walker, 2002; Webb and Weihs, 1986), but all generally encompass $Re = 1$ to 20. This intermediate regime spans a very narrow but important part of the biologically relevant Re spectrum. Comparative studies and computer simulations (Walker, 2002; Childress and Dudley, 2004) indicate that organisms at the lower end of the regime should exclusively use rowing strokes and those at the upper end should tend to use flapping strokes, due to benefits in propulsive efficiency or viscous limitations on thrust production by simple flapping

motions. Consequently, studies of organisms that transit this region as individuals, either ontogenetically or behaviorally, may be important in establishing how aquatic animals achieve the rowing-to-flapping transition and whether this transition is sudden or gradual.

In order to facilitate further discussion, it is first appropriate to provide a definition of what constitutes rowing or flapping kinematics. Appendages generate force in fluids through net action of the viscous stress and pressure distribution across its surface. At high Re , the net viscous contribution is typically small in comparison to that of the pressure, which is effectively generated by the change in inertia of the fluid surrounding the appendage. Under these conditions, the inviscid concept of circulatory lift force is the dominant effect, so that an appendage translating at a small angle of attack relative to oncoming flow experiences a high force perpendicular to this flow (lift). Due to the unsteady motion, a component of the instantaneous lift is directed along the flow such that there is a net production of positive thrust. This corresponds to a simplified view of the case for a flapping type motion, and here we take pure flapping to occur when appendage strokes are perpendicular to flow or to the direction of motion (Figure 2). In contrast, at very low Re , viscous stresses become dominant, and inviscid mechanisms such as circulatory lift become ineffective. Under these conditions, a net thrust is generated by separating strokes into a power half-stroke that produces high thrust through drag, and a recovery half-stroke that reduces drag via changes in appendage shape, orientation or speed (van Duren and Videler, 2003; Kohlhage and Yager, 1994). A rowing type motion then corresponds to an appendage stroke that is along the direction of the flow or net thrust. It should be noted that rowing strokes and mechanisms are also possible at higher Re

(the oar of a rowboat being a classic example), but under these cases it is the inertia reaction of the fluid, and not viscous forces which are responsible for the thrust. Typically, it has been observed that flapping motions are more prevalent for high Re conditions, as speculated for a net gain in efficiency (Walker, 2002; Walker and Westneat, 2002).

It may be useful to consider the shift from rowing to flapping in a single aerial or aquatic organism as being analogous to some gait changes observed in terrestrial systems, where legged animals alter their motor pattern with increasing speed to increase the energetic efficiency of travel (Hoyt and Taylor, 1981; Alexander, 1989; Heglund et al., 1974; Heglund and Taylor, 1988). Previously, certain transitions in swimming mechanisms have also been referred to as ‘gait’ changes, notably the continuous to burst-and-coast swimming (Weihs, 1974; Videler and Weihs, 1982) and pectoral to caudal fin powered swimming (Cannas et al., 2006; Drucker, 1996) in fish. Such aquatic transitions have been identified only in organisms operating at relatively high Reynolds numbers ($Re > 100$). To our knowledge, no shifts between rowing and flapping have yet been identified within a single appendage set during over changes in propulsive speed or over ontogeny, even though multiple studies predict that such a shift should occur.

The nymphal mayfly, *Centroptilum triangulifer* (Ephemeroptera, Baetidae), grows through the intermediate Re regime while maintaining an array of seven pairs of plate-like gills. Kinematic analysis of high-speed (1 kHz) videos revealed an apparent gait shift near frequency Reynolds number $(Re_f) = fL_g^2/\eta = 5$, which consisted of a transition of high to low asymmetry in several stroke parameters. Both the magnitude of the range of gill pitch and deviation from the mean stroke plane

decreased abruptly with increasing Re . These changes in gill-plate kinematics were accompanied by the development of a passively oscillating distal flap and a significant shift in net flow from a direction approximately parallel to the stroke plane to one more perpendicular to the stroke plane. These ontogenetic transitions suggest a possible hydrodynamic limit at low Re in early instars that is reflected by a relatively rapid switch between two gaits corresponding to the basic categories of rowing and flapping. This result is consistent with simulation- and model-based results predicting a rapid rather than gradual change in appendage kinematics with gradually increasing Re .

2.B Materials and Methods

2.B.1 Study organism and cinematography

On days 20, 21, 23, 25, 27, 28, 35, and 42, a nymph was taken from cultures and used for 3D kinematic analysis, with two nymphs selected on day 25 (Table 1). The examined size range was 2.0-5.6 mm in length. Animal body lengths reported here excluded the caudal filaments. The size of the animal increased with age, with the exception of an individual on day 25 that was slightly larger than the nymphs sampled on both days 27 and 28. Nymphs emerged from the water and molted into a gill-less flying sub-imago soon after achieving a maximum size of about 6 mm. Individuals were also captured in the Paintbranch Creek, University of Maryland (College Park, MD) in August-October 2006. Only laboratory-reared nymphs ($n=9$) were used in the 3D kinematic analysis. Wild and laboratory cultured nymphs were not qualitatively different in gill kinematics across corresponding animal sizes, and hence both laboratory reared ($n=5$) and wild caught nymphs($n=8$) were used in the low field imaging trials to characterize changes in flow patterns as a function of Re_f .

2.B.2 Experimental set up

Nymphs were removed from water and dried for about 1 min on tissue paper. The tip of a minuten pin was dipped into cyanoacrylate (SuperGlue) and attached dorsally to the nymph's thorax. The other end of the pin was embedded in a mound of petroleum jelly that had been affixed to one wall of a 20x20x20-mm chamber constructed from glass microscope-slide covers. Nymph orientation inside the chamber was manipulated using forceps to position the pin relative to the jelly, so as to suspend the nymph at a typical resting distance from the bottom of the glass chamber and at least 7 mm from the dorsal and lateral walls. The chamber's free surface was then covered with a microscope-slide cover so that a complete seal was formed. Temperature of the water in the chamber was $20\pm 2^\circ\text{C}$, and nymphs initiated periods of ventilation as the oxygen diminished. In the case of the small nymphs, this occurred in about 1 hour, while large nymphs often began ventilation immediately.

Lateral and dorsal images (4 x 4 mm field of view) of the ventilating array were captured by two synchronized cameras (Phantom v9, 1632 x 1200 pixels; V.4, 512 x 512 pixels) operated at 1000 fps and attached to Leica dissecting microscopes (30 x magnification zoom lens). The cameras were adjusted to nominally orthogonal viewing positions (within 5 degrees). Nymphs were front illuminated for each camera view with two Leica gooseneck lamps (each lamp box with two fiber optic necks, and a 100 W incandescent bulb). The four fiber optic collimators were positioned about 3 cm from the water chamber. A separate glass chamber containing

animal age (days)	L_a (mm)	L_g (mm)	L_{rs} (mm)	f(Hz)	Re_f	α mean gill 4 (°)	α range gill 4 (°)	α range gill 4 (°) S.D.	$\Phi_{max}-\Phi_{min}$ (°)	$\Phi_{max}-\Phi_{min}$ S.D.	β (°)	ϵ (°)	γ range (°)	γ range (°) S.D.	θ range (°) gill 4	phase lag gill 4-5
20	2	0.25	0.16	34	2.1	70	37	3.4	30	0.9	55	81	16.54	2.41	13.11	0.26
21	2.30	0.3	0.17	26	2.3	71	36	1.9	49	1.2	52	80	18.16	2.93	11.55	0.19
23	2.90	0.5	0.24	20	5.0	60	23	3.5	40	0.2	65	79	23.87	0.4	7.61	0.28
25	3.15	0.65	0.24	20	8.4	93	10	0.9	36	0.7	68	87	40.62	1.75	3.05	0.16
25	3.50	0.51	0.24	25	6.5	87	9	0.5	40	0.4	57	74	64.26	3.55	5.01	0.17
27	3.29	0.58	0.23	25	8.4	100	4	1.6	31	1.2	77	79	43.04	4.89	4.16	0.17
28	3.33	0.65	0.23	29	12.2	104	11	1.8	28	2.4	60	80	57.64	9.48	4.13	0.18
35	5.18	0.82	0.39	30	20.1	87	10	0.7	22	0.6	74	81	50.39	5.1	2.50	0.2
42	5.64	0.77	0.41	37	21.6	86	8	2.1	24	0.6	61	86	61	7.03	1.82	0.23

L_g =gill 4 length, L_a =animal length not including caudal filaments, L_{rs} =root separation distance,f is frequency, Re_f is frequency Reynolds number, $\Phi_{max}-\Phi_{min}$ is the stroke range,S.D. is the standard deviation of 4 strokes, β is the stroke plane inclination angle, ϵ is the stroke plane lateral offset angle, γ is the hinge angle, θ is the strokeplane deviation angle.

Table 1. Size and plate kinematic data of all nymphs examined.

a 1-mm grid provided a two-dimensional (2D) calibration image for the dorsal perspective. This 2D calibration scale was then used to define the length and width of the abdomen. The length of the abdomen then provided the scale factor for the lateral perspective. The resulting movie files were converted to “avi” format using VideoMach (Gromada, 2007) and imported to a three-dimensional (3D) motion analysis program (Motus Peak Performance, v.7). A 3D spatial calibration was performed using the animal's body (with known length and width) as a calibration object in combination with the 2D calibration described above. This nymph-based calibration object was defined as a virtual box with vertices formed by the roots of gill 2 and gill 6 on both sides of the abdomen and the height of the resting gills. The gills on the far side of the body, though out of focus in the lateral image, provided a measure of roll and yaw for the calibration box, and did not indicate any significant parallax in the camera lens system. The object space defined by this calibration was self-consistent to the extent that points could be located to within 0.001 mm in each dimension. Along with the root location (R), the tip (T), medial edge (ME), and lateral edge (LE) of each gill was digitized in each frame (see landmarks defined in Figure 4 and Figure 7). Uncertainty in the values of the kinematic parameters is derived from both the spatial calibration and landmark ambiguity of the multiple points that define each parameter. Spatial calibration and landmark ambiguity errors were quantified separately. The spatial calibration contribution was quantified by comparing the pitch angles of the same sequence of strokes before and after intentional skewing of the virtual calibration box, where the skewing was the maximum possible due to ambiguity in location of the box vertices. This resulted in a shift of pitch angle of $2.2 \pm 3.9^\circ$ (mean \pm S.D., $n=5$ pitch extrema) in the smallest

nymph and 0.7 ± 0.2 in the largest nymph. The landmark ambiguity contribution to the error was quantified by comparing the pitch angle extrema of the same sequence of strokes ($n=5$ periods) under two independent digitizations of the gill landmarks. Due to the large pitching motion of the small nymph gill plates, landmark digitization error accounted for about 18% ($-0.4 \pm 6.5^\circ$ vs 37°) of the full pitch range. Landmark digitization error produced a mean offset of the pitch in the largest nymph similar to the full pitch range at that size ($6 \pm 1.2^\circ$ vs 8°), but the pitch range itself did not change. Hinge angle in the largest nymph shifted $3 \pm 2.8^\circ$ ($n=5$ periods) due to landmark ambiguity, but less than 1° due to spatial calibration error.

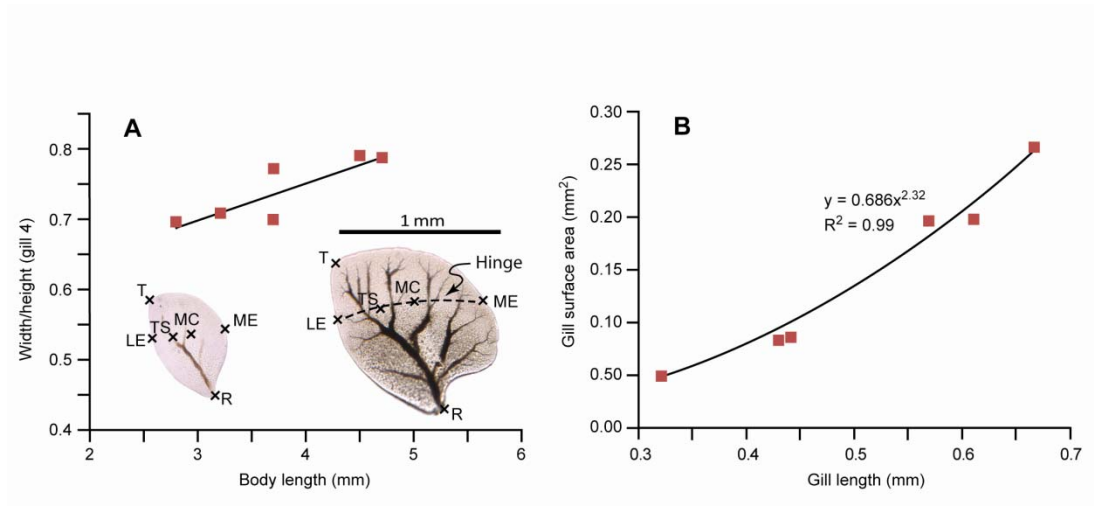


Figure 7. Ontogenetic changes in gill morphology. A. Ratio of gill 4 (width/height). B. Gill 4 surface area as a function of gill length.

After the high speed images of the animals were captured for kinematic analysis, hollow glass beads (11 μm mean diameter, Potters Industries, Grade 110P8) were added to the water for flow field analysis. Flow in the vertical plane just lateral to the abdomen was quantified using planar cinematographic PIV (1000 fps, exposure time 950 μs). We used a 400 mm (focal length) plan-convex lens and 63 mm (focal length) plan-cylindrical lens to generate a light sheet from the beam of a continuous

Argon ion laser (max. power 2 W, Coherent Innova 90). In the filming area, the light sheet was 20 mm wide and 0.2 mm thick. Framing rates of 1 kHz allowed for cyclic phase resolution of approximately 10° , with a spatial resolution of approximately 25 μm for a 3 mm field of view. This level of resolution is possible through the use of ensemble-correlation PIV (Meinhart et al., 2000), since the observed flow is ostensibly laminar and highly repeatable from cycle to cycle. An ensemble on the order of $N=10$ is typically found sufficient to converge the velocity field at the desired resolution. The size of the initial sub-image for the PIV ensemble correlation procedure was 128 x 128 pixels, and was reduced to 32 x 32 for the second and final correlation. Overlap between sub-images was 50%. The influence of light scattered by the gill plate was removed by subtracting the mean image for the local ensemble prior to computation of the correlation. Not all of the individuals used in the 3D kinematics imaging maintained a regular and prolonged ventilation sequence necessary for the ensemble-correlation, possibly due to accidental damage to the body by the laser. Therefore, we imaged the flow field of several nymphs ($n=8$, size range 1.9-5.6 mm total body length) not included in the 3D study. Altogether, the inter-gill flow field of 13 ventilating individuals was resolved through the PIV ensemble-correlation.

2.B.3 Gill-plate kinematics

The 2D raw coordinates from digitizing each perspective were Butterworth filtered (100 Hz cutoff) and transformed to 3D coordinates (Motus Peak Performance, v.7). The cutoff frequency of 100 Hz was chosen after comparison of

the raw and filtered signal confirmed that filtering above 80 Hz did not attenuate the amplitude and significant features of stroke motion. The 3D-transformed coordinates were analyzed in Matlab R2006b. The mobile gills of animals greater than 3 mm body length bend at a hinge line that demarcates proximal and distal regions of the gill. This hinge line lies approximately parallel to the horizontal x - y plane (Figure 4 and Figure 7). The medial-dorsal end and lateral-ventral end of the hinge line were clearly defined points in bending gills, which along with the gill root, provided three convenient points in which to reliably define a proximal plate for the gill (referred to earlier as the medial edge (ME), lateral edge (LE) and root (R), respectively). We digitized the analogous points in the animals with non-hinged gills (body length > 3 mm). The stroke plane (Φ) of wings in flying insects is usually defined as the plane that contains the wing root and the most anterior and posterior positions reached by the wing tip (Dudley 2000). Due to the tip flexion in the largest animals, we used the trajectory of the midchord point (taken to be the bisector of the dorsal (DE) and lateral edge (LE) points) to define the stroke plane in all the animals (Figure 4 and Figure 7). Using the strokeplane defined by the trajectory of an alternative point (TS, trachea subdistal), calculated as the bisector of the lateral edge (LE) point and the midchord point, produced slightly different kinematic results. For the smallest nymph, using the point TS rather than the midchord decreased the pitch range from 37 to 33°, and for the largest nymph, increased the pitch range from 8 to 12°. The stroke plane can be described by an inclination angle (β) and lateral offset angle (ϵ), where β is the angle between the stroke plane and the x - y (coronal) plane, and ϵ is the angle between the stroke plane and the y - z (sagittal) plane (Figure 2). The x - y (coronal) plane of the animal was specified as that containing the roots of gill 2 and

gill 6 on both sides, while the y - z (sagittal) plane was specified by the roots of gill 4 of both sides, and the dorsal and ventral abdominal surfaces associated with gill 4. Pitch (α) was defined as the angle between the stroke plane (Φ) and the plane formed by the proximal plate of the gill, measured in the plane orthogonal to both surfaces. Stroke plane deviation angle (θ) was the angle between the root-midchord line and the stroke plane (Φ), and was considered to be positive if medial to the stroke plane, and negative if lateral. The hinge angle (γ) was the angle between the proximal and distal gill plates. This quantity was reported even for the three smallest animals that had no visible hinge line, and minimal, if any, bending. In the case of the three smallest animals, any variation of the hinge angle from 0° primarily represented the accumulated error produced by the digitization of the three points that defined the distal plate. Phase lag was calculated by auto-correlating the time-varying kinematic parameters (pitch and stroke angle for the three smallest nymphs or hinge and stroke angle for the five largest nymphs) between adjacent gills over 4 stroke cycles. We report the average of these two measures of phase lag.

Frequency Reynolds number (Re_f) was derived from the gill length in mm (L), oscillation frequency in Hz (f) and kinematic viscosity in cSt (η): $Re_f = L^2 f \eta^{-1}$ (Borrell et al., 2005). We performed linear regression analyses to determine the effect of size on all the kinematic parameters using both Re_f and body length as the independent variable (Microsoft Excel 2005).

One key element in any drag-based mechanism is an asymmetry in stroke mechanics, such that the net force on the appendage results in a non-zero thrust over a complete cycle. To assess the potential for drag asymmetry between half strokes for individual gills, we calculated a volumetric sweep rate:

$$VSR = [A_{prox} \mathbf{n}_{prox} + A_{flap} \mathbf{n}_{flap}] \cdot \mathbf{v}$$

where \mathbf{n} is the unit normal vector of the gill plate surface (the gill has been divided into a *proximal* plate and a distal *flap* surface), A is the surface area of the given portion of the gill plate, and \mathbf{v} is the velocity of gill plate at the mid-span position. It should be stressed that this is a purely kinematic quantity that was constructed to display the combined effects of orientation and velocity, as it is difficult to make a direct kinematic connection to the drag within the range of Reynolds numbers under consideration. This is due to the different scaling required by the viscous and inertial limits: in the creeping flow limit, drag is directly proportional to the viscosity, length, velocity and orientation, $F_D(Re \rightarrow 0) = f(\mu, l, v, \alpha)$; whereas in the inertial limit, it depends on the density, area, square of the velocity and orientation; $F_D(Re \rightarrow \infty) = f(\rho, l^2, v^2, \alpha)$. For these reasons, the drag coefficients and velocity exponents required to quantify the relationship between kinematics and drag must be determined individually for each case, so that drag cannot be immediately determined by speed and frontal area alone. Nevertheless, VSR highlights the potential for drag asymmetry between half strokes, due to its combination of length, velocity and orientation. The ratio of the integrated VSR between the powerstroke and return stroke is an additional measure of half-stroke asymmetry.

To confirm that the stroke patterns were not artifacts of mechanical restraint, lateral wall effects, or the genetic strains of the animals, 22 nymphs (1.7-6.1 mm body length) were captured in the Paintbranch Creek, University of Maryland (College Park, MD) in August-October 2006, and high speed images were taken within 24 hours while the unrestrained nymphs ventilated in a 1-cm-deep petri dish. The gill

kinematics of all nymphs less than 2.5 mm head-to-tail length (n=4 out of 22 nymphs, 31-45 Hz, Re range ~2-3.8) could be easily classed as having high-pitch movements and low-hinge amplitude in comparison to the larger animals from the sample, which was qualitatively similar to what was noted in the detailed kinematic analysis.

2.B.4 Gill-plate morphology

Nymphs from laboratory petri-dish cultures were killed in EtOH and dissected. Gill 4 from each animal was placed between a microscope slide and coverslip and photographed (Diagnostic Instruments Spot32 camera on a Leica compound scope, 100x total magnification) before the alcohol evaporated. A length scale was captured by separately photographing a Leica stage micrometer with 1- μ m markings. Length, width, and surface area were measured for each gill (Adobe Photoshop V10.0). The aspect ratio, $AR = L_g^2/SA$, where gill length L_g and surface area SA were determined for each gill.

2.C Results

2.C.1 Generalized kinematics of the gill array

Suspended nymphs attempted to grip the glass substrate with their legs and occasionally tried to walk. Swimming was observed, which was manifest by dorsal-ventral undulation of the abdomen with the gills retracted and held tightly against the abdomen. When not swimming, gills were always held in the fully protracted (most anterior) position and occasionally initiated ventilatory movement. During

ventilation, the body was typically held in a dorsal concave position, with the head and most posterior abdominal segment raised about a half-abdomen width higher than the middle abdominal segments (Figure 4). At rest, the seven gill pairs extended from the abdomen, so that the root-midchord segment was oriented at a stroke angle of about 0° (Figure 4). Gill movements were always bilaterally symmetrical; the gill pair of each segment always moved in synchrony. Gill 7 (the most posterior gill pair) was never actively moved during ventilation and retained its approximate resting posture. Ventilation was always initiated with retraction of gill 6. Gill 5 began retraction once gill 6 reached its most posterior position. The metachronal wave of activation traveled anteriorly to gill 1. The first retraction of gill 2 occurred in near synchrony with the second retraction of gill 6. The range of each stroke increased gradually, and required six and 11 full strokes in the two largest nymphs to achieve steady state, but only three cycles in the smaller nymphs. Duration of the ventilation activity continued for several dozen strokes up to indefinitely long periods of time. Gill 7 oscillated through only a small range of movements ($\Phi_{\max} - \Phi_{\min} < 5^\circ$ and pitch $< 10^\circ$) that was likely a passive response to the fluid motion produced by gill 6. Using animal length instead of Re_f as the independent variable in the regression did not change the statistical significance of any of the tests, therefore we report the statistical results for only one of these independent variables.

Oscillation frequencies ranged from 20-36 Hz (Table 1), with no significant trend associated with Re_f ($r^2 = 0.23$, $F_{1,7} = 2.11$, $p = 0.19$). The phase lag between adjacent gills also did not change significantly with Re_f , varying between $0.17 - 0.26$ ($61^\circ - 94^\circ$) ($r^2 = 0.01$, $F_{1,7} = 0.08$, $p = 0.78$). Stroke plane inclination of gill 4 was $\beta = 63 \pm 8^\circ$ (range 52° to 77°) across animals and did not change with Re_f ($r^2 = 0.17$, $F_{1,7} =$

1.49, $p = 0.27$). The lateral offset angle of the stroke plane from the sagittal plane was $\varepsilon = 6 \pm 16^\circ$ (range, -19° to 28°) ($r^2 = 0.007$, $F_{1,7} = 0.05$, $p = 0.83$). Both the transient and steady-state stroke kinematics were usually repeatable, but occasional digressions occurred in isolated gills in some individuals. These unusual strokes consisted of slightly higher or lower stroke ranges (change on the order of 10°) and/or slightly delayed phasic activation. For the individual of day 21 (body length 2.3 mm), gill 2 exhibited high magnitude stroke at initiation and then consistently lower magnitude strokes thereafter, and for the nymph of day 42 (length 5.6 mm), gill 1 had an unusual stroke after about every 10 strokes. We performed statistical analysis only on stroke sequences that were repeatable to the extent that inter-stroke variation was less than the digitization error. The kinematics of only steady-state sequences are reported here. The nymphs used at least two different ventilation strategies as a function of Re_f , with the largest and smallest nymphs exhibiting the extreme development of each strategy, and hence described in detail here. One nymph of intermediate size ($Re_f = 5$) was identified as potentially mixing strategies in our 3D study (intermediate level of pitch variation but no hinge development), and several other unrestrained animals of intermediate size used such intermediate kinematics while ventilating in the petri dish.

2.C.2 Kinematics specific to nymphs with $Re_f < 5$

Gills 2-6 underwent large changes in pitch during the stroke by rotating about the root-tip line (Figure 8 C,I). During gill retraction (posterior-ventral movement), the flat posterior surface of the plate was presented more or less orthogonal to the direction of gill travel, reaching a peak angle of about $\alpha = 90^\circ$ and then gradually

decreasing pitch in preparation for protraction. During protraction the gill continued to decrease pitch until about halfway through protraction, at which time it reached the minimum pitch of about 55° . The gill executed protraction (anterior-dorsal travel) while moving with a more positive stroke plane deviation angle (θ) (Figure 8 B, Figure 10 A). Any bending along the long axis of the gill was minimal ($\sim 17^\circ$); approximately the digitization accuracy at this small size for this parameter (Figure 8 D). Gill 1 was a shaft-like structure that participated in the metachronal rhythm but with small amplitude of motion. Both VSR and integrated VSR ratio were highly asymmetric between half-strokes (Figure 10 A, Figure 9 F), which is a reflection of the strong asymmetries in pitch and stroke velocity between half-cycles. Water flowed from the dorsal to ventral side of the gill array (Figure 11 B), with visual observation also indicating a significant lateral flow component as the fluid exited the array.

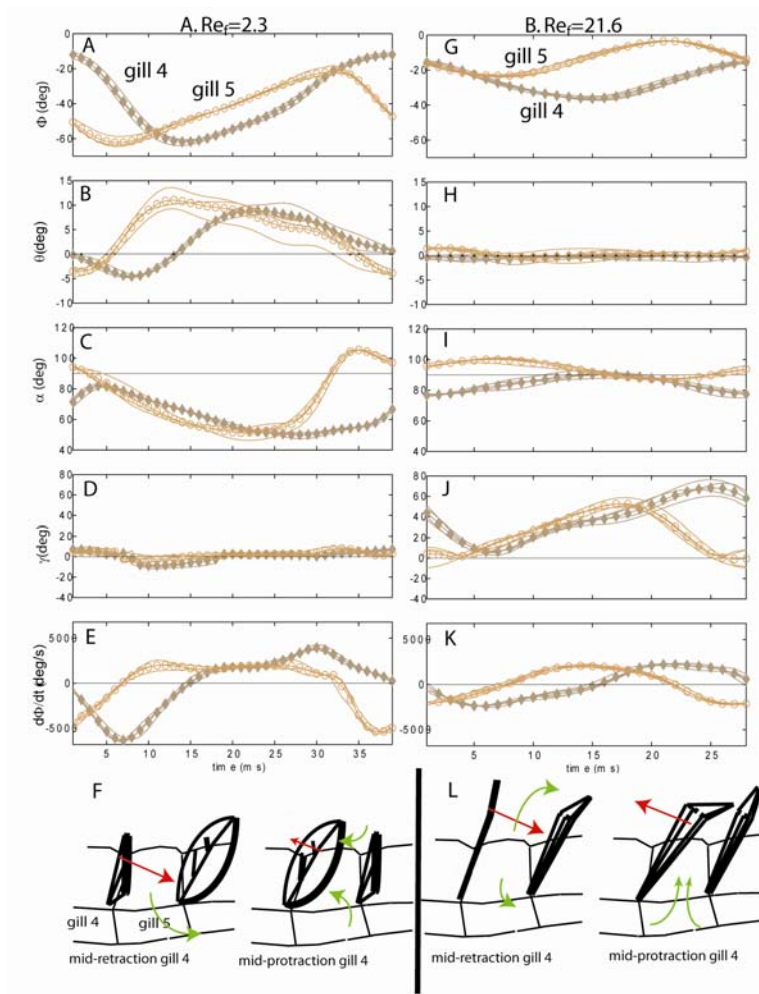


Figure 8. Kinematic parameters for gill 4 (brown) and gill 5 (orange) over a stroke cycle. Initiation of retraction of gill 4 marks time=0 ms. Stroke angle angular velocity is negative during retraction. Re_c number is that associated with the space between the gill indicated and its posterior partner. Thin lines represent individual strokes, while thick or dotted line represent mean of individual strokes ($n=4$). Curved green arrows represent the mean flow at that phase, while straight red arrows indicate gill velocity at that phase. A-F. $Re=2.3$. G-L. $Re=21.6$.

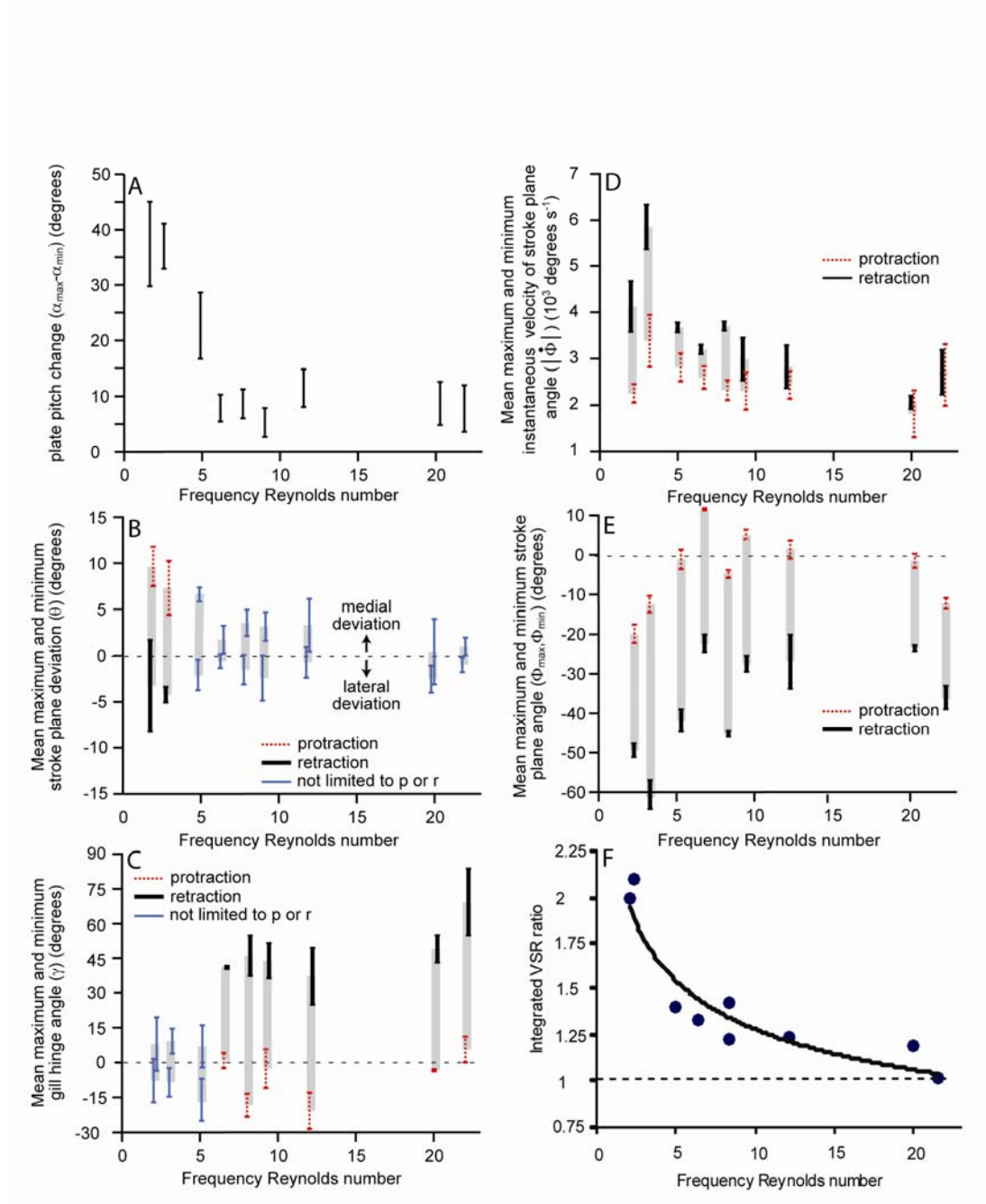


Figure 9.

A-F. Mean kinematic parameters for gill 4 plotted as a function of frequency Re number (Re_p) for nine individuals. Means were determined from 4 strokes; error bars indicate ± 2 S.D. Extrema indicated by red error bars occurred entirely during protraction; extrema indicated by black error bars occurred entirely during retraction; extrema indicated by blue error bars occurred at various points in the stroke and were not limited to either protraction or retraction.

2.3.3 Kinematics specific to nymphs with $Re_f > 20$

Nymphs had broad gill plates that retracted and protracted with a relatively constant high-pitch position ($\alpha \sim 90^\circ$, Figure 8 J) and at the same peak speed between halfstrokes (Figure 8 M). The gills had a distinct transverse hinge (Figure 4 D) that created a distal flap, which pointed toward the posterior of the animal when the gills were not oscillating. Resting hinge angle (γ) in the four oldest animals increased from 8° - 29° , but were not significantly correlated with animal length ($r^2 = 0.51$, $F_{1,2} = 2.1$, $p = 0.28$). During ventilation, the flap appeared to move passively under the combined influence of active gill movement and hydrodynamic forces. The flap was generally parallel to the proximal plate during retraction, thereby presenting a large projected surface area in the direction of travel, and the flap was bent during protraction so that less area was presented to the travel direction. The stroke range ($\Phi_{\max} - \Phi_{\min}$) of gill 1 was similar to that of gills 2-6. VSR in these nymphs was only 10% higher during retraction than protraction, and the slight difference was due primarily to hinged motion of the distal flap (Figure 10 C). Net flow was directed from the substrate and up through the gill interspaces, and then continued upward with a posterior component, so that an exit jet pointed backward and upward at about 45° to the substrate (Figure 11 A).

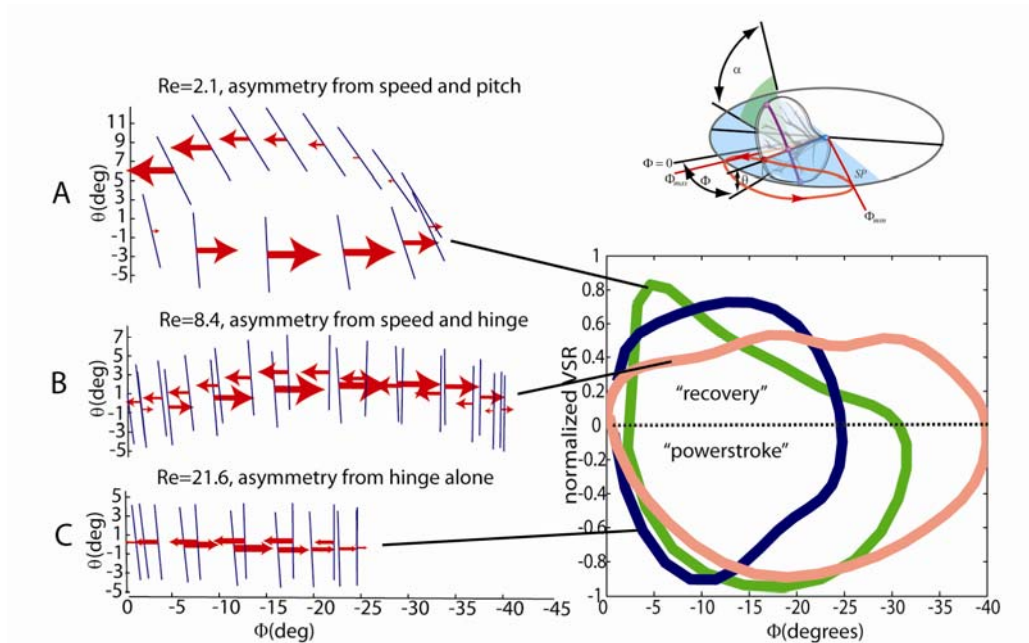


Figure 10.

Volumetric sweep rate, defined as $VSR = [A_{prox} \mathbf{n}_{prox} + A_{flap} \mathbf{n}_{flap}] \cdot \mathbf{v}$, where A and \mathbf{n} are the plan area and unit normal vectors of the gill plate sections (*proximal* and *distal flap*) and \mathbf{v} is the mid-span velocity of the gill. The inset figures on the left show the orbital trajectories of the gill relative to the stroke plane for three different Re_f cases. The orientation of the gill is indicated by the thin line, while the size of the red arrow gives the magnitude of the VSR at the indicated position. The graph on the right depicts a VSR as a function of stroke angle for each of the three cases given. Each case is normalized by its respective maximum VSR magnitude to facilitate relative comparison in stroke symmetry.

2.C.4 Gradual and abrupt changes between $Re_f > 20$ (large) and $Re_f < 5$ (small) nymphs

Significant changes over ontogeny occurred in pitch (α), hinge angle (γ), stroke plane deviation (θ), and retraction angular velocity. The intermediate animal size range of 2.3-3.1 mm ($8.4 > Re_f > 2.3$) marked abrupt changes in several of these parameters. The range of pitch motion over a stroke ($\Delta\alpha = \alpha_{max} - \alpha_{min}$) decreased from 37° to 8° , with instars rapidly decreasing pitch motion over the earliest gilled instars (full dataset linear regression marginal significance, $r^2 = 0.43$, $F_{1,7} = 5.3$, $p = 0.06$, linear regression for distribution of smallest 6 instars only, $r^2 = .94$, $F_{1,4} = 62$, $p = 0.001$) (Figure 9 A). Small nymphs ($Re_f < 5$) utilized a high pitch (90°) during

retraction and a significantly reduced pitch (55°) during protraction, while the large nymphs did not deviate far from $\alpha = 90^\circ$ (Figure 8 J). Bending at the gill hinge (γ) increased from $17 \pm 2^\circ$ to $61 \pm 7^\circ$ ($r^2=0.54$, $F_{1,7}=8.3$, $p=0.02$) (Figure 9 C), with an abrupt increase in bending at $Re_f > 6$. Bending was not symmetric about the hinge but was more acute with increasing Re_f ($r^2=0.65$, $F_{1,7}=11$, $p=0.02$), with the maximum flexion angle ranging from 10° at $Re_f=2.1$ to 68° at $Re_f=21.6$. Stroke-plane deviation (θ) decreased with Re_f from $10 \pm 3^\circ$ to $0 \pm 2^\circ$ (Figure 9 B).

Several parameters (ratio of peak protraction to peak retraction speed and the range of stroke motion) changed gradually with Re_f over the entire range of study. Peak angular speed of retraction decreased with increasing body length, while protraction speed was relatively constant, a pattern that resulted in equal peak protraction and retraction speeds in the largest animals (Figure 3 D). The ratio of peak protraction to peak retraction speed increased gradually with Re_f ($r^2=0.75$, $F_{1,7}=21$, $p=0.003$). Stroke range ($\Phi_{\max} - \Phi_{\min}$) decreased gradually with Re_f ($r^2=0.61$, $F_{1,7}=11$, $p=0.013$) (Figure 9 E).

At nymphs operating at $Re_f < 5$, VSR was about 100% greater during the retraction “powerstroke” than during recovery (Figure 10 A), and this was due entirely to the high speed and pitch during this stroke phase. At Re 6-12, a powerstroke during retraction occurred due to both distal flap straightening and higher speed (Figure 10 B). At $Re > 20$, the distal flap was the only source of the slight asymmetry in the VSR, where the distal flap straightening produced only about a 25% increase in the VSR during the “powerstroke” compared to “recovery” (Figure 10 C). While the VSR may be underestimating the drag differences over half strokes

at this high Re , the reduced asymmetry in this index is suggestive that any rowing mechanism plays a less important role as animals grow.

Finally, use of the PIV results allows one to determine a quantitative value for the mean flow direction, and hence provide a more complete classification of the rowing or flapping kinematics. Individual graphs (Figure 11) of the mean flow field were discussed above for the extreme cases, and the results of the net flow direction relative to the stroke plane is shown in (Figure 12) for the full range of Re_f studied. Here it can be seen that the flow direction is nearly constant at approximately 60° for $Re_f > 8$, but decreases sharply below this Reynolds number, giving values that rapidly become more aligned with the stroke plane (0°).

2.C.5 Morphological results

The number of tracheal branches and medial lobe extension increased during ontogeny. Gills became wider with body length ($r^2=.75$, $F_{1,4}=12$, $p=0.03$)(Figure 7), corresponding to a decrease in aspect ratio from 2.1 to 1.65 ($r^2=$, $F_{1,4}=2.3$, $p=0.2$). Gills increased in surface area four fold over a two fold increase in animal length ($SA=0.68 L_g^{2.3}$, $r^2=0.99$).

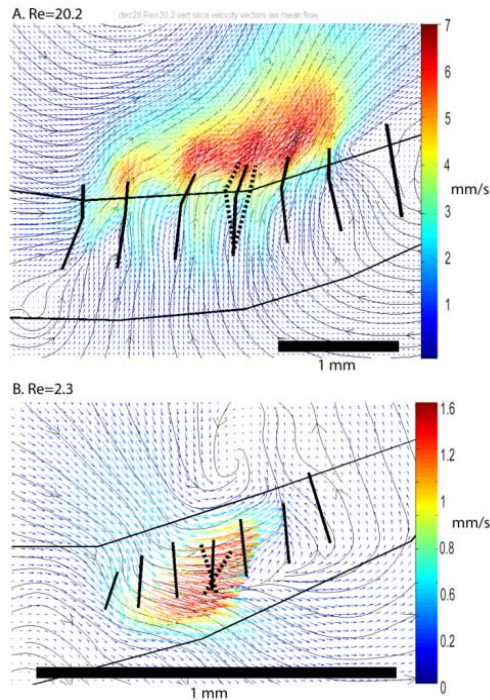


Figure 11.

A. Flow field through and around the gill array in the vertical plane quantified by ensemble correlation PIV for $Re_f=20.2$. Mean gill positions over a stroke cycle for gills 1-7 and abdomen outline shown by solid black lines. Gill 4 protraction and retraction maximal positions shown for both the proximal and distal plates as dotted lines.

B. Flow field through and around the gill array in the vertical plane quantified by ensemble correlation PIV for $Re_f=2.3$. Mean gill positions over a stroke cycle for gills 1-7 and abdomen outline shown by solid black lines. Gill 4 extreme protraction and retraction positions shown as dotted lines. There is no measurable flexion about a hinge in any of the gill plates at this Re_f .

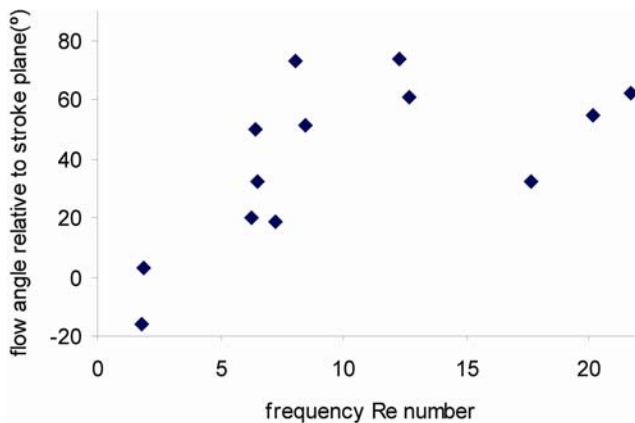


Figure 12. Change in flow direction as a function of Re_f for 13 individuals. Mean flow direction was calculated as the average of the flow over the entire imaged area. A 90 degree angle is expected for an idealized flapping stroke, and a 0 degree angle for an idealized rowing stroke. Flow angle increases with Re_f ($r^2=0.76$, $F_{1,7}=22$, $p=0.002$, linear regress on $Re_f < 12.3$), ($r^2=0.37$, $F_{1,11}=6.3$, $p=0.03$, linear regress on all Re_f). (5/9 individuals from the 3D kinematics study were included in this graph (Re_f 2.1, 8.4, 12.2, 20.2, and 21.6). The remaining individuals (8/13) depicted were collected from the wild.

2.D. Discussion

Comparative studies have revealed general patterns in the way that stroke kinematics vary along the spectrum of intermediate frequency Reynolds numbers (i.e. $1 < Re_f < 100$) (Walker, 2002), with exclusive use of rowing occurring at the low end and flapping predominating at the high end. Studies of individual species that transit this Re range, either through ontogeny or with changes in speed, indicate that animals either row with a single set of appendages with changes in stroke kinematics or they use two separate appendage groups at different Re . For example, remipede crustaceans use one set of appendages to perform both a metachronal stroke for cruising or hovering and a synchronized ametachronal stroke pattern for escape (both at approximately $Re_f \sim 2$; (Kohlhage and Yager, 1994). The copepod *Temora longicornis* forages using an equi-phase metachronal rowing stroke with its five feeding appendages ($Re_f \sim 1$), but rows with its swimming legs during escape with a metachronal power stroke and synchronized recovery stroke ($Re_f \sim 10$; (van Duren and Videler, 2003)). Finally, the free-swimming mollusc, *Clione antarctica*, uses ciliary bands for low velocity movement and two flapping pteropodia for higher velocity locomotion, with the lower bound for flapping occurring at $Re_f \sim 10$ (Childress and Dudley, 2004).

The mayfly *C. triangulifer* appears to be unique in exhibiting a change in both kinematics and hydrodynamic mechanism while using a single set of appendages as they grow. Specifically, *C. triangulifer* shows a kinematic transition between a rowing and flapping mechanism over a narrow range of development as Re_f changes from approximately 3 to 8. This transition consists of several distinct kinematic and

morphological changes: the formation of a passive hinge that increases gill flexion (Figure 9 C), a dramatic decrease in pitch variation throughout the cycle (Figure 9 A) and a decrease in the stroke plane deviation (Figure 9 B). However, some kinematic parameters do not change [cycle frequency (Table 1), inter-gill phase (Table 1), speed of protraction (Figure 9 D), and pitch during retraction] or change gradually [stroke angle maximum and minimum positions and speed of retraction]. In order to better place this behavior in context, it is useful to compare our observations with other animal systems at both extremes of *C. triangulifer*'s range.

At the lower range of the Reynolds number scale ($Re_f < 5$), there are numerous examples of other multi-appendage array animals that use rowing stroke kinematics for propulsion, such as copepods (van Duren and Videler, 2003), remipedes (Kohlhage and Yager, 1994), ctenophores (Barlow et al., 1993) and *Artemia* (Williams, 1994a; Williams, 1994b). A common feature among these examples is a change in appendage shape or profile during the recovery stroke to minimize drag and enhance net thrust. This is accomplished through articulation of the appendage (remipede), actuated flexion (cilia in the ctenophore) or retraction of setae on the limb (*Artemia*, remipede). In the case of the mayfly at this Reynolds number, the gill plate is fairly stiff, with very little to no change in the plate shape throughout the stroke cycle. Instead, the asymmetry in the drag on the appendage is accomplished through a change in pitch to “feather” it during protraction (as indicated by the two times change in VSR between the power and recovery stroke (Figure 10), as well as any mutual interaction benefit derived by the phasing of the stroke with neighboring appendages. It is curious that the young mayfly nymph does not utilize an articulation to change the gill geometry, as the other animals noted do, particularly

since a hinge develops in the gill plate at the later stages of development. The simultaneous requirements of supporting a gill plate with stiffened trachea, promoting diffusion through those trachea, and producing efficient ventilatory flow must be studied further in order to understand why the use of plate flexion is limited to larger gills.

At the high end of the viscous/inertial transition range, no multi-appendage array animals have been reported in the literature to operate with a flapping mechanics. For single appendage pairs, however, there is a great deal of work on inertial-based flapping mechanisms for insect flight, and – to a lesser extent – some work on how such mechanisms behave or stop at a low Re_f limit.

Significantly, most models of lift-based flapping assume inviscid flow and a concentrated source of circulation to explain the production of lift. Given this, one would expect lift-based mechanisms to be inoperable below a sufficiently small Re_f due to rapid frictional degradation of vorticity. Indeed, the mollusc *Clione antarctica* does not use the flapping mode of locomotion below a critical value of $Re_f \sim 10$ (Childress and Dudley, 2004). Childress and Dudley (2004) constructed an idealized mathematical model of this type of locomotion, dubbed the “Venetian blind” model, which assumed a symmetrical, time-reversible stroke motion, and found that a critical bifurcation occurred at around the same critical Reynolds number observed in *C. antarctica*. Below this value, symmetric motion could not sustain a lift-based flapping mode of propulsion. Simple mechanical experiments by Vandenburg et al. (2004), supported these findings, although the bifurcation occurred at a slightly higher Re_f , possibly due to friction in the experimental apparatus. There is a striking similarity between the critical Re_f observed in the preceding studies and

those associated with the kinematic changes of *C. triangulifer*. However, several features of the kinematics and morphology in the mayfly violate assumptions of the Venetian blind model and the two systems may not be comparable. Specifically, the mayfly is not a time-symmetric system due to the phase lag between adjacent gills in the array, and morphology is not constant due to the development of the passive hinge that coincides with the transition in kinematics. Thus, the rough correspondence between predictions of the Venetian-blind model and the ontogenetic transition in mayflies may reflect common hydrodynamic factors or it may be a coincidence. Further work on an extended flapping model capable of representing the mayfly geometry is needed to distinguish these two possibilities.

Other hydrodynamic flapping mechanisms have been described in the literature, such as the Leading Edge Vortex (LEV), rotational lift, added mass and clap-and-fling models, all of which were constructed to account for the differences between the quasi-steady lift and drag forces typically found in the case of fixed-wing aerodynamics and the reality observed in the unsteady, oscillating flows generated by flapping wings (Sane and Dickinson, 2002). These mechanisms attempt to account for how vorticity (or circulation) is produced and redistributed through the flow region as a result of a fairly specific set of stroke kinematics, and so are expected to be sensitive to strong diffusion effects at a low Reynolds number. Most of these mechanisms have been noted and studied in animals that operate at much higher Re_f (typically $>10^2$) than *C. triangulifer*, with the exception perhaps of the “clap and fling” model first proposed by Weis-Fogh (1973) in his study of the small chalcid wasp *Encarsia formosa*. As proposed by (Weis-Fogh, 1973), developed by (Lighthill, 1973), and confirmed by (Maxworthy, 1979), this mechanism uses the close proximity

of two wing elements at maximum stroke to generate a strong rotational flow as the wings are drawn apart, providing a boost in lift in the early part of the stroke. This mechanism in hovering *E. formosa* occurs for a $Re_f \sim 10$, which is similar to the upper range noted for *C. triangulifer*. The gill plates do approach each other closely and nearly touching at times, so similar mechanisms may be relevant for this animal. Further studies on the details of the time-resolved flow within the intergill space is needed to ascertain what hydrodynamic mechanisms may be operating for these conditions, and to clarify how this flow is distinguished from that generated by rowing in early instars.

2.D.1 Gill oscillation frequency scaling

Few studies have measured gill oscillation frequency in animals moving at low and intermediate Re , but systems in this regime may be relatively independent of the constraints associated with inertial resonance or vortex-shedding systems (Wang, 2000) owing to dominance of viscous effects. The independence of oscillation frequency with size in *C. triangulifer* is striking compared to flying and swimming stroke frequencies in other animals, where frequency typically decreases with size (Full, 1997). The typical decrease in frequency observed over a three-fold increase in length in high Re oscillating systems is about 50%. While the observed range in frequency and size in *C. triangulifer* was of this order of magnitude, the variation was not significantly correlated to the size, implying that the Re increased solely due to gill length. In brine shrimp *Artemia* (another aquatic system examined across a similar Re range) the frequency decreased with size by only 25% (Williams, 1994a), whereas a 75% reduction would be expected based on swimming and flight systems that operate at higher Re (Full, 1997).

Manipulation of gills in large narcotized animals (original observations) and stability in protraction speed across ontogeny (Figure 9 D) suggest that protraction may be powered by a passive elastic mechanism. Previous descriptions of the gill musculature in select species, with the goal of highlighting potential homologies in the wing/gill muscles (Brodskii, 1974; Kluge, 1989; Eastham, 1958), have cited 1 or 2 muscles at this gill articulation, but dynamic characterization of gill actuation through tools such as electromyography are hampered by the small size of the taxa. The complete retraction of the gills during swimming, flattening against the abdomen in order to reduce drag, may be a general feature of mayfly nymphs, including those species not utilizing active ventilation. As such, the protractive motion restoring the plates to upright position after swimming may be sufficiently actuated by a weak elastic mechanism. The active ventilation performed by the species in the current study could represent a derived function of the plates, in which the elastic mechanism is enhanced so that protraction is less limiting to the length of the stroke period (small instars), or potentially even provide useful ventilatory thrust (large instars).

2.D.2 The significance of the gill hinge in *Centroptilum*

Fluid-induced (passive) bending of appendages is a common feature in many wings (Wootton, 1981; Wootton, 1999; Ennos, 1988), legs (Kohlhage and Yager, 1994), and gills (Eastham, 1937; Eastham, 1936) and is critical to the mechanics of many rowing systems, where it functions to reduce the drag force during a recovery stroke and increasing the drag during the powerstroke. In insect wings, passive flexion can occur in both the chord and spanwise directions (Ennos, 1988), and wings are stiffer toward the base (Combes and Daniel, 2003). The functional significance of flexibility in flapping systems is not as obvious as in rowing, but may increase

efficiency in flexible flapping by changing camber and/or pitch. Insect wings can also combine a continuous, distributed bending over an entire wing with localized flex regions created by reduced stiffness at specific points in the wing venation. The gill plates of the mayfly nymph *Leptophlebia* flex chordwise (change camber) around the gill center shaft over a half-stroke, potentially in order to increase drag during that phase (Eastham, 1936). However, this flexion is only on the order of 20° and occurs around the center shaft.

In contrast to *Leptophlebia*, the gills of the larger instars of *C. triangulifer* represent the first reported example of a clearly defined gill plate hinge that separates the plate into proximal and distal sections (the hinge line runs diagonally from the dorsal/root edge to the ventral/tip edge, see Figure 7 A). The hinge kinematics are typically asymmetric, with a strong bias (increased bending) in the posterior direction (Figure 9 C, J). The hinge likely plays an important hydrodynamic role that may manipulate vorticity shed from individual elements, in a fashion similar to that of an undulatory swimming body (McHenry et al., 2003; Drucker, 1996). Such undulatory motion can generate transverse thrust through both circulation and/or drag mechanisms. Alternatively, the distal flap could function as the valve of a pump consisting of three surfaces (posterior, anterior and flap) and three open sides (medial, lateral and ventral). During the suction phase, fluid is drawn upward from the substrate. In the subsequent compression phase of the stroke, the water is squeezed out both in the ventral and dorsal directions, but due to the asymmetry in the suction phase, the net result is dorsal directed transport of water. A trend from peristaltic to valve based pumps does occur in embryonic development of the vertebrate circulatory and lymphatic systems (Forouhar et al., 2006). It has also been suggested

that such biological tubular pumping systems may switch from peristaltic to a valved mechanism at some critical Re range due to energetic efficiency advantages(Vogel, 1992). Work is currently in progress to examine these hypotheses by analyzing the detailed time-resolved flow between the inter-gill spaces.

Chapter 3: Phase resolved flow fields and the rowing to flapping transition

3.A. Introduction

Animals vary widely in the number, arrangement and stroke kinematics of the appendages they use to generate flows for propulsion, ventilation or feeding. The aim of biomechanical research is to explain such diversity in terms of fundamental physical principles, and some general patterns can be explained by considering the ratio of inertial and viscous forces, a value captured by the well-known Reynolds number (Re). For example, appendicular stroke kinematics are broadly divided into flapping (where net flow occurs largely perpendicular to the stroke) and rowing (where net flow occurs largely parallel to the stroke), with flapping observed to occur at $Re > 100$ and rowing predominating at lower Re . This pattern occurs regardless of the phylogenetic history or specific arrangement of the appendage system (Walker, 2002).

While comparative studies are invaluable for identifying general trends, they do not address precisely how inertial and viscous effects are manifested in flow structure or how such effects interact among and between themselves within an array of appendages. The paucity of such studies can be traced to the fact that most animals do not commonly transit this intermediate regime, but rather spend their lives on one side or the other. Those animals that do cross the intermediate regime often use a separate appendage set on either side [(e.g. ciliary to wing-like propulsion in arctic pteropod (Childress and Dudley, 2004) and antennal to leg propulsion in some crustaceans (Williams, 1994b)].

It would therefore be instructive to study a single species that transits the intermediate Re regime using a single set of appendages and undergoes a shift from rowing to flapping. Progress in understanding general patterns, such as the rowing-flapping dichotomy, requires describing flow at fine scales of resolution such as the level of individual appendages. Such descriptions have been generally limited by the technical difficulty of imaging flow at such small scales. Here we provide a detailed PIV-based description of one such multi-appendage system, the gill array of nymphs of the mayfly *Centroptilum triangulifer* (Baetidae). Our goal is to associate major changes in gill kinematics and gross flow structure with fine-scale hydrodynamic phenomena to generate more precise biomechanical explanations of general patterns, which can then be tested in *Centroptilum* and other systems. If flow structures and flow rates at the scale of the individual appendages can be resolved, basic hypotheses concerning Re -driven behavioral shifts and appendage interactions might then be tested to allow for improved understanding of functional performance and model development.

The ventilatory system of *Centroptilum triangulifer* is well-suited for this kind of investigation and it shifts from a rowing to flapping type stroke while crossing the intermediate Re range during growth (Sensenig et al., in press 2009). The animal is stationary while generating ventilatory current using a serial array of seven pairs of abdominal gill plates. Individuals grow incrementally through a Re spectrum that ranges from 2 to 22, with a rapid change in gill kinematics from rowing to flapping over the range $4 < Re < 9$. Specifically, gills in small instars use strokes with large pitch and stroke-plane deviations, and net flow is directed ventrally and essentially parallel to the stroke plane (i.e. rowing). Larger instars use strokes with minimal pitch

and minimal stroke-plane deviation, and their gills have an intrinsic hinge that undergoes passive asymmetric movement between half strokes. Net flow in larger animals is directed dorsally and essentially transverse to the stroke plane (i.e. flapping). These characteristics facilitate fine-scale analysis of hydrodynamics at the appendage level while also providing a natural and predictable sequence of hydrodynamic events, including incremental increases in Re , a dramatic change in kinematics and direction of net flow, and a gradual change in Re within a flapping system (Sensenig et al. in press).

Studies of the hydrodynamic interactions of the four wings dragonflies reveal the importance of such interactions to lift and maneuverability, but these systems reside at the upper limits of the intermediate Re regime and only involve four appendages (Somps and Luttges, 1985; Usherwood and Lehmann, 2008). The current study is among the first to resolve flow between appendages within the more extensive serial appendage arrays that tend to dominate aquatic taxa. Previous measurements of foraging and locomoting copepods (van Duren and Videler, 2003; Jiang et al., 2002; Malkiel et al., 2003) and krill (Yen *et al.*, 2003) used multi-planar time-averaged velocity fields or sparsely seeded digital holography (Jiang et al., 2002; Malkiel et al., 2003) to describe the time-average velocity field around the appendage set. This information can be used to distinguish between basic rowing and flapping mechanisms, but does not allow detailed visualization of fluid motion between appendages. In the present study, the stationary and cyclical ventilation system of the nymphal gill array permitted the use of ensemble correlation PIV, which provided highly-resolved inter-appendage flow information throughout the oscillation cycle. The resolution was sufficient for calculating temporal and spatial gradient-dependent

terms such as vorticity, so that individual flow structures could be tracked within the array itself. Comparison of fluid kinematics across the appendage array's kinematic rowing -flapping transition allowed us to assess whether the fluid kinematic transition occurred simultaneously with the behavioral transition. The transition was assessed by identifying and measuring the size and circulation strength of vortices, along with total array flow rates and flux across individual gill interspaces.

The metachronal phasing of the gill plate array produced a time-dependent array of vortices that resulted in a net ventilatory current, a fluid kinematic pattern we term a “phased vortex pump”. Our analysis indicated that fluid structure size (vortex diameter L_v) did not change significantly as animal size and Re increased. The approximately constant oscillation frequency used throughout ontogeny resulted in a similar diffusion time for vorticity generated by the plates, and hence similar diffusion lengths. At $Re \sim 15$, the vortex diameter was equal to the average intergill spacing (L_{is}) over the stroke. Consequently, in nymphs smaller than this, single vortices enveloped several gills over much of the stroke cycle, while in larger nymphs, each vortex was associated with a single plate for most of the gill stroke cycle. The relative size of the vortex and intergill space appeared to constrain the kind of flow-generating mechanisms used at each end of the ontogenetic spectrum. The phased vortex pump transitioned from rowing in nymph early stages to a later stage mechanism characterized by significant dorsal and transverse flow through individual intergill spaces. Such flow occurred at $Re > 5$ in the nymph array, and was most clearly established by $Re \sim 15$. We suggest that the rowing-to-flapping transition in multi-appendage arrays is determined by the ratio L_{is} / L_v . Specifically, we argue that effective flapping requires organized flow within intergill spaces and that this cannot

occur when vortex diameter exceeds the distance between appendages. Thus rowing should be favored when $L_{is} / L_v < 1$ and flapping should be favored when $L_{is} / L_v > 1$. Significantly, the rowing-to-flapping transition in *Centroptilum* occurs at $Re \sim 5$, when maximum dynamic intergill distance equals vortex diameter.

3. B. Materials and Methods

3.B.1 Nymph preparation

Centroptilum triangulifer is a common parthenogenetic mayfly of slow-flowing streams in eastern North America. It is multi-voltine, and nymphs can be found year-round (Funk et al., 2006). Eggs of *Centroptilum triangulifer* were obtained from a stock population at Stroud Water Research Center, Avondale, PA, and nymphs were reared at 20° C in about 1 cm of water within covered petri dishes. The water was a mixture of distilled and stream water (White Clay Creek, Avondale, Pa), and the stream water contained the nymph's primary food of diatoms and other microbial debris. The shallow water precluded the need for an aerator, and a few hours of sunlight was sufficient to maintain the diatoms. After several instars (15 days), nymphs were about 1 mm long and single lamellar gills appear on seven adjacent abdominal segments. At about 20 days, nymphs were about 2 mm long with actively oscillating gills. Nymphs were also captured in Paint Branch Creek, College Park, MD periodically throughout the year.

To prepare nymphs for flow imaging, animals were removed from the petri dish and dried for about 1 min on tissue paper. The tip of a minuten pin was dipped into cyanoacrylate (SuperGlue) and attached dorsally to the nymph's thorax. The other end of the pin was embedded in a mound of petroleum jelly that had been affixed to

one wall of a 20x20x20-mm chamber constructed from glass microscope-slide covers. Nymph orientation inside the chamber was manipulated using forceps to position the pin relative to the jelly, so as to suspend the nymph at a typical resting distance from the bottom of the glass chamber and at least 7 mm from the dorsal and lateral walls. The chamber's free surface was then covered with a microscope-slide cover so that a complete seal was formed. Temperature of the water in the chamber was recorded by periodic measurement with a digital thermometer, and was between 20-25° C. Nymphs initiated periods of ventilation as the oxygen diminished. In the case of the small nymphs, this occurred in about 1 hour, while large nymphs often began ventilation immediately.

3.B.2 PIV implementation and gill tracking

Images of the vertical plane were captured by intersecting the laser light sheet (described below) with the gill array as the animal was moved laterally into the sheet using a micromanipulator. The location of vertical slice was centered between the lateral and medial extent of the gill plates (± 0.2 mm), as indicated schematically in Figure 13. Horizontal plane images were generated by rotating the restrained animal about its longitudinal axis until the light sheet intersected the gills at the hinge line on both left and right sides, with this slice illustrated in Figure 13. We present data from horizontal planes of four individuals, and from vertical planes of 12 individuals (Table 2). Laser power was minimized during focusing and completely blocked when not needed, and maximized to 2 W during movie capture, which lasted several seconds. Three-dimensional kinematics derived from diffuse white lighting and PIV slices derived from laser illumination were compared for the same individual and revealed that the brief exposure to the laser did not significantly affect kinematics.

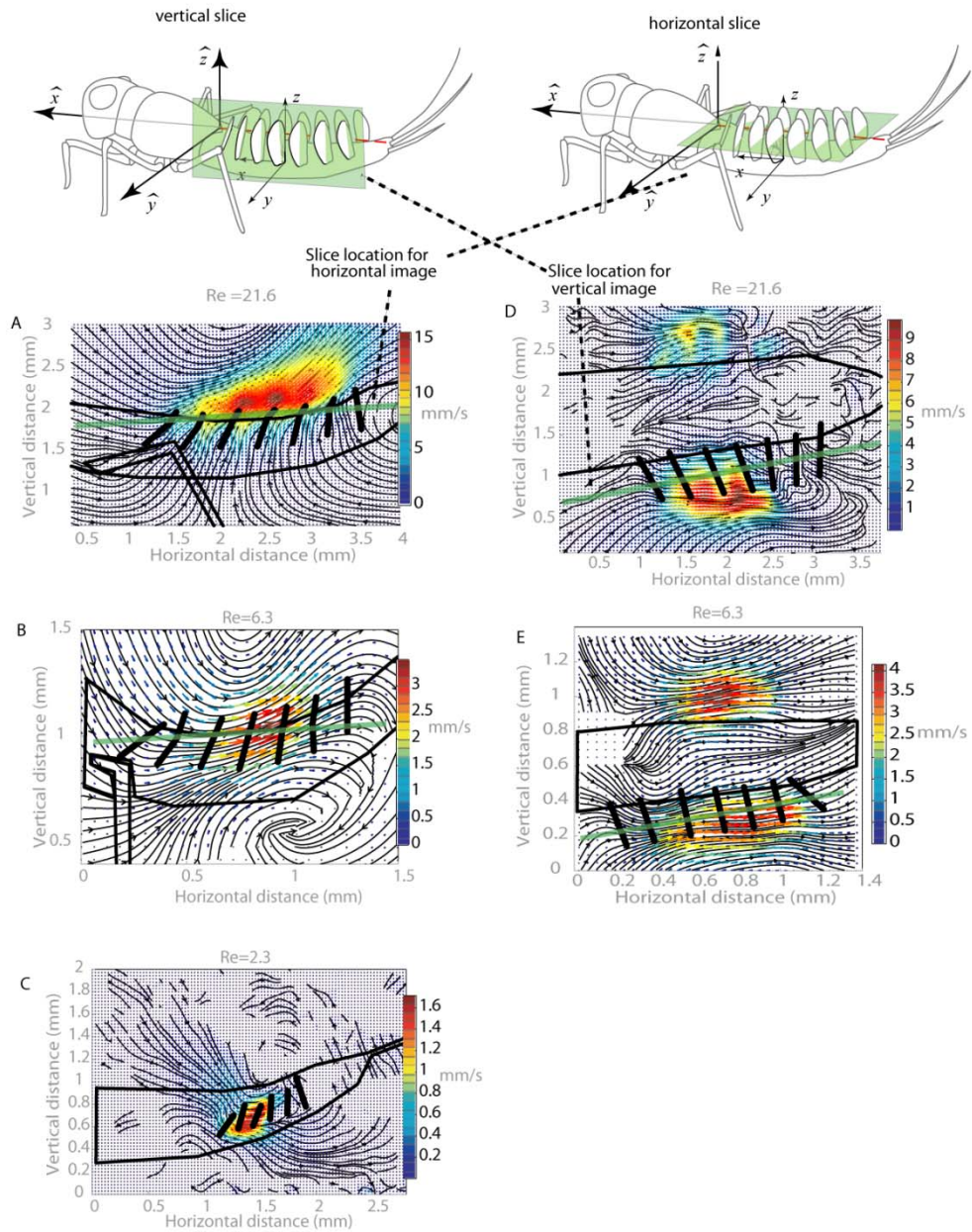
Motion in the horizontal plane was not measured using PIV at scales of $Re < 6$, but was instead observed qualitatively in full volume white (non-laser) light in both restrained and unrestrained nymphs.

Planar cinematographic PIV (1000 fps, exposure time 950 μ s) was conducted using a high-resolution CMOS imager (Phantom v9, 1632x1200 pixels). The field of view during maximum magnification of the Leica dissecting microscope was 3x3 mm, and this was used for the smallest nymphs. A field of view extending up to 9x9 mm was used for the largest nymphs. A ruler with mm markings was mounted in an identical aquatic chamber and photographed at each magnification used. I used a 400-mm (focal length) plan-convex lens and 63-mm (focal length) plan-cylindrical lens to generate a light sheet from the beam of a continuous Argon ion laser (maximum power 2 W, Coherent Innova 90). In the filming area, the light sheet was approximately 20 mm wide and 0.15 mm thick. Hollow glass beads (11- μ m mean diameter, Potters Industries, Grade 110P8) were added to the water as seeding particles, and needed to be periodically stirred to resuspend and remove them from the glass walls.

Figure 13.

A.,D. Mean vertical and horizontal flow field at $Re_f = 21.6$

B.,E.



Mean vertical and horizontal flow field at $Re_f = 6.3$, smaller resolution camera and vector spacing, total field 52x52 vectors.

C. Mean horizontal flow field at $Re_f = 2.3$, total field is 105x75 vectors

Framing rates of 1 kHz allowed for cyclic resolution of approximately 10° , with a spatial resolution of approximately $25\ \mu\text{m}$ for a 3 mm field of view. This level of resolution is possible through the use of ensemble-correlation PIV (Meinhart, *et al.*, 2000), since the cyclic flow is ostensibly laminar and highly repeatable from cycle to cycle. Ensemble-correlation PIV uses multiple frame pairs from approximately the same stroke phase to average the correlation before vector computation. Because the imaging frequency was not an exact multiple of each animal's oscillation frequency, care had to be exercised to ensure that a proper set of image frames was used to construct the ensemble. This was done by selecting an initial representative frame from the beginning of the sequence, and then searching for the best match among the possible frames that were expected to match based on the cycle frequency of the animal. The quality of the match was determined by cross-correlation of the gill plate locations within each frame. Of the approximately 30 cycles recorded in a typical imaging sequence, an ensemble of $N=10$ frame pairs was found to be sufficient to converge velocity fields at the desired resolution, and so a fairly close match within each frame could be assured. The influence of light scattered by the gill plate was removed by subtracting the mean image for the local ensemble prior to computation of the correlation. The size of the initial sub-image for the ensemble-correlation PIV procedure was 128 pixels, and reduced to 32 for the second and final correlation. Overlap between sub-images was 50%. The vector field was then conditioned both during the intermediate and final passes using the standard median filter technique with an iterative replacement of any rejected vector from secondary peaks within the cross-correlation. The mean velocity field over a complete stroke was computed by averaging the velocity at each point in the 2D space over all frames in the cycle

(varied between 21-49 frames). Assuming a conservative estimate of the sub-pixel displacement accuracy of 0.1 pixels, an interframe time of 1 ms, and a image resolution of 25 $\mu\text{m}/\text{pixel}$, the lower bound on the velocity estimation was taken to be 2.5 mm/s, which was typically 5-10% of the maximum velocity.

To map the gill positions onto the velocity field derived from ensemble correlation, the gill positions within the mean image for the local ensemble was digitized using MatLab 7.0 (MathWorks, Inc., Natick, MA, USA) by manually indicating the abdomen, legs, and ventral gill location, within-gill hinge point, and dorsal gill tip. The raw gill plate points were then smoothed in space and time using a cubic spline fit (Matlab 7.0, 'smooth'). Smoothing altered any individual point position by less than 10% of the gill length.

3.B.3 Hydrodynamic definitions

One of the most important hydrodynamic parameters in the study of oscillatory pumping or locomotion is the Reynolds number (Re), which relates the relative roles of inertial and viscosity in the governing dynamics through the definition $Re = LU/\eta$, where L is the characteristic length of the appendage or moving body, U is the characteristic velocity, and η is the kinematic viscosity. For the case of propulsion, U is typically taken to be that of the forward motion of the body being propelled, and the oscillatory nature of the appendages is introduced through the parameter of the advance ratio or reduced frequency, $k = fL/U$. For hovering flight, or stationary pumping as in the case of mayfly nymphs, the standard definition for Re becomes equal to zero, while the reduced frequency becomes infinite. In this case, it is more common to reformulate the characteristic velocity as being proportional to the

appendage oscillation frequency and span length, thereby giving a new definition of an oscillatory Re number, $Re_f = f L_g^2 \eta^{-1}$. This can also be seen as equivalent to the product of the Re number and the reduced frequency. In the current work, we take our characteristic length from the gill span in mm (L_g), the oscillation frequency in Hz (f) and kinematic viscosity in cSt (η), as adopted in similar works (Borrell et. al., 2005). Note that Re_f gives a value that is proportional, but not equivalent to, the maximum tip Re number. The exact proportionality would be altered by specific values of the stroke angle range, the duty cycle and asymmetries between the protraction and retraction stroke, and a factor of 2π .

The Re_f also has a similar form as another frequently encountered parameter in oscillating or pulsatile flows, the Womersley number, $Wo = R(2\pi f/\eta)^{1/2}$, where R a reference length dimension. In the original context, R was the radius of the channel or duct in which the pulsatile flow occurred, and as such, the Womersley number can be seen to represent the ratio of the duct half-height to the distance viscous shear forces have been able to diffuse from the wall (Womersley, 1955). Taking the reference dimension to instead represent the length of the gill, this number would be proportional to the square root of Re_f , and give an indication of the distance that locally generated viscous stresses would diffuse into the flow during one cycle in comparison to the gill size (Landau and Lifshitz, 1987). The mayfly gill array involves ontogenetic growth of appendages through a viscous diffusive length comparable to appendage length, since gill oscillation frequency change across animal growth was not statistically significant.

3.B.4 Vorticity and circulation calculation

Vorticity is a useful construct in which to study unsteady flows due to its connection to the fluid kinematics and its capacity to estimate the dynamic load on an immersed body independent of a mechanistic model. Vorticity descriptions have proven useful for bird wakes (Rayner, 1979; Spedding et al., 2003), fish (Drucker and Lauder, 1999) and insects (Ellington, 1984; Poelma et al., 2006). In particular, for situations where the vorticity is compact and distinctly organized, it can offer a potentially simpler and more convenient means for direct calculation of unsteady hydrodynamic forces (Wu, 1981). It should be pointed out, however, that in order for quantitative unsteady loading information to be calculated, the velocity field should have adequate spatial and temporal resolution as well as provide a complete description of local vorticity distribution. In the current measurements, the temporal and spatial resolution conditions are likely adequate, however, our measurements represent only a two-dimensional slice from a complex three-dimensional flow field, and hence would likely produce inaccurate results for the unsteady forces.

Here, vorticity was calculated using a second order central difference approximation (Matlab R2007b 'curl' function) on the validated (median filtered with iterative replacement of outlier vectors as noted above) velocity field data. Individual vortices adjacent to the gill plates were identified within each frame as spatial regions where vorticity exceeded 25% of the peak value observed during the complete cycle (Poelma et al., 2006). If a given vortex appeared to span more than a single gill, the identified region was segmented into smaller zones that were assigned to the closest appendage. Often times such vortices appeared to exhibit a narrowing or "pinching" between the gills, suggesting a boundary where the originally distinct vortices

produced by adjacent gill plates were diffusing into a single structure. Such features provided a natural demarcation to guide the segmentation. This was almost always the case for merging vortices in the high Re conditions, but due to increased diffusion at the low Re , such points were not readily visible. In these cases, the vortex was segmented geometrically by simply assigning regions based on proximity to a given gill plate.

Once segmented, the circulation of a given vortex region was calculated using its definition:

$$\Gamma = \int \vec{\omega} \cdot \vec{n} dA$$

which is the area integral of the vorticity that is within the specified domain ($\vec{\omega}$ is the vorticity vector, \vec{n} is the unit normal vector for the surface of integration, and dA is the scalar differential area of the surface). In our case, the flow fields are extracted in two-dimensional planes, and so the measured vorticity component is always the one normal to the observation plane. In practice, this was approximated by summing the vorticity within the given region and multiplying by its respective area. For those cases where the vorticity spanned multiple gills over multiple frames, the total circulation of the vortex was calculated and compared to the per gill “segmented” values. The peak circulation of a gill specific segmented vortex was about 15% less than the circulation of its associated non-segmented “total” vortex. Circulation values were non-dimensionalized by dividing by gill length and by the square of the gill oscillation frequency, in order to facilitate comparison among nymphs of different sizes. Non-dimensional circulation was calculated as $\Gamma/(L_g^2/f)$.

L_g (mm)	gill 2-6 root separation (mm)	water °C	f (Hz)	η	Re_f	dorsal vortex p:r circulation ratio	vortex 4 max area(mm ²)	vortex max diameter gill 4 (mm)	influx vertical (mm ² /s)	outflux vertical (mm ² /s)	outflux vertical - influx vertical (mm ² /s)	f (Hz) horizontal imaging	influx horizontal (mm ² /s)	outflux horizontal (mm ² /s)	ratio of vertical to horizontal outflux
		Vertical imaging										Horizontal imaging			
0.3	0.57	20	20	1.0	1.8	-0.33	0.040	0.23	-0.003	0.002	-0.001				
0.22	0.48	25	48	0.9	2.6	-0.60	0.026	0.18	-0.005	0.001	-0.004				
0.4	0.66	25	33	0.9	5.9	-0.42	0.108	0.37	-0.007	0.004	-0.004	33	-0.007	0.004	-0.89
0.45	0.69	25	30	0.9	6.8	-0.42	0.072	0.30	-0.011	0.008	-0.003				
0.47	0.68	20	29	1.0	6.4	-0.32	0.066	0.29	-0.011	0.011	-0.001				
0.51	0.65	20	24	1.0	6.2	-0.55	0.066	0.29	-0.019	0.016	-0.003				
0.58	0.79	20	21	1.0	7.1	-0.50	0.055	0.26	-0.017	0.018	0.002	21	-0.017	0.018	0.10
0.65	0.70	20	26	1.0	11.0	-0.62	0.073	0.31	-0.016	0.023	0.007				
0.65	0.70	20	19	1.0	8.0	-0.62	0.073	0.31	-0.016	0.023	0.007				
0.70	1.05	20	33	1.0	16.2	-0.76	0.038	0.22	-0.005	0.016	0.011				
0.82	1.28	20	30	1.0	20.2	-1.02	0.054	0.26	-0.033	0.056	0.023	29	-0.034	0.010	2.27
0.77	1.50	20	34	1.0	20.2	-0.91	0.077	0.31	-0.075	0.100	0.025	29	-0.001	0.010	2.57

Table 2. Fluid kinematic parameters of all nymphs examined.

3.B.5 Inter-gill sectional flux and time-averaged array flux calculation

The net flow produced by a given set of stroke kinematics, both as a time-averaged and as an instantaneous measure, is a useful metric to quantify pumping performance. For the case of a serial array of appendages, I was interested in determining both the flux produced by a set of two longitudinally adjacent gills to reveal the local contribution to the overall flow (inter-gill flux), and the flux associated with the entire array as a measure of net performance or total mean pumping rate.

To this end, flow through the intergill plate spaces was quantified by calculating the net flux across three distinct bounding regions of the intergill space (dorsal, mid-gill and ventral). These three bounding regions were then demarcated by defining a line connecting two homologous locations on adjacent plates at each instant in time: 1) the uppermost (dorsal) extent of the gill plate, 2) the hinge flexion points (mid-gill) visible from the motion of the plates, and 3) the lowermost (ventral) extent of the gill plate. For animals not having a distinct hinge point, the flow through the mid gill interspace was defined by a line between the mid-point of the root-tip line. The two-dimensional flow across these lines was quantified by averaging the component of the velocity vectors projected normal to that line. Dorsally directed flow was assigned to be positive, and ventral negative. Flux values were non-dimensionalized by the square of the gill length and the oscillation frequency, to enable comparison between different sized instars and different frequencies. Non-dimensional intergill flux was calculated as intergill flux divided by the normalization factor of L_g^2/f .

Uncertainty in measurements of intergill flux and circulation was estimated by the standard deviation of this parameter across typical gill interspaces of 2,3,4, and 5

($n=4$). This error can be attributed to several sources. The uncertainty in location of gill plates between which the flux was calculated would determine how many velocity vectors were included in the flux measurement. Another source of error is the uncertainty in vector magnitudes and directions across the space.

The time-averaged array flux was calculated by first defining a roughly rectangular control volume around the gill array, with the boundary located roughly 1/3 gill length from the edges of the array (Figure 21 and 22). The velocity field was then interpolated uniformly (using a bilinear operator) along the bounding edge and the local contribution to flux was calculated as:

$$\Delta Q = (\mathbf{v} \cdot \mathbf{\hat{n}}) \Delta l$$

where $\mathbf{\hat{n}}$ is the outward-pointing unit normal vector of the control volume, and Δl is the scalar incremental length along the boundary edge. The local flux was then divided into regions of inflow (ΔQ^- where $\Delta Q < 0$) and outflow (ΔQ^+ where $\Delta Q > 0$), which were summed to give a measure of the net flow rate per unit depth across the array. The difference between the magnitudes of these two sums reflects the net amount of out-of-plane flow within the specified control volume, as well as contributions from the accumulated error of the measurement.

3.B.6 Statistical treatment of gill flow characteristics

The similarity of the flow between adjacent gill spaces enabled construction of an average vorticity and flux behavior as a function of phase within each animal, by adjusting fluid and gill kinematics to a common stroke period. A dimensionless time $\tau = t/T$ was defined as the fraction of a stroke period, with the arbitrary definition of $\tau = 0$ taken to be in the initiation of retraction of gill 4. The kinematic pattern of

each gill was phase delayed with respect to its posterior neighbor, and therefore the flow features (flux through defined lines, vortices) were similarly shifted. The phase lag was measured to be between $0.20 < \Delta\tau < 0.25$, such that gills 2 and 6 were in equivalent phases of a stroke at any given time. Amplitude of the kinematics and flow features were lower for edge gills of the array. Gill 1 was located at the anterior edge of the array, while gill 6 represented the posterior edge of the mobile gills, as gill 7 was always stationary. Flow structures through gill interspace 1-2 and 6-7 were always much reduced compared to other gill interspaces (Figure 13), potentially due to both the lower kinematic amplitude and boundary effects. In order to summarize the basic fluid dynamic operation of the typical center gill plates, flux and circulation values were averaged within each animal across gills 2, 3, 4 and 5. In order to average the values of adjacent gill plates, the circulation and flux associated with each gill was phase adjusted so that the retraction/protraction phases were standardized to have a time $t = 0$ defined by the initiation of retraction of the respective gill. Variation of these parameters across gill plates within a single animal could occur due to error in aligning the light sheet parallel to the animal abdomen, different kinematic amplitude of each plate, and different plate shapes.

3.C. Results

3.C.1 General observations and steady flow field

Mayfly nymphs of *Centroptilum triangulifer* grew gill buds at about 1 mm body length, and started oscillating the gill plates when at about 2 mm body length,

corresponding to a gill length of about 0.2 mm. Gills oscillated at higher than visible frequencies of 20-50 Hz, which in early instars corresponded to a $Re_f \sim 1-2$ and for late instars to an Re_f of ~ 22 . Ventilation flow could be observed through a dissecting microscope as nymphs crawled and fed on detritus in the petri dish. The flow around the array could be deduced qualitatively from the motion of suspended detritus and numerous single-celled organisms that were entrained in the ventilation current during periodic activation of the array. Quantitative measurements were made for select individuals using PIV. Nymphs grew to about 6 mm in body length, with 1 mm long gills. Nymphs <3 mm length are hereafter typically denoted as “small” nymphs, and those >4 mm as “large” nymphs. Occasional reference is made to nymphs occupying the size range of 3-4 mm as “intermediate” nymphs. In open petri dishes, large nymphs appeared to oscillate the gills a higher proportion of time than the small instars. The small instars could be induced to ventilate more frequently by placing them with a pipette in 1-cm x 1-cm x 1-cm clear growth chamber slides for about an hour, where they could then be observed more easily in this small volume as they fed on transferred detritus. The smallest nymphs would feed and ventilate at different body orientations, occasionally even hanging upside down from the water surface of an open dish.

For the small instars (body size less than 3 mm, $Re_f < 5$), the entrained ventilation current consisted of a slow movement of water from the region dorsal to the head toward the array (Figure 13 C). Flow several gills length above the abdomen (1 mm away) was about 0.5 mm/s. Upon reaching the array, the fluid particles moved rapidly out the ventral and lateral sides of the array, reaching mean speeds of about 2

mm/s. Flow ended virtually instantaneously when the array stopped oscillating due to the high viscous forces.

Flow in the intermediate instars (3-4 mm in body length, $5 < Re_f < 10$) was oriented differently relative to the animal. Fluid was entrained equally from ventral and dorsal anterior regions of the fluid (Figure 13 B,E). In the large instars (body length 4 mm and larger, $Re_f > 10$), the current from the ventral and lateral sides of the animal and was directed away from the array in two dorsal jets (Figure 13 A,D). The animals were typically observed to position themselves in the upright position, either while chewing detritus or having recently completed a swim escape or moving from a previous detrital clump.

Re_f increased from 2.3 to 21.6 as animal size increased. Calculating a Re number using gill length and maximum speed of the gill tip was found to be about 2 times higher than the Re_f for the small nymphs due to the fast retraction phase of the small nymphs, but was equivalent to Re_f for the largest nymphs. Due to similar oscillation frequency across animal size, the calculated diffusion length of the vorticity associated with each gill was not affected by animal size, and varied between 0.2-0.3 mm. For the smallest animals, this length was equivalent to the gill length, but represented only about 1/3 of the gill length for the largest animals.

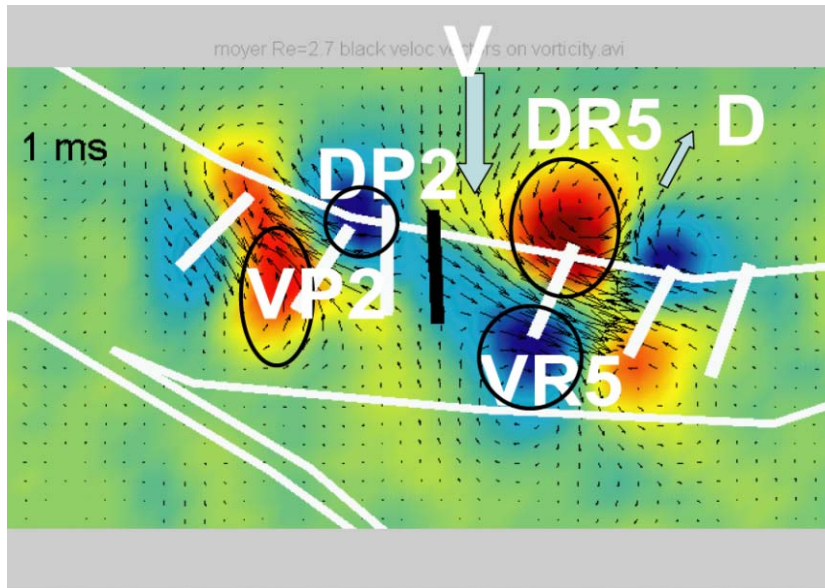


Figure 14. Vorticity at phase $t/T=0$ in small nymph $Re=2.7$. Each posterior gill is 0.25 period phase leading anterior gill. Gill bars are white, except gill 4 denoted by black bar. Individual vortices indicated by their dorsal or ventral position and protraction or retraction phase. Ventral induced flow (V) into gill 4 and 5 interspace as gill 5 retracts. Dorsal induced flow is much lower in magnitude (D). High counterclockwise circulation produced by gill 5 retraction (DR5).

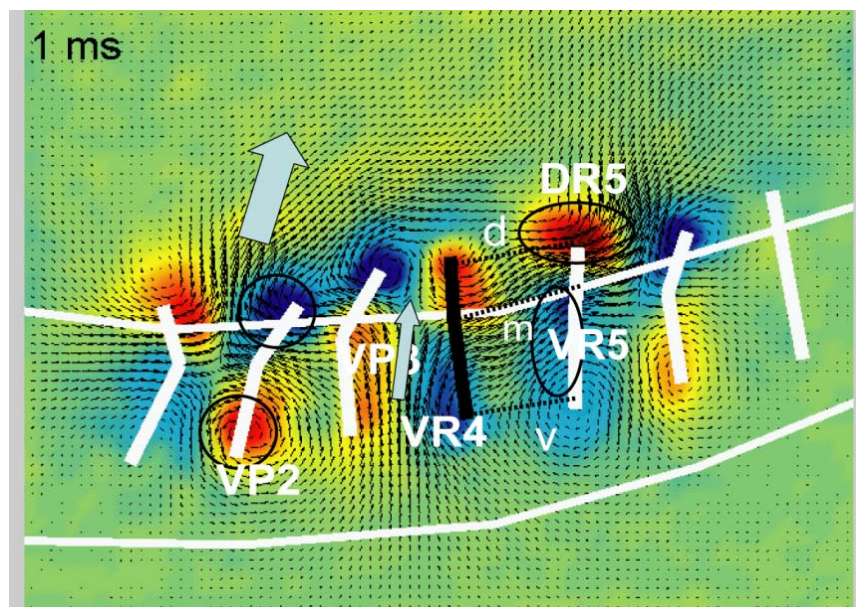


Figure 15. Vorticity at phase $t/T=0$ in large nymph $Re=20$. Individual vortices indicated by their dorsal or ventral position and protraction or retraction phase. Important fluid jet/jets indicated by large arrows. Gill 6 is midway through protraction (phase 0.6 for that gill), gill 5 is ending retraction and negative vortex VR5 is moving from proximal to distal plate (phase 0.3). Gill 4 has just begin retraction, and is generating a new negative vortex (VR4) at its leading edge. Gill 3 is nearing end of protraction, and positive (counter-clockwise) vortex VP3 is moving from proximal to distal plate. Gill 2 is midway through protraction, and in approximate synchrony with gill 6. The flow in the interspace of gill1-2 is approximately in phase with that through interspace 5-6, producing a dorsal jet D from both spaces. Lines through which intergill flux was tracked over the cycle shown as dashed lines, and labeled lower case d(dorsal),m(middle),and v(ventral).

3.C.2 Unsteady flow structure

The general features of the unsteady flow are indicated in Figure 14 and 15. In the vertical plane, the typical gill stroke cycle was characterized by generation of vortices at the dorsal and ventral edge, one at each half-stroke, the position and magnitude of which could then be tracked over the complementary portion of the stroke cycle as they advected dorsally and either decayed or were reinforced by additional production. Vortices were named for their instantaneous location on the gill plate (dorsal, D, or ventral, V), the stroke direction (retraction, R, or protraction, P) and for their associated gill number (1-6). A negative ventral vortex formed during retraction (VR-), originating predominantly at the anterior ventral edge of the plate, and a positive ventral vortex developed at the posterior edge during protraction (VP+), although the anterior/posterior distinction became much less evident by mid-stroke due to the local convection and strong diffusion at these Re_f . These vortices subsequently appeared to advect dorsally near the end of the half-stroke, and after passing the hinge flexion line at approximately the mid-stroke position, vortex VR- was designated a dorsal protraction vortex (DP-) and VP+ designated a dorsal retraction vortex (DR+). These vortices were then sustained by the continued generation of the same sign vorticity produced near the dorsal tip during the complementary half stroke. In the horizontal plane (as viewed from above the animal), vortices were clearly identified and named based on their medial, M, or lateral, L, position. Over the duration of the retraction stroke, a negative lateral vortex (LR-) and a positive medial vortex (MR+) were formed, then strengthened, and decayed. During protraction, the opposite occurs, with a positive lateral vortex (LP+) and a negative medial vortex (MR-) being formed. The distinct impression of advection of the vorticity from one side to the other at stroke reversal (at least in the

higher Re_f cases) that was noted in the vertical plane was not readily apparent in the horizontal plane.

Figure 16 follows gill 4 (center of the three pictured plates) as a stereotypical central gill of the array, and highlights the features unique to the higher Re_f nymphs ($Re_f > 20$). As gill 4 plate began retraction (Figure 16, time 1 ms), vortex VR4- (circulation negative, clockwise) developed at the ventral region of the gill plate. Furthermore, much of this vorticity appeared to be concentrated on the anterior ventral region, suggesting the role of the developing pressure gradient across gill space 3 in generating this circulation. As retraction progressed, VR4- increased in strength (Figure 16, $t/T=0.31$) and moved dorsally into the intergill space. At about ($t/T=0.45$), VR4- transitioned from the ventral side of the plate to the middle of the plate and was then designated DP4-. The gill reversed direction of the proximal plate angular travel at about mid stroke ($t/T=0.50$), and by $t/T=0.59$ vortex VR4-/DP4- had completed its move to the dorsal tip. This maintenance of circulation and identification of a single vortex of each sign for a given gill was only measured in the higher Re_f nymphs. Soon after stroke reversal, vortex VP4+ began development at the ventral edge of the plate (Figure 16, $t/T=0.59$). At time $t/T=0.72$, vortex DP4- fused with vortex DP5- associated with the approaching posterior gill.

VP4+ originated at the ventral edge of the plate during protraction, and followed a course similar to VR4-, although a half-cycle out-of-phase with VR4-. At the end of protraction, vortex VP4+ traveled upward and attached to the distal flap (Figure 16, $t/T=1$). Because a complete stroke cycle was completed at $t/T=1$, to follow the trajectory of VP4+ after this time required going through time 0. Near the end of

the retraction ($t/T \sim 0.4$), the dorsal vortex VP4+ migrated from the tip of the gill. Vortex strength was sufficiently high that VP4+ was visible for about 3 ms ($\Delta t/T=0.1$) after shedding from plate, so that at time $t/T=0.5$, two vortices of VP4+ coexisted (but phase-shifted). The same held true for VR4- at $t/T=0$. The highest circulation of a particular vortex occurred at mid halfstroke for that respective vortex; for VR4- (Figure 16 $t/T=0.17$, figure 18 A), for VP4+ (Figure 4 $t/T=0.86$, Figure 18 B).

The imaging plane for the horizontal slice was approximately at the gill 4 plate hinge (Figure 13 D), so that the vorticity measured in the horizontal plane was likely part of the vortex associated with the vertical plane images at the equivalent phases. In particular, prominent fusion of adjacent gill vorticity at time $t/T=0.76$ (Figure 17), coincided with fusion of lateral vorticity observed at the same time. Hence DR4 and DR4h were identified as the same vortex structure, with the two vortical regions identified as DR4h part of a vortex loop that enclosed the dorsal edge and more dorsal regions of the medial and lateral edge of the plate. The signs of the vortex in both the horizontal and vertical plane were consistent with formation of a 3D vortex ring.

At the end of retraction, vortex DR4h was shed laterally (time $t/T=0.45$), also corresponding to the dorsal shedding of DR4 (Figure 16, $t/T=0.45$). Therefore, the entire vortex loop was likely shed in the dorso- lateral direction. During protraction, vortex DP4h was derived from the posterior gill ($t/T=0.59$), and at the end of protraction, was transferred to the anterior gill ($t/T=1$).

Evolution of the flow field typical of the smallest nymphs is depicted at eight phases of the stroke cycle in frames with only every fourth frame shown (Figure 17). At time $t/T=0$, gill 4 was about to begin retraction, but gill 5 was in the middle of retraction. As gill 5 rapidly retracted, fluid was drawn from the dorsal side into the widening space of gill 4 (time 1 ms, Figure 14 jet V) (note that intergill space refers to space posterior to gill). As the gill plate 4 rapidly retracted (time $t/T=0.24-0.33$), large vortices were generated on both the dorsal (DR4 vortex) and ventral (VR4 vortex) edges of the gill plate. During this phase, and particularly prominent near the end of this retraction, there was prominent downward flow on the ventral side of the gill 4 space (time $t/T=0.33$), and a smaller amount of upward flow on the dorsal side as fluid was squeezed out of the gill 4 space. Near the end of retraction, vortex VR4 neared the vortex of same rotation (VR3) associated with the anterior gill. During protraction, a new vortex DP4 developed on the dorsal surface of the gill, and was derived from or briefly shared with the posterior gill DP5 (time $t/T=0.52$), before being transferred to the anterior gill ($t/T=0.71$). During this phase, vortex VP4 also was linked to DP3 of the anterior gill. For the small nymphs, the relatively large vortices associated with a gill plate were fused across several gill plates during protraction (Figure 14 vortex DP2 fuses gill 2 and gill 3) but separated during retraction of the plates (e.g. Figure 14 vortex DR5 associated only with gill 5). Vortex dissipation occurred rapidly relative to the stroke cycle so that circulation decreased to 0 between half-strokes for $Re_f 2.3$ at time $t/T=0$ and $t/T\sim 0.35$ for both positive and negative vortices (Figure 18). This contrasted with the higher Re_f cases, where the vortex was maintained as it traveled upward and did not decrease to 0

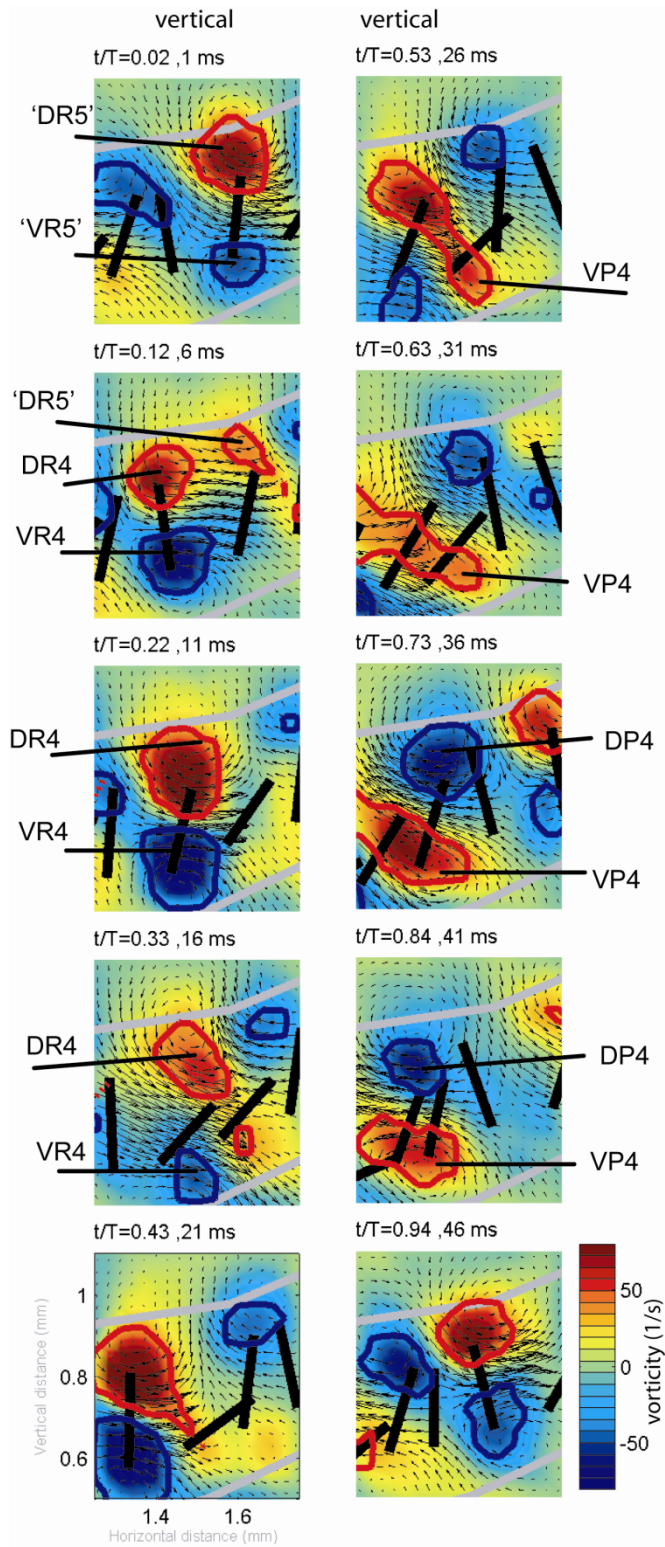


Figure 17. Phase resolved vertical plane flow at $Re_f = 2.3$. Only vertical plane flow was imaged at individuals so small that $Re_f < 5$.

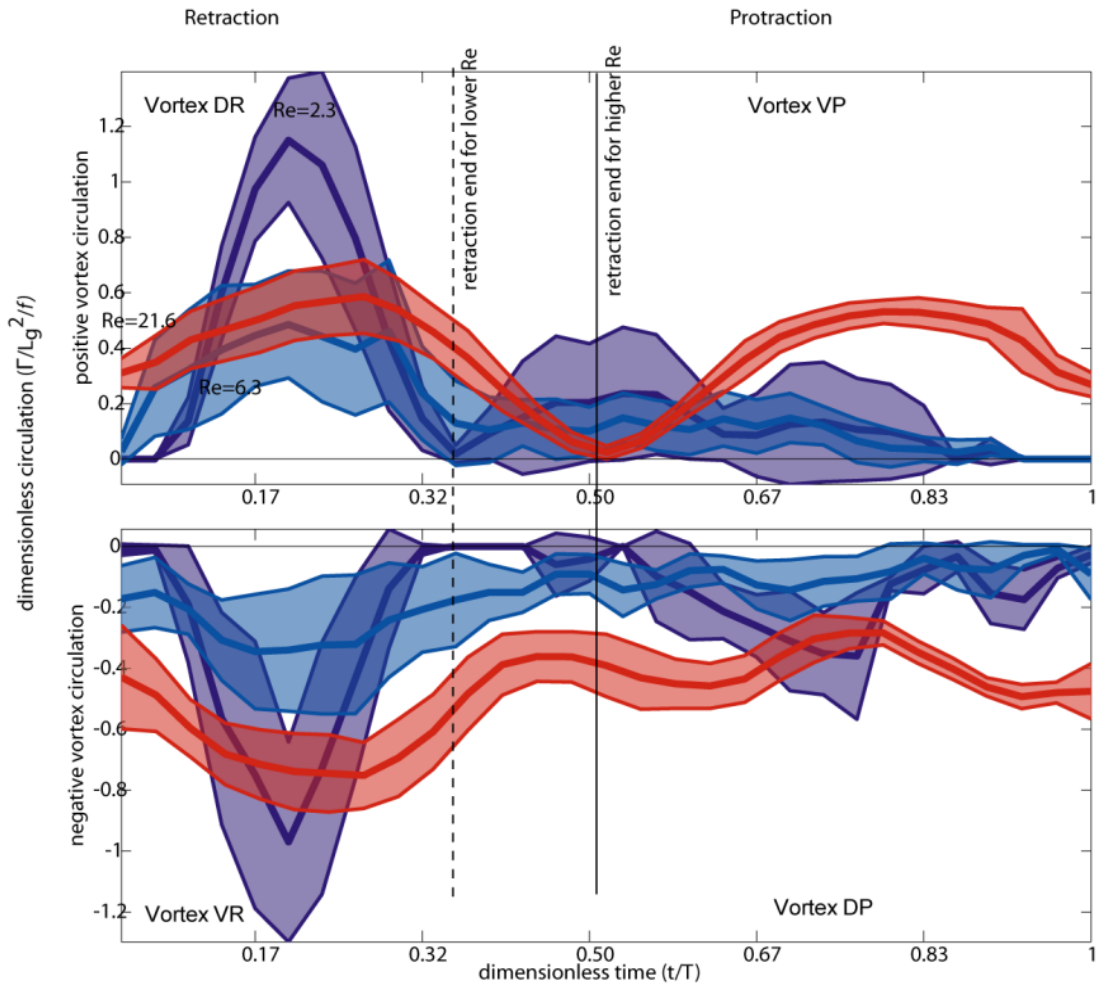


Figure 18. A-B. Vertical plane circulation history of positive and negative vortices at 3 representative Re_f . Time is plotted as fraction of period T . Retraction occurs rapidly over about 0-0.35 t/T in the smaller nymphs, but over 0-0.5 t/T in the large nymphs. The retraction and protraction phases are thus approximately equal length in the largest nymphs. A normalized and unitless value of circulation ($\Gamma/(L_g^2/f)$), where Γ is circulation of the vortex, L_g is gill length, and f is plate oscillation frequency is plotted for comparison of different size nymphs generating 10 fold range in maximum absolute circulation (0.3-3 mm^2/s). Curves denote the mean \pm 1 St.D of gills 2,3,4,5 ($n=4$).

3.C.3 Gill circulation history

As animals grew larger (and Re_f increased) the circulation ratio of the protraction:retraction (recovery:power) stroke decreased. This trend was statistically significant for the dorsal vortex ($r^2=0.71$, $F_{1,10}=26$, $p<0.001$) but not for the ventral vortex ($r^2=0.20$, $F_{1,10}=2.5$, $p=0.14$)(Figure 19 A). However, full symmetry was never achieved, even at the largest instars. Asymmetry in the strength of the vortices at

dorsal edge may be related to the action of the hinge, while at the ventral edge to the different boundary conditions supplied by the body walls and neighboring plates. For example, circulation of the vortex generated at the ventral edge of the gill during retraction (VR $t/T=0.17$) (Figure 19 A) was still about 30% higher at the higher Re than that generated at the ventral edge by protraction (VP $t/T=0.86$), giving a p:r ratio of 0.7 (Re 21.6).

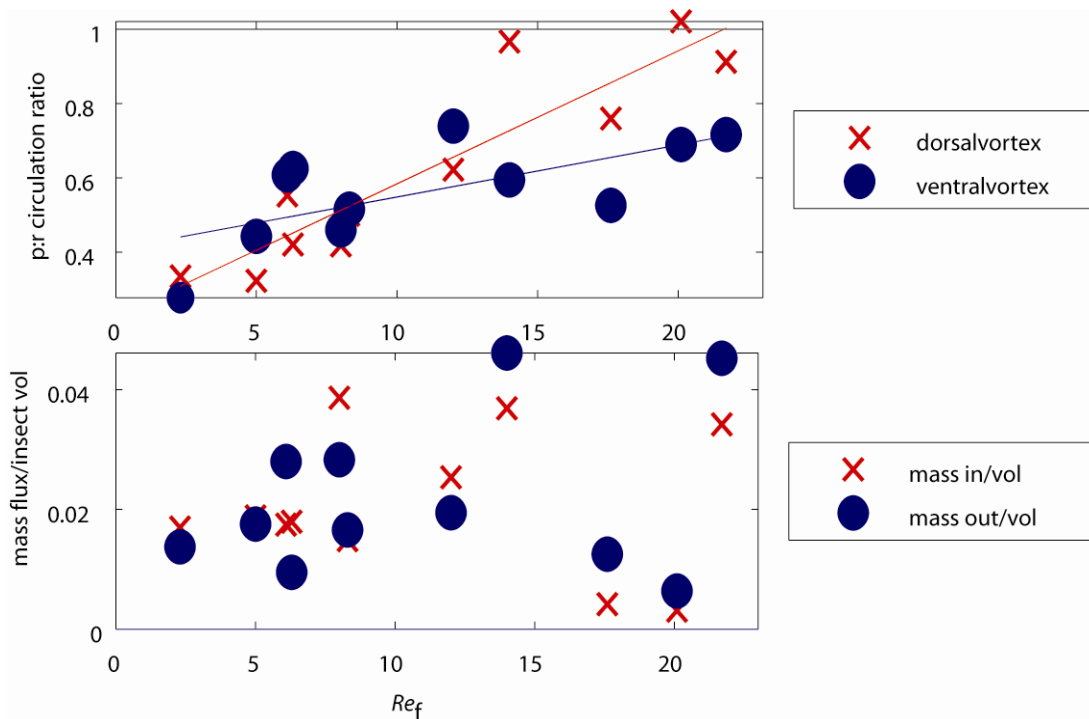


Figure 19.

A. Dorsal and ventral vortex p:r circulation ratio as function of Re_f . The p:r ratio is the maximum circulation achieved by the vortex at the designated location over protraction divided by the maximum achieved over retraction. Rowing mechanics of the small nymphs are indicated by the lower p:r ratio. B. Flux magnitude as function of Re_f . The influx is defined as the sum of all incoming vectors on the control box drawn in Figure 17-18. The outflux is defined as the sum of all outflowing vectors of the control box. Flux is standardized by the insect volume, showing that flow per volume can vary approximately 5 fold over ontogeny, but is not dependent on ontogenetic stage.

The dorsal: ventral (d:v) ratio index of vortex symmetry within a halfstroke indicated differences in condition across the plate during a single stroke, as opposed to between stroke differences quantified by the p:r circulation ratio. In the situation of

a stiff plate in small animals, the dorsal edge of the plate moves farther and faster during the powerstroke (Vortex DR during time $t/T=0-0.35$), and hence generated greater peak circulation than the ventral edge (Vortex VR during time $t/T=0-0.35$)(Figure 18). This situation did not hold for the $Re_f > 20$ flexible plate case which instead generated higher circulation at the ventral edge, despite lower amplitude of kinematics at that location (Figure 18). This shift in fluid dynamic response across ontogeny may be related to the increasing flexion of the distal plate, which functions to reduce the circulation of the fluid about the distal plate during both retraction and protraction.

3.C.4 Inter-gill sectional flux

Particularly in the high Re cases, maximal relative plate separation rate and flow rate were achieved when a posterior plate was initiating retraction and an anterior plate was ending protraction, so that these adjacent plates had opposing translational motions for a small fraction of the stroke period. For gill 4-5 space, this occurred at about $t/T=0.86$, producing high flow at ventral aperture v (Figure 20 C). For high Re_f , A suction phase ($t/T=0.86$, gill 4-5 space), in which fluid was drawn upward from the substrate, potentially occurred as two adjacent plates separated, although we can only infer the pressure field from the current data. Flow through the gill interspaces at the dorsal, mid, and ventral apertures was dorsally directed at almost each instant of the stroke cycle for the higher Re_f cases (Figure 13 A-C, $Re_f = 22$), again indicating the higher Re_f maintenance of flow direction over much of the stroke.

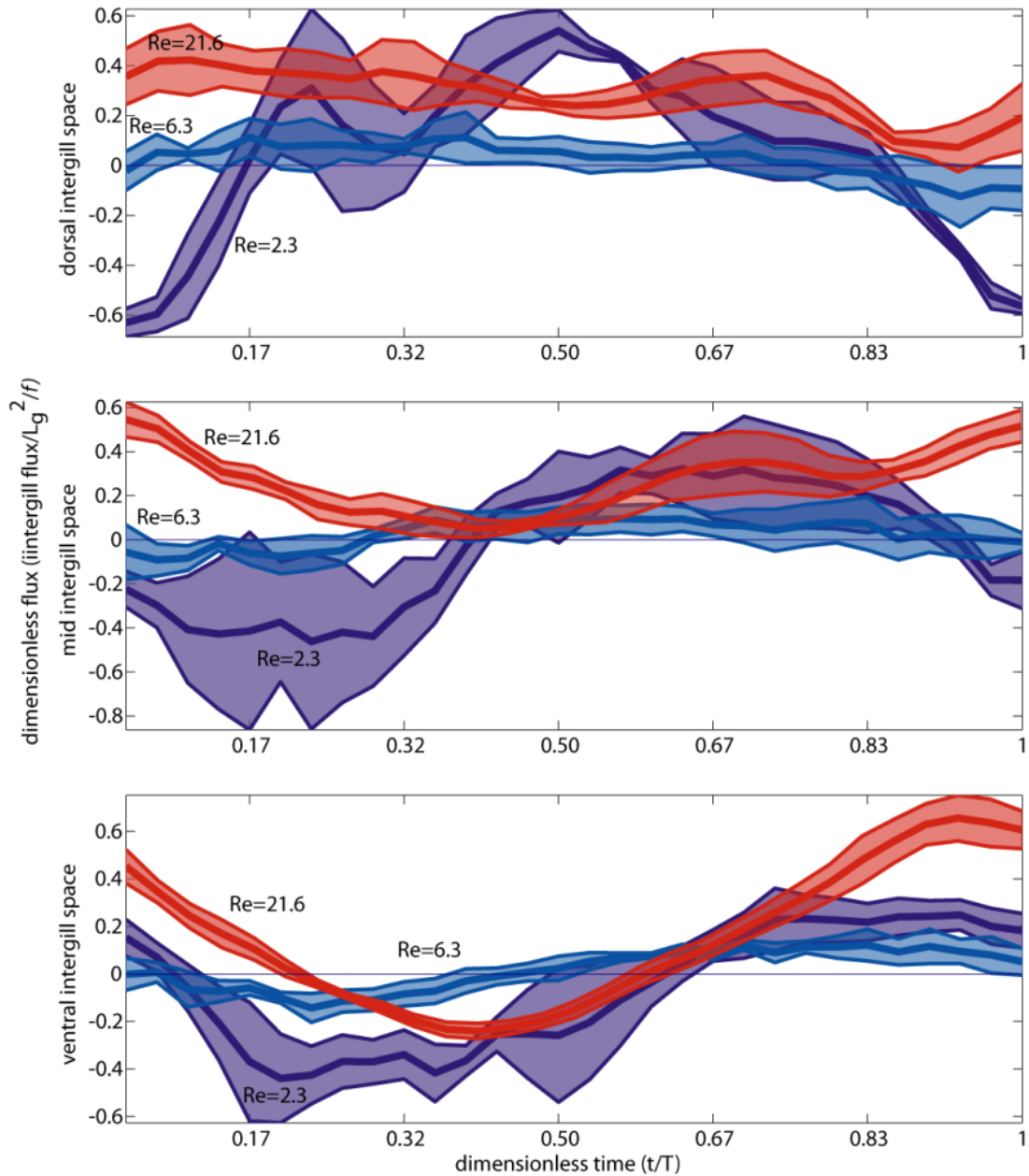


Figure 20. A-C. Vertical plane intergill flux history at 3 representative Re_f and through dorsal, mid, and ventral apertures. Period was normalized to 30 ms for comparison. 1-15 ms is approximately retraction, 15-30 ms is protraction. A normalized and unitless value of flux ($\text{flux}/(L_g^2/f)$, where flux is the flux through the gill interspace, L_g is gill length, and f is plate oscillation frequency) is plotted for comparison of different size nymphs generating 14 fold range in maximum absolute intergill flux ($0.45\text{-}6.2\text{ mm}^2/\text{s}$). The lower normalized intergill flux for the intermediate Re_f case ($Re=6.3$) may correlate with higher horizontal flow rates at this stage. Curves denote the mean \pm 1 St.D of gill interspaces 2,3,4,5 ($n=4$).

For $Re_f < 3$, those phases of the stroke with downward flow (Figure 20 A, dorsal aperture d, time $t/T=0.80-0.16$) (Figure 20 B, mid aperture m, time 27-12 ms) (Figure 20 C, ventral aperture v, time $t/T=0.1-0.66$) through gill apertures (dorsal d, mid m, ventral v) (Figure 14) were characterized by greater peak flows and flows over longer time periods than those phases with upward flow. These patterns resulted in net ventral flow over the stroke cycle. Flow rates within each gill space were strongly correlated with kinematics of neighboring plates. For example, for $Re_f < 3$, from time $t/T=0.83-1$ (Figure 20 A) the downward flow across the dorsal space was generated by retraction of the posterior gill, as the reference gill was itself undergoing minimal translation at that time. By mid retraction ($t/T=0.25$) however, the reference gill, in reducing the intergill space by retracting, was likely responsible for the upward (+) flow out of this space (Figure 20 A time $t/T=0.17-0.33$).

Not surprisingly, the flux through the gill spaces increased with increasing animal size and Re_f , potentially matching the absolutely larger oxygen demands of larger animals. However total flux in the vertical plane summed across the gills, multiplied by gill length to account for thickness of the slice, and then normalized by body volume did not increase with Re_f , varying between 0.005 and .045 $\text{mm}^3/\text{s}/\text{vol}$ (Figure 19 B). It should be recognized, however, that this is a rough estimate of the actual flow rate, since it does not incorporate potentially important contributions by the horizontal flow rate, which appears to be quite important in the smaller nymphs (Table 2). Our limited horizontal flow rate data suggest that vertical and horizontal flux is similar in magnitude in the smallest nymphs (vertical to horizontal flux ratio ~ 1), but that vertical flow is 2-3 fold that of horizontal flux in the largest nymphs.

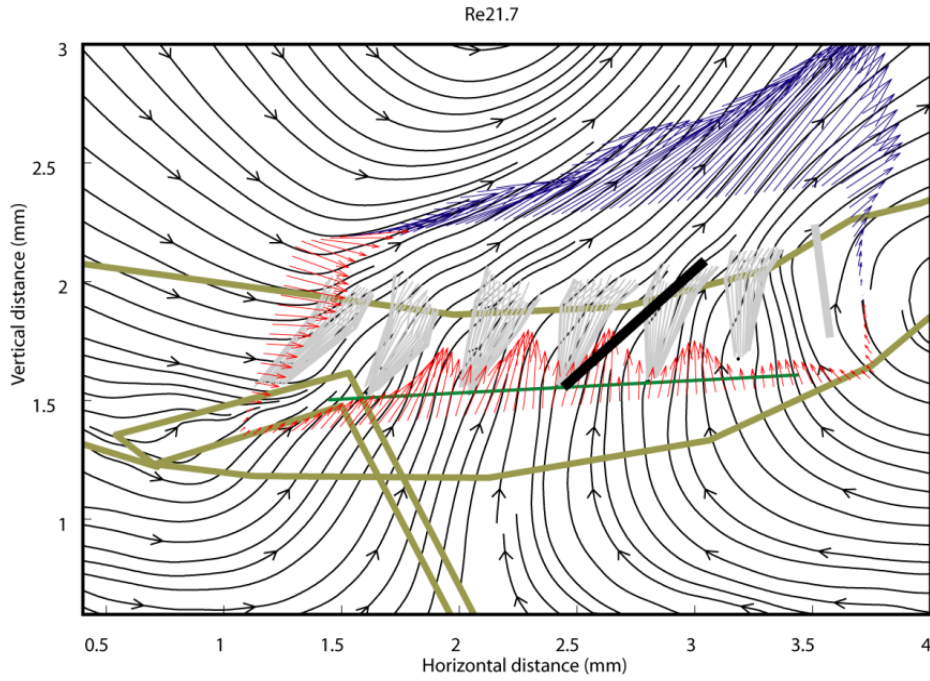


Figure 21. The time-averaged array flux through control volume at $Re_f=21.6$. Blue vectors at control volume edge indicate outflow, while red vectors at the control volume edge indicate inflow. The stroke plane of gill plates 2-6 is indicated by the green line, with the mean flow vector over control volume as the thick black vector. The mean flow angle is the angle between the mean flow vector and the mean stroke plane.

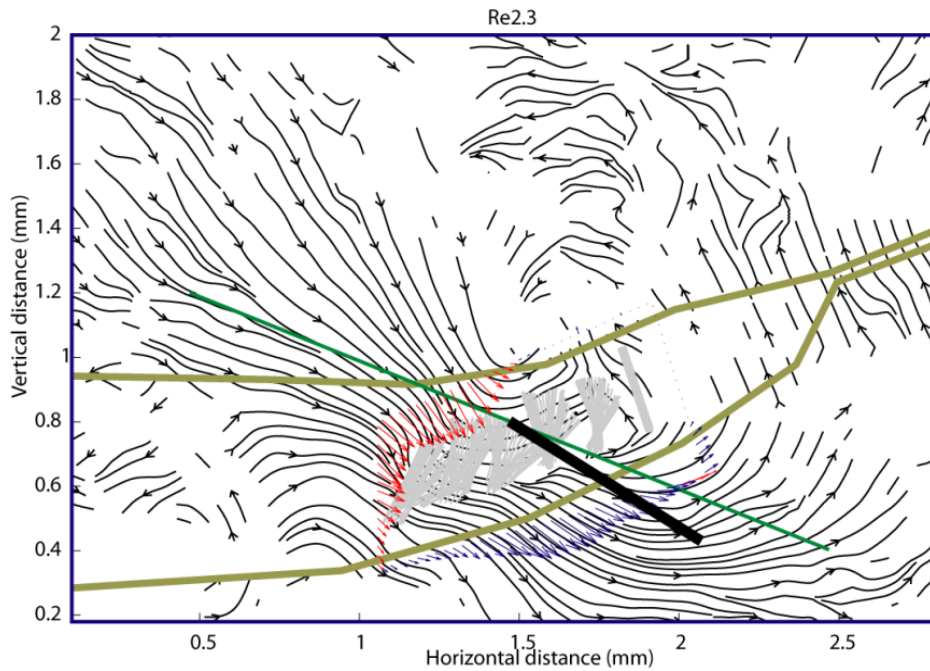


Figure 22. The time-averaged array flux through control volume at $Re_f=2.3$. Blue vectors at control volume edge indicate outflow, while red vectors at the control volume edge indicate inflow. The stroke plane of gill plates 2-6 is indicated by the green line, with the mean flow vector over control volume as the thick black vector. The mean flow angle is the angle between the mean flow vector and the mean stroke plane.

3.D. Discussion

3.D.1 Phased vortex pump

The crux of the questions posed in the introduction is to ascertain how an organism with a similar set of appendages can function hydrodynamically across the intermediate range of Re_f . The gross kinematic and mean flow observations of *C. triangulifer* demonstrated that there exists a transition from a rowing to a flapping mode around an $Re_f \sim 5-10$. Our question can now be distilled to: “Are completely different hydrodynamic mechanisms at work at either end of the spectrum, or does this shift represent an adaptation of a single mechanism to these two extremes?”

Observations of the detailed unsteady near-gill flow field presented above indicate the latter, with the basic components of the mechanism being the generation of a vortex ring around the periphery of the gill plate upon protraction and retraction. The difference between the two extremes, then, is how the vorticity is distributed due to the combined effects of viscous diffusion and the spatio-temporal manipulation of the vortex ring by the kinematics of the gill plate itself.

Insight into the first of these two effects, viscous diffusion of the vorticity produced by the moving appendage, can be obtained by examining the maximum vortex diameter during retraction as a function of Re_f (Figure 6). This result shows the initially remarkable result of a nearly constant vortex size ($r^2 = 0.01$, $p = 0.73$) as a function of Reynolds number. The reason for this becomes clear when one further examines the frequency of oscillation of the animals as a function of Re_f , which

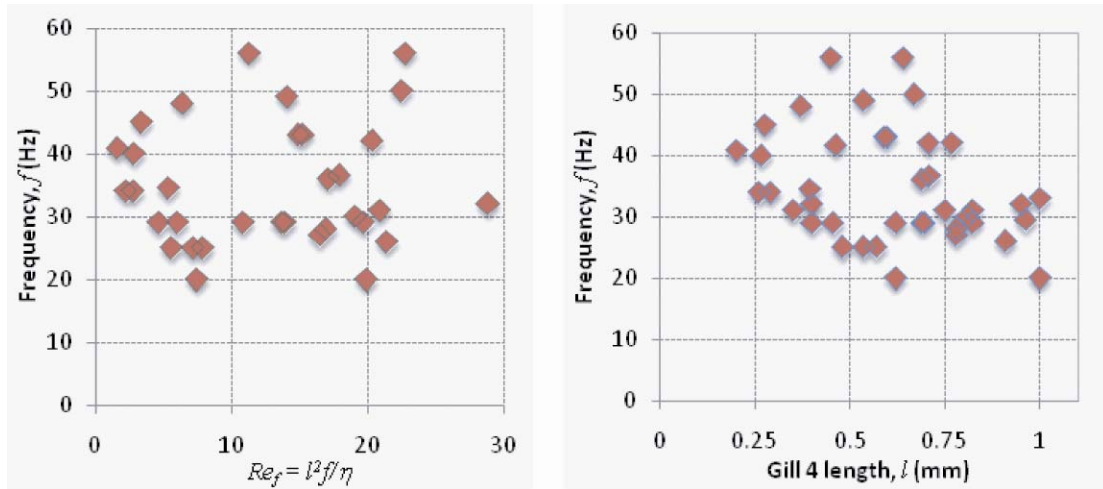


Figure 23. Gill plate oscillation frequency as a function of Reynolds number (left) and gill 4 length (right). Each point represents an individual animal. The data-set represents an approximately equal sampling of wild and lab reared nymphs.

shows a similar statistical independence (Figure 23). Thus, as the animal produces vorticity on the surface of the gill plate due to the plate accelerations and the surrounding pressure fields, viscous diffusion is acting to spread the vorticity further into the flow. The time available for this to occur will limit the extent to which the vortex can grow, which is to first order determined by the oscillation frequency of the appendage. Since the oscillation frequency appears to be invariant with respect to Re_f (on average), then it should come as no surprise that the dimensional vortex size is similarly constant. It should also be noted that in the above discussion that in the low Re_f cases, the vortex size during retraction represents a conservative size estimate since the retraction duration is shorter than the protraction, and hence is the smaller of the two vortices. The important conclusion from this observation is then that the *relative* vortex size in comparison to the appendages is decreasing over ontogeny.

The second of these points, namely the manipulation of the vorticity by the kinematics of the plate, is much more difficult to quantify and describe, as the

important details that need to be observed are transient and spatially complex. The most effective means to view these dynamic features is through an x - y - t diagram that displays the spatial evolution of the identified vortices through space and time in conjunction with the motion of the gill plates. Two such figures are shown for the example extreme cases of $Re_f = 21.6$ and 1.8 , respectively, in Figures 24 and 25. These figures were prepared by appending individual frames of the two-dimensional vorticity field together (obtained from the vertical x - z plane) to form a three-dimensional array, the third component of which now represents the phase of the oscillation cycle. Isosurfaces equal to 20% of the global maximum through the cycle of the positive (red) and negative (blue) vorticity were then extracted from the volume, and “endcaps” of the resulting vortex “tubes” were colored according to the vorticity values locally on the x - z plane corresponding to that given instant in the cycle. To better visualize the dynamics throughout the cycle, these figures were also sectioned at different times, as shown in the subfigure below the main figure. Note that the static gill 7 is not shown in the figure, and that the non-dimensional cycle time of $t/T = 0$ was arbitrarily set to the condition of when gill 4 (shown in red) initiated its retraction from the fully protracted state.

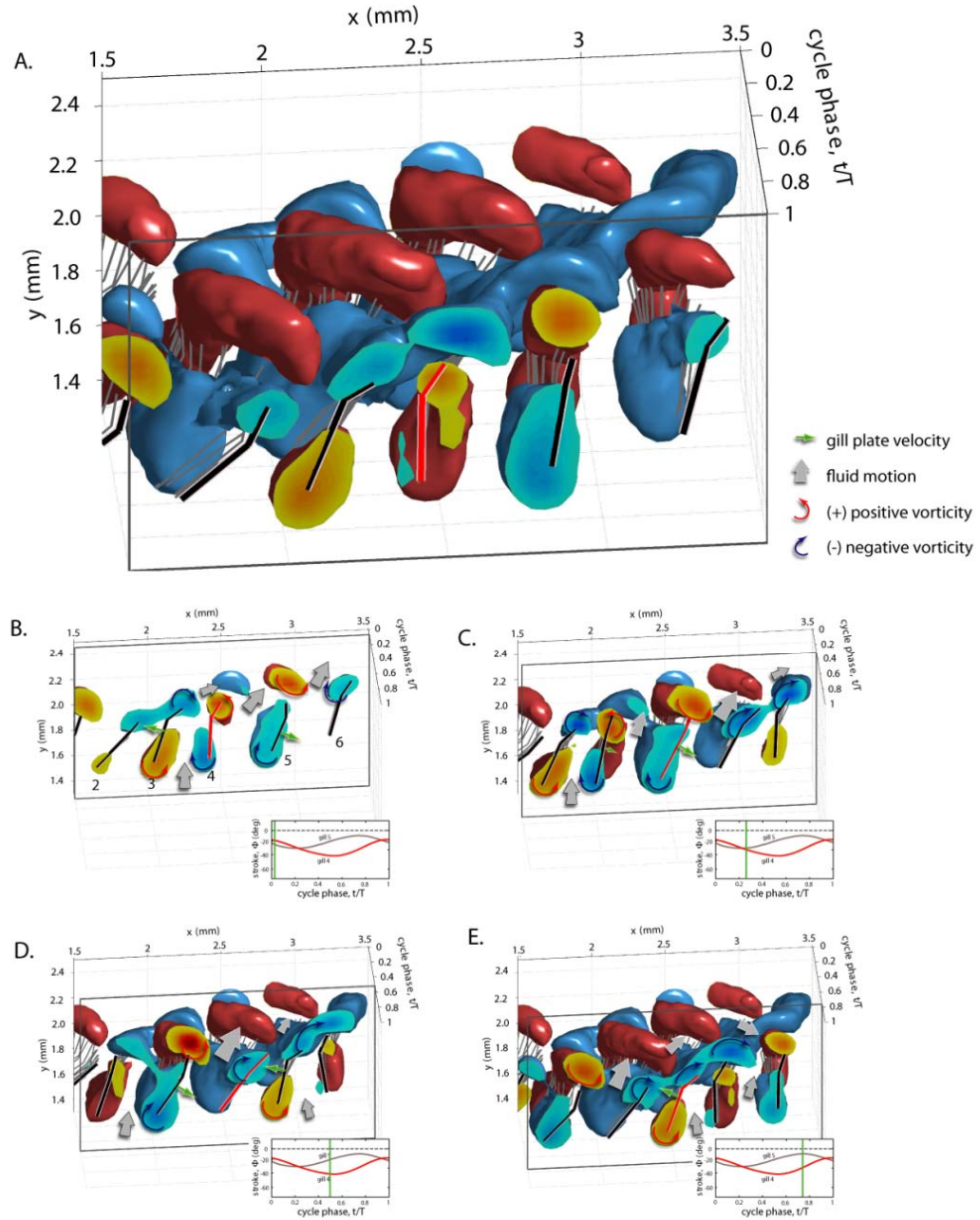


Figure 24. Isosurface of positive (red) and negative (blue) vorticity as a function of x - z - t for $Re_f = 21.6$. Surface value corresponds to $|\omega_y| = 0.2(\omega_y)_{\max}$. Gills are shown at each instant in the cycle as a gray line, with black (red for gill 4) used for the last slice in the section. The “endcap” of the surface shows the vorticity magnitude at the given instant in the cycle. A. complete section ending at $t/T = 1$; B. slice depicting $t/T = 0.07$; C. slice depicting $t/T = 0.31$; D. slice depicting $t/T = 0.52$; E. slice depicting $t/T = 0.75$. The inset shows the stroke position of gill 4 and 5, with a green bar indicating the phase of the cycle.

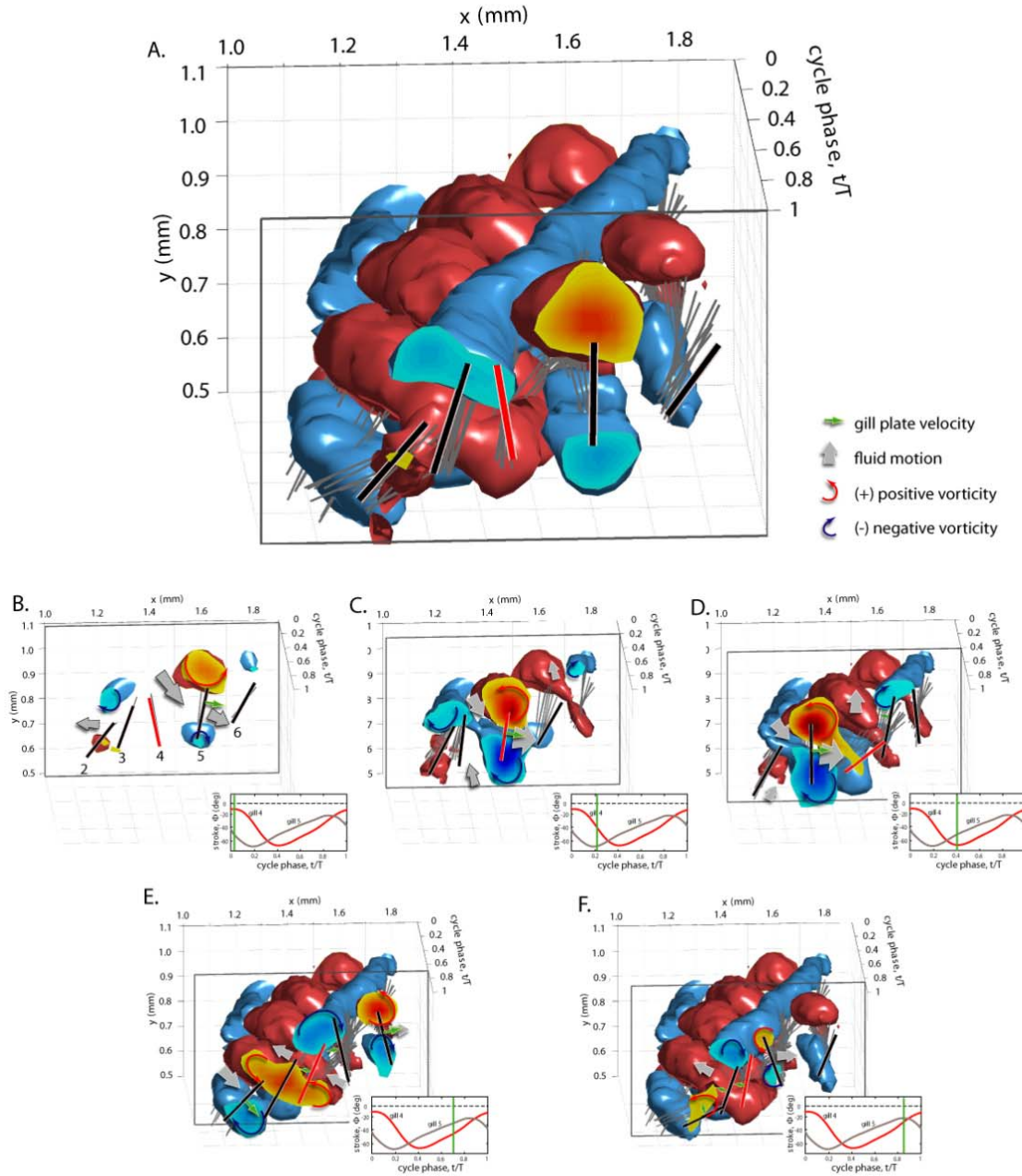


Figure 25. Isosurface of positive (red) and negative (blue) vorticity as a function of x - z - t for $Re_f = 1.8$. Surface value corresponds to $|\omega_y| = 0.2(\omega_y)_{\max}$. Gills are shown at each instant in the cycle as a gray line, with black (red for gill 4) used for the last slice in the section. The “endcap” of the surface shows the vorticity magnitude at the given instant in the cycle. A. Complete section ending at $t/T = 1$; B. slice depicting $t/T = 0.04$; C. slice depicting $t/T = 0.2$; D. slice depicting $t/T = 0.4$; E. slice depicting $t/T = 0.69$; E. slice depicting $t/T = 0.86$. The inset shows the stroke position of gill 4 and 5, with a green bar indicating the phase of the cycle.

Starting with the high Reynolds number condition, $Re_f = 21.6$ (Figure 24A), one can immediately appreciate the regularity and synchrony of the gill elements within the array, and a clear herringbone pattern of alternating positive and negative vorticity is woven across the top of the array. More specifically, the generation of the positive vorticity (DR+) corresponds to the retraction phase of the gill, while the negative vorticity (DP-) corresponds to the gill protraction, as identified earlier. Examining the positioning of this vorticity and the resulting flow at different points of the cycle provides an explanation of how the net mean flow is generated (Figure 24B-E). Starting just after gill 4 retraction (Figure 24B), a vortex ring corresponding to the retraction phase has just formed on gill 4. Gill 3 is nearing its peak protraction velocity, creating a widening gap, and a vortex ring with opposite sign already well formed as a result. The proximity of the opposite sign vorticity between the ventral regions of gill 3 and 4 forms a dipole with an induced velocity directed towards the widening gap, aiding the filling of the intergill region of gill 3. Note that all of these vortices tend to exhibit distortions in their shape due to the local convection and diffusion of the vorticity as it is being generated; the ventral vortices are elongated along the surface of the gill due to the inflow from the ventral region, while the dorsal vortices are often elongated along the arc of the gill tip.

Simultaneous to the initiation of gill 4 retraction, gill 5 has just past its peak retraction velocity, and has a well formed DR+ and VR- vortex attached near and over its surface. The groupings DR5+/DP6- as well as DR4+/VR5- also form dipole pairs that induce flow in the dorsal-posterior direction. For the DR5+/DP6- vortex dipole, this induced flow is the ejection of fluid away from the dorsal aperture of the intergill space. For the DR4+/VR5- vortex dipole, this induced flow is the infilling of

fluid into the intergill space through the ventral aperture. The phasing of the gill movements to produce these particular pairings is a common theme that is key to the generation of the dorsally directed flow observed in the time-averaged velocity field. This theme is repeated at the quarter-cycle point (Figure 24C, by DR3+/VR4- and more strongly by DR4+/DP5-), and again at the half-cycle (Figure 24D, by DR3+/DP4-) and three-quarter cycle (Figure 24E, DR2+/DP3-) points as the dorsal tips approach each other in neighboring gills, moving in a retrograde wave toward the anterior of the array. The generation of a net mean current by a specific arrangement of vorticity produced by the phased stroke kinematics of a serial appendage array can be thought of as a “phased vortex array” pumping mechanism. As will be seen in the next case, this construct is useful for explaining the observed hydrodynamic operation for both the high and low Reynolds number conditions.

The low Reynolds number condition, $Re_f = 1.8$, is shown in Figure 25. At first glance, there are several strong similarities and noticeable differences in comparison to the high Reynolds number case. For similarities, the dorsal perspective reveals there are still patterns of positive vorticity (DR+) moving in the posterior direction resulting from gill retraction and a streak of negative vorticity (DP-) moving in the anterior direction from the protraction (Figure 25A). The difference, however, is that the size of the vortices are much larger relative to the gill size and spacing (as noted above), and much of the finer features of the vortex topology (such as the zig-zag kinks in the DP- vortex chain, Figure 25A) are lost due to the larger relative influence of diffusion. Aside from these general differences, the arrangement of the vorticity as a result of the stroke kinematics is also significantly altered. The most prominent difference is phasing of the gills to produce a distinct and isolated “power” stroke

during the retraction phase of each gill. This is clearly visible in gills 5, 4, and 3 in the inset Figures 25B- D, each of which has been captured close to the peak retraction velocity of the respective gill. This relatively isolated “power” stroke in conjunction with the comparative larger vortex size has the effect of making the dominant vortex interaction taking place with the dipole pair of the ring itself (DR5+/VR5-, DR4+/VR4-, DR3+/VR3-), rather than with adjacent vortex structures produced by other gills. As a result, the predominant flow produced by this stroke corresponds to a flow through the center of the ring and in the direction of motion of the gill (ventral-posterior). The other difference that can be observed is that the increased stroke range combined with the increased variation in pitch carries the positive dorsal retraction vortex (DR+) toward the ventral edge of the neighboring posterior gill, which soon starts its protraction (VP+), creating a continuation of the vortex (see, for example, DR5+ to VP6+ in Figure 25C; DR4+ to VP5+ in Figure 25D; DR3+ to VP4+ in Figure 25E). The combination of the VP+ vortex with the formation of a much stronger negative dorsal vortex (DP-) on the same gill leads to a minor retrograde flow, i.e. anterior directed flow opposite to the full stroke cycle averaged mean flow at that location. Finally, the last major difference is the coordinated protraction of multiple gills, as best exemplified by gills 3, 4 and 5 (Figure 25E-F). Their combined motion diminishes the amount of circulation produced per gill, reducing the magnitude of the retrograde flow, as evidenced by the circulation protraction:retraction ratio (Figure 19 A) and comparison of the intergill flux exiting the intergill volume during these two events(Figure 20 A,B,C time $t/T \sim 0.4-1$). The inter-gill flux can also provide an additional means to relate the stroke and flow kinematics to simpler models of rowing or flapping. In particular, the interaction of

gill plates may produce peak pumping fluxes at phases other than predicted by simplistic models.

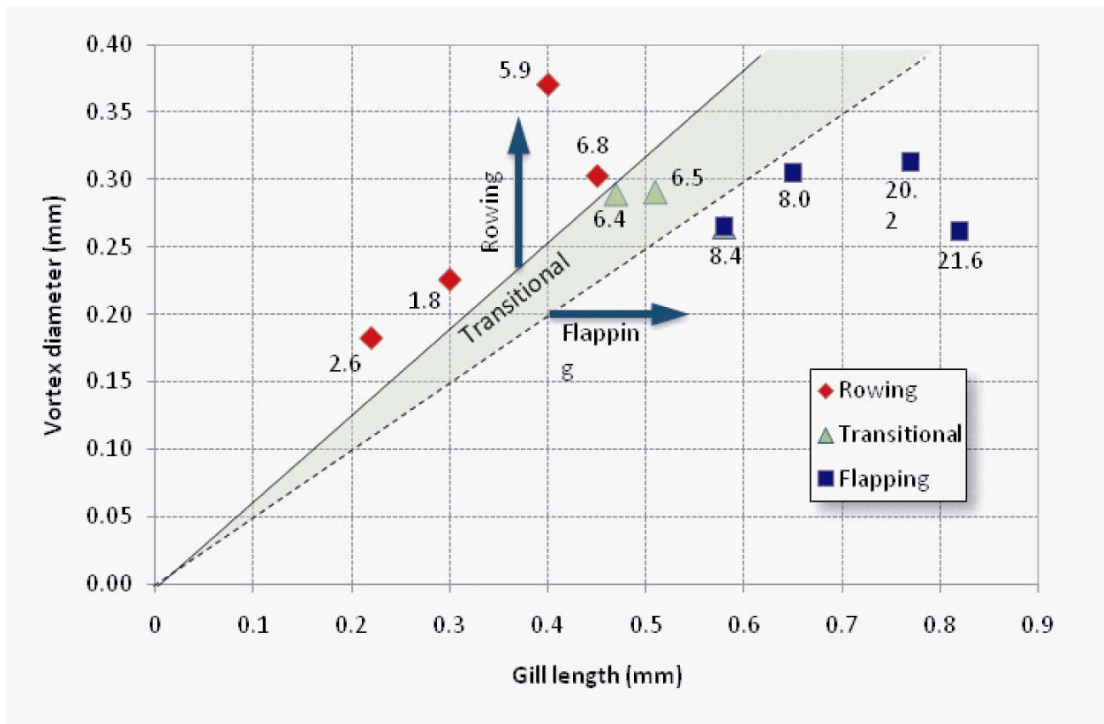


Figure 27. Relationship between vortex diameter and gill length, illustrating observed cases of rowing, transitional and flapping behavior. The oscillating Reynolds number, Re_f , for each case is shown below the label.

The above discussion illustrates how subtle differences in the topology of a relatively similar vortex structure can lead to dramatically different mean flow patterns. Although not immediately quantitative, the idea of the phased array vortex pump does offer some logical explanations for the transition behavior. Specifically, observation of the timing and positioning of the vortices was key to producing the net dorsal flow at the high Reynolds number cases, and examination of the low Reynolds number cases make plausible the idea that the relatively larger vortices under these conditions would interfere with the operation of producing the identical flow, or at

least may result in a much weaker flow (due to cancellation of opposite-signed vorticity from cross diffusion). This idea can be tested by examining the calculated maximum vortex diameter during retraction as a function of gill length, and observing how it correlates with the rowing to flapping transition (Figure 26). The data indicate that *C. triangulifer* exhibits a consistent flapping behavior when the maximum vortex diameter is less than one half the gill length. This also happens to correspond to an oscillating Reynolds number typically on the order of 6 to 8, though it is not necessary that the above condition give a strict boundary in terms of the Reynolds number. Below this transition size, the previous discussion would indicate that it is favorable for the phase vortex array pump to reconfigure its topology for continued pumping performance. Following these ideas a bit further, it seems unlikely that such a pumping mechanism can extend down to arbitrarily small Reynolds numbers, even with continued alterations to the stroke mechanics, as eventually diffusion would generate vortices on the scale of the array or larger, removing its capability to significantly manipulate the topology in any meaningful way. The array should be capable of accomplishing net displacement down to infinitely small Re , however, through its time irreversible components of motion. Though an idealized situation, such an array might be predicted to behave akin to a single appendage, as it deals with single vortices. Metachronal phasing of rowing strokes in feeding and locomotory arrays (Jiang et al., 2002; van Duren and Videler, 2003; Malkiel et al., 2003) are quite ubiquitous, and as suggested by the current study, the appendage generated vortices of such arrays might encompass multiple appendages. In such a condition, function is enhanced by individual appendages contributing to the array generated retraction and protraction flow structures.

3.D.2 Potential shift in component dynamic mechanisms over ontogeny

The function of the phased vortex pump can be compared to commonly cited fluid dynamic models. Among these, rowing and squeezing are foremost in their similarity to the array fluid kinematics, where squeezing is typically defined as pressure driven flow, and occurs in regions of changing volume. Part of the explanation for the success of nymphs in using a basic appendage array throughout the intermediate Re may lie in the capability for differential reliance on these two mechanisms with what could be perceived as relatively slight changes in plate kinematics.

The smallest nymphs most clearly relied on rowing, as evidenced by individual plate kinematics (VSR) (Figure 10), the array metachronal pattern (Figure 26), and vorticity evolution (Figure 18). Notably, however, the powerstroke phase of such a rowing mechanism was evident in the fluid kinematics at all nymph sizes, in the form of the p:r ratio (Figure 19 A) and overlap of vortices during the recovery halfstroke. This indicated enhancement of drag during the retraction “power” stroke, but reduced drag by coordinated recovery stroke of adjacent gills. The hinge of the large nymphs could even be described as enabling the overlapping of vortices during the recovery stroke, as otherwise vortex diffusion would not have been sufficient to extend across the gill plate dorsal gaps.

The high kinematic stroke symmetry of the proximal plate of the large nymphs was reflected in the higher symmetry of generated vorticity (Figure 18). In the largest nymphs, the kinematics of the proximal plate alone could not be separated into a

“power” and “recovery” stroke. Hence the rowing mechanism was replaced by a new mechanism as the upward flow developed in response to the potentially oscillating pressure gradient at the ventral side of the gill plates. While speculative, transverse flow may become possible as this pressure effect approached that of the viscous rowing effect over ontogenetic size increase.

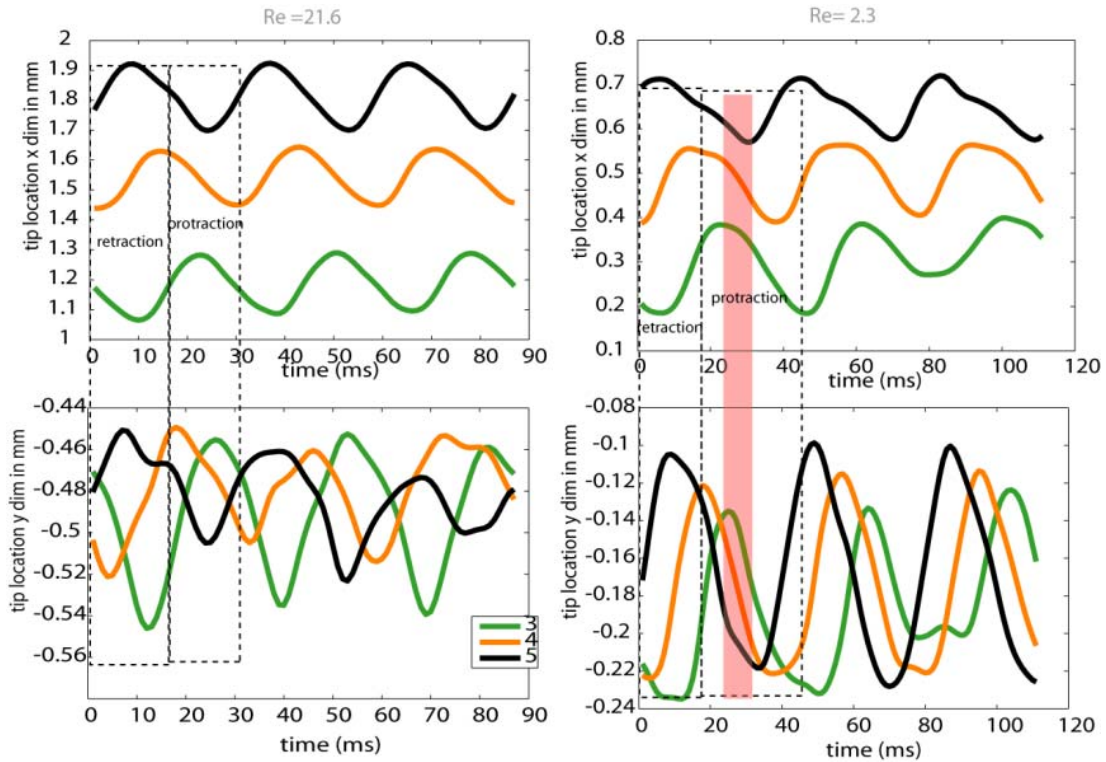


Figure 26. Rowing kinematics derived from metachronal phasing of adjacent gill plates. Results from 3D kinematics demonstrate the concerted rowing due to the combination of high retraction speeds and metachronal phase lag at low Re ($Re=2.3$) (right column), but absence or less evidence of this feature at higher Re (left column). Top plots are the x location (dorsal-ventral axis) of the gill tip motion. Bottom plots are the y location (anterior-posterior axis) of the gill tip motion. Retraction and protraction phase for the center gill (gill 4) of these three gills (gill 3,4,5) is marked for the first of three oscillation periods. Only during mid-protraction of the reference gill (gill 4) at low Re can more than 2 adjacent gills be identified as moving together in a common direction (this phase is shaded pink). It is at this phase that shared vorticity is also prominent across these multiple gills.

Such transverse flow may result from positive or negative pressure induced by the changing intergill volume. Notably, such flow is absent anterior to gill 1, a location in the flow bordered on only one side by a moving plate. The flow is also minimal in the gill 6 space, which is bordered by mobile gill 6 on one side and

stationary gill 7 on the other. Both these observations suggest the importance of oscillating gill pairs to produce the upward flux, and thus a pressure based system. The flow field of small and large instars may both use such a squeeze mechanism, but orient it differently due to different kinematics and morphology. For the small nymphs, such an effect (reverse squeeze) occurred as gill 5 rapidly retracted, fluid was drawn from the dorsal side into the widening space of gill 4 at time $t/T \sim 0$ (Figure 14 jet V), while for large nymphs it may be a prominent feature at the ventral side of the array and involve upward flow. Rapidly separating plates then produce flow directed ventrally in the smallest instars, but dorsally in the largest. Rapid separation of plates to produce low pressure regions that draw in fluid is somewhat analogous to the fling mechanism of insect flight (Lighthill, 1973). Essentially, a V shaped configuration of the separating wing plan surfaces draws fluid into the increasing inter-wing space. Primarily the usefulness of this mechanism is attributed to its generation of starting vortices, which serve to rapidly generate the LEV of each wing. There is much interest in the impact of intermediate Re on the performance of the clap-fling mechanism (Miller and Peskin, 2005; Miller and Peskin, 2004), and hence the gill array phased vortex pump may be of particular interest in this regard as a system that spatially reorients this mechanism over ontogeny.

A reciprocating stroke pattern generates a wake, with wake shedding distance approaching 0 with decreasing Re . In certain circumstances energy can be extracted from these shed fluid structures. For example, at stroke reversal, an insect wing sheds the vorticity generated during the prior stroke, and, as it reverses direction, the wing passes through this shed vorticity field. This vorticity can influence force at the start of the stroke, a mechanism termed 'wake capture' (Dickinson et al., 1999). The

shared vorticity of the protraction stroke in the phased vortex pump can be analogized to a continual, intensive half-stroke ‘wake capture’ effect, although here we only infer the dynamic benefit of such an interaction. Kinematic phasing produces an arrangement of vorticity that is likely precisely timed to localize effect and produce the appropriate degree of transverse flow. Certain aspects of the fluid kinematic phasing of the phased vortex pump may apply to the many appendage arrays that stagger the activation sequence of adjacent appendages by about 1/5 of a stroke cycle (Kohlhage and Yager, 1994; van Duren and Videler, 2003; Knudsen, 1973). As such, it is a general model that may describe, in some sense, an optimal pattern with which to develop and coordinate fluid structures at intermediate *Re*.

3.D.3 Implications of specialization for ventilation

While most well-characterized aquatic appendage are jointed, leg-like structures, those appendages specialized for ventilation have high surface area associated with oxygen diffusion enhancement, eg.gills of Branchiopod and Isopod(David, 1991) crustaceans, Xiphosura(Knudsen, 1973), Ephemeroptera (Wingfield, 1939). Because of the surface area enhancement, the appendage performs an important diffusion role that can function independently of muscular activation of the appendage, with the density of plates packed into a given space potentially increasing the diffusion rate at a given far-field concentration. Unlike a propulsive system for aquatic escapes or wings in flight, where a specified minimum impulse is needed to accelerate the animal mass, any ventilation flow, no matter how small, can assist diffusion. General metabolic rate scaling combined with passive diffusion

limits is likely a fundamental factor in nymphs initiating active ventilation once achieving body length of about 2 mm.

The ventilatory flow of *Centroptilum* nymphs was only generated by stationary nymphs, in a different direction than that generated by swimming, and by appendage mobility used, as far as is known, solely for ventilatory flow. These factors together produce a novel model system for bio-mimetic analysis. The ontogenetic trajectory of this ventilation system is instructive of diffusion physics. The smallest nymphs had no gill plates, implying that passive diffusion or whole animal locomotion, i.e. walking or swimming, to fresh fluid regions was sufficient to meet oxygen demand. Nymphs with very small gill plates oscillate them rarely, if at all. At this size, however, even passive plates could be beneficial in boosting diffusion. All nymphs with larger gills periodically activated the array, probably because bulk flow was now vital to meet metabolic demand.

The function of the flow is intricately related to its form (Denissenko et al., 2007). Flows generating locomotive force must result in net fluid displacement over an oscillation cycle, while ventilatory or filterfeeding flows must mix the fluid or otherwise increase the rate of contact of the animal with oxygenated water or nutrient particles. Ventilation flow structure need not resemble locomotion powering or foraging flows due to the completely different functional requirements of these flows. Diffusion enhancing flows may represent a subset of biological flows inherently characterized by a lower Reynolds number. The diffusive length scale defines the characteristic length for the Re , so that both are constrained to within several mm, resulting in typical $Re < 100$. In the intermediate Re regime, the importance of the delivery of chemical species by diffusion is rapidly replaced by the necessity of

delivering a chemical species by bulk flow of its solvent. Where turbulent separation is not available due to the low Re , artificial micro-mixing devices work by bending and folding of fluid lamina (Ali Asgar et al., 2007). Depending on the scale of the system and the relevant diffusion gradients, ventilation flows could be quite different than locomotion flows. Foraging and locomotion systems in other aquatic taxa are usually based on flow directed cephalic to caudal, likely due to the need for sensory processing of incoming stimuli. While the net flow in *Centroptilum triangulifer* does have a significant anterior to posterior component, a survey of other species of mayfly nymphs shows that flow can be posterior to anterior, such as in *Chloeon dipterum* (Eastham, 1932; Eastham, 1958) and even normal to the sagittal plane, in *Caenis horaria* (Eastham, 1934)

Chapter 4: Conclusion

Our analysis of ventilation in the developing mayfly revealed changes in gill kinematics and morphology with the combined effect of increasing temporal symmetry of gill stroke with increasing Re_f . This change occurred primarily through reductions in the range of pitch motion, the ratio of peak protraction/retraction speeds and stroke plane deviation over a narrow range of Re_f . This transition was accompanied by a change from posterior/ventral flow to dorsal/transverse flow at higher Re_f and a transition from an essentially rowing stroke to a flapping stroke. The simultaneous transition of these parameters in the range $3 < Re_f < 8$ suggests a change in hydrodynamic gait that may have broad significance for the many organisms that ventilate, swim or fly in the intermediate Re range, and particularly for those that utilize paired plate-like structures. Specifically, our results are roughly consistent with a model which predicts that changes in propulsive mechanisms should occur abruptly rather than gradually as an organism traverses the intermediate Re regime, but further study is needed to determine whether kinematic change actually reflects a switch in hydrodynamic mechanism with increasing Re .

The basic plan of an oscillatory array adapts to growth and its requisite change in Re to ensure that effective ventilation current is continually generated over the transition. The mayfly gill array involves ontogenetic growth of oscillating appendages through a viscous diffusive length comparable to appendage length. Such a vorticity diffusion distance may be a hydrodynamic feature of the system that places a lower limit on effective operation of the more symmetric flapping mechanism observed in the largest nymphs. The mechanism of pumping (phased-vortex array) is similar across the Re range, but its configuration is modified by the fact that the size

of the vortex elements is nearly the same for all animals due to the invariance of the frequency. In particular, the intergill flow cannot be a significant component of the pumping mechanism when vortex size encompasses more than a single appendage.

The intermediate Re regime is one in which diverse organisms not only locomote, but also forage, detect chemicals, and ventilate. All of these actions must be performed efficiently and within the constraints of the local Re . I suggest that morphological and kinematic adjustment to growth should be common within diverse organisms in the intermediate Re regime. Furthermore, adaptations in such systems should reflect some of the specific ontogenetic changes observed in the mayfly gill plate array.

This quantification of this biological model system can be used as a baseline for computational flow studies of flapping arrays. In particular, such studies can also enable testing of behavioral extremes not used by nymphs. Thus, such simulations could address questions of optimality of plate phase relationships, hinge and pitch range, and test for critical transitions without the complications of the changing gill morphology and kinematics. Re fluctuations due to seasonal variation in temperature and thus viscosity might also be encoded into the development mechanism, and I predict that future experimental work should find delays in the onset of the large nymph kinematic pattern in colder water.

List of symbols

ME medial edge of gill plate

LE lateral edge of gill plate

R root of gill plate, abdomen attachment point of gill plate

TS trachea sub-distal point of gill plate

MC midchord of gill plate

α plate pitch

β stroke plane inclination angle

γ hinge angle

ε stroke plane lateral offset angle

θ stroke plane deviation angle

μ , dynamic viscosity

η kinematic viscosity = μ/ρ

ρ density

Φ stroke plane angle

Φ_{\max} stroke plane angle anterior limit

Φ_{\min} stroke plane angle posterior limit

f plate oscillation frequency

Re Reynolds number

Re_f frequency Reynolds number

L_a animal length not including caudal filaments

L_g gill total length

L_{rs} gill root separation distance

AR plate aspect ratio

SA plate surface area

\mathbf{n}_{prox} proximal plate unit normal vector

\mathbf{n}_{flap} distal plate unit normal vector

VSR volumetric stroke rate

\mathbf{v} velocity of midchord position

SP stroke plane

A_{prox} surface area of proximal plate

A_{flap} surface area of distal plate

A surface area of proximal plate

k advance ratio

L characteristic length of the appendage or moving body

U characteristic velocity

Wo Womersley number

R reference length

γ first moment of vorticity

$\dot{\omega}$ vorticity vector

$\dot{\mathbf{n}}$ unit normal vector for the surface of integration

dA scalar differential area of the surface

Δl scalar incremental length along the boundary edge

ΔQ local flux

τ fraction of a stroke period

T stroke period

DR dorsal retraction vortex

VR ventral retraction vortex

DP dorsal protraction vortex

VP ventral protraction vortex

MR medial retraction vortex

LR lateral retraction vortex

MP medial protraction vortex

MP medial protraction vortex

V ventrally directed jet

D dorsally directed jet

LEV leading edge vortex

Γ circulation

L_{is} intergill spacing

L_v vortex diameter

L_{vd} vortex diffusion distance

Bibliography

- ALEXANDER, R. M. 1989. Optimization and gaits in the locomotion of vertebrates. *Physiol. Rev.* 69:1199-1227.
- ALI ASGAR, S. B., T. K. P. ERIK, and P. IAN. 2007. A passive planar micromixer with obstructions for mixing at low Reynolds numbers. *Journal of Micromechanics and Microengineering*:1017.
- BARLOW, D., M. A. SLEIGH, and R. J. WHITE. 1993. Water Flows around the Comb Plates of the Ctenophore *Pleurobrachia* Plotted by Computer: A Model System for Studying Propulsion by Antiplectic Metachronism. *J Exp Biol.* 177:113-128.
- BAUMER, C., R. PIROW, and R. J. PAUL. 2000. Respiratory Adaptations to Running-Water Microhabitats in Mayfly Larvae *Epeorus sylvicola* and *Ecdyonurus torrentis*, Ephemeroptera. *Physiological and Biochemical Zoology.* 73:77-85.
- BENNETT, L. 1966. Insect Aerodynamics: Vertical Sustaining Force in Near-Hovering Flight. *Science.* 152:1263-1266.
- BIRCH, J. M., and M. H. DICKINSON. 2003. The influence of wing-wake interactions on the production of aerodynamic forces in flapping flight. *J Exp Biol.* 206:2257-2272.
- BORRELL, B. J., J. A. GOLDBOGEN, and R. DUDLEY. 2005. Aquatic wing flapping at low Reynolds numbers: swimming kinematics of the Antarctic pteropod, *Clione antarctica*. *J Exp Biol.* 208:2939-2949.
- BRACKENBURY, J. 1990. Wing movements in the bush cricket *Tettigonia viridissima* and the mantis *Ameles spallanziana* during natural leaping. *J. Zool. Lond.* 220:593 -602.
- . 2004. Kinematics and hydrodynamics of swimming in the mayfly larva. *J Exp Biol.* 207:913-922.
- BRENNEN, C., and H. WINET. 1977. Fluid Mechanics of Propulsion by Cilia and Flagella. *Annual Review of Fluid Mechanics.* 9:339-398.
- BRENNEN, C. E. 1982. A Review of Added Mass and Fluid Inertial Forces. Final Report, Apr.-Nov. 1981 Brennen (CE), Sierra Madre, CA.
- BRODSKII, A. 1974. Evolution of the wing apparatus in the Ephemeroptera. *Entomol. Obozr.* 53:1-303.
- BRODSKY, A. K. 1991. Vortex Formation in the Tethered Flight of the Peacock Butterfly *Inachis io* L. (Lepidoptera, Nymphalidae) and some Aspects of Insect Flight Evolution. *J Exp Biol.* 161:77-95.
- CANNAS, M., J. SCHAEFER, P. DOMENICI, and J. F. STEFFENSEN. 2006. Gait transition and oxygen consumption in swimming striped surfperch *Embiotoca lateralis* Agassiz. *Journal of Fish Biology.* 69:1612-1625.
- CHILDRESS, S., and R. DUDLEY. 2004. Transition from ciliary to flapping mode in a swimming mollusc: flapping flight as a bifurcation in $Re\omega$. *Journal of Fluid Mechanics.* 498:257-288.
- COMBES, S. A., and T. L. DANIEL. 2003. Into thin air: contributions of aerodynamic and inertial-elastic forces to wing bending in the hawkmoth *Manduca sexta*. *J Exp Biol.* 206:2999-3006.

- COOTER, R. J., and P. S. BAKER. 1977. Weis-Fogh clap and fling mechanism in *Locusta*. *Nature*. 269:53-54.
- DANIEL, T. L., JORDAN, C. AND GRUNBAUM, D. 1992. Hydromechanics of swimming, p. 17 -49. *In: Mechanics of Animal Locomotion*. Springer-Verlag, Berlin.
- DANIEL, T. L., and E. MEYHOFER. 1989. Size Limits in Escape Locomotion of Caridean Shrimps. *J Exp Biol*. 143:245-265.
- DANIEL TL, W. P. 1987. Physical determinants of locomotion, p. 343-369. *In: Comparative physiology: life in water and on land*. B. Dejours P and T. C. L, Weibel ER (eds.). Liviana Press, New York.
- DAVID, E. A. 1991. Mechanics of branchial ventilation in the valviferan isopod *Idotea wosnesenskii* (Crustacea). *Journal of Zoology*. 224:607-616.
- DENISSENKO, P., S. LUKASCHUK, and T. BREITHAUPT. 2007. The flow generated by an active olfactory system of the red swamp crayfish. *J Exp Biol*. 210:4083-4091.
- DICKINSON, M. H., and K. G. GOTZ. 1993. Unsteady Aerodynamic Performance of Model Wings at Low Reynolds Numbers. *J Exp Biol*. 174:45-64.
- DICKINSON, M. H., F.-O. LEHMANN, and S. P. SANE. 1999. Wing Rotation and the Aerodynamic Basis of Insect Flight. *Science*. 284:1954-1960.
- DRUCKER, E. G. 1996. The Use of Gait Transition Speed in Comparative Studies of Fish Locomotion. *Amer. Zool*. 36:555-566.
- DRUCKER, E. G., and G. V. LAUDER. 1999. Locomotor forces on a swimming fish: three-dimensional vortex wake dynamics quantified using digital particle image velocimetry. *Journal of Experimental Biology*. 202:2393-2412.
- EASTHAM, L. 1932. Currents produced by the Gills of Mayfly Nymphs. *Nature*. 130:58.
- . 1934. Metachronal rhythms and gill movements of the nymph of *Caenis horaria* (Ephemeroptera) in relation to water flow. *Proceedings of the Royal Society of London*. 115:30-48.
- EASTHAM, L. E. S. 1936. The Rhythmical Movements of the Gills of Nymphal *Leptophlebia marginata* (Ephemeroptera) and the Currents Produced by them in Water. *J Exp Biol*. 13:443-449.
- . 1937. The Gill Movements of Nymphal *Ecdyonorus Venosus* (Ephemeroptera) and the Currents produced by them in Water. *J Exp Biol*. 14:219-228.
- . 1939. Gill Movements of Nymphal *Ephemerella danica* (Ephemeroptera) and the Water Currents caused by them. *J Exp Biol*. 16:18-33.
- . 1958. The abdominal musculature of nymphal *Chloeon dipterum* L. (Insecta: Ephemeroptera) in relation to gill movement and swimming. *Proc. Zool. Soc. London* 131:279-291.
- ELLINGTON, C. P. 1984. The Aerodynamics of Hovering Insect Flight. V. A Vortex Theory. *Philosophical Transactions of the Royal Society of London. Series B, Biological Sciences*. 305:115-144.
- ENNOS, A. R. 1988. The Importance of Torsion in the Design of Insect Wings. *J Exp Biol*. 140:137-160.
- ERIKSEN, C. H., and J. E. MOEUR. 1990. Respiratory functions of motile tracheal gills in Ephemeroptera nymphs, as exemplified by *Siphonurus occidentalis* Eaton. Kluwer Academic Publishers.
- FOROUHAR, A. S., M. LIEBLING, A. HICKERSON, A. NASIRAEI-MOGHADDAM, H.-J. TSAI, J. R. HOVE, S. E. FRASER, M. E. DICKINSON, and M. GHARIB. 2006. The

- Embryonic Vertebrate Heart Tube Is a Dynamic Suction Pump. *Science*. 312:751-753.
- FUIMAN, L., and R. BATTY. 1997. What a drag it is getting cold: partitioning the physical and physiological effects of temperature on fish swimming. *J Exp Biol*. 200:1745-1755.
- FULL, R. J. 1997. Invertebrate locomotor systems, p. 853-930. *In: The handbook of comparative physiology*. Oxford University Press, Oxford.
- FUNK, D. H., J. K. JACKSON, and B. W. SWEENEY. 2006. Taxonomy and genetics of the parthenogenetic mayfly *Centroptilum triangulifer* and its sexual sister *Centroptilum alamance* (Ephemeroptera:Baetidae). *Journal of the North American Benthological Society*. 25:417-429.
- GILLIES, M. T. 1997. Gill mobility in the Baetidae (Ephemeroptera): results of a short study in Africa. *Ephemeroptera & Plecoptera: Biology-Ecology-Systematics, MTL, Fribourg*:113-116.
- GOTZ, K. G. 1987. Course-Control, Metabolism and Wing Interference During Ultralong Tethered Flight in *Drosophila Melanogaster*. *J Exp Biol*. 128:35-46.
- GRAY, J., and G. J. HANCOCK. 1955. The Propulsion of Sea-Urchin Spermatozoa. *J Exp Biol*. 32:802-814.
- HEGLUND, N. C., and C. R. TAYLOR. 1988. Speed, stride frequency and energy cost per stride: how do they change with body size and gait? *J Exp Biol*. 138:301-318.
- HEGLUND, N. C., C. R. TAYLOR, and T. A. MCMAHON. 1974. Scaling Stride Frequency and Gait to Animal Size: Mice to Horses. *Science*. 186:1112-1113.
- HORRIDGE, G. A. 1956. The Flight of Very Small Insects. *Nature*. 178:1334-1335.
- HOYT, D. F., and C. R. TAYLOR. 1981. Gait and the energetics of locomotion in horses. *Nature*. 292:239-240.
- JIANG, H., C. MENEVEAU, and T. R. OSBORN. 2002. The flow field around a freely swimming copepod in steady motion. Part II: Numerical simulation. *J. Plankton Res*. 24:191-213.
- KLUGE, N. J. 1989. The problem of the homology of the tracheal gills and paranotal processi of the mayfly larvae and wings of the insects with reference to the taxonomy and phylogeny of the order Ephemeroptera, p. 48-77. *In: Chiteniya pamyati N.A.Kholodkovskogo [Lectures in Memoriam of N.A. Kholodkovsky] Vol. 41*.
- KNUDSEN, E. I. 1973. Muscular activity underlying ventilation and swimming in the horseshoe crab, *Limulus polyphemus*. *Biol. Bull*. 144 355-367.
- KOHLHAGE, K., and J. YAGER. 1994. An Analysis of Swimming in Remipede Crustaceans. *Philosophical Transactions: Biological Sciences*. 346:213-221
- KUTASH, T. N., and D. A. CRAIG. 1998. Ontogenetic effects on locomotory gaits in nymphs of *Baetis tricaudatus* Dodds (Ephemeroptera: Baetidae). *Journal of the North American Benthological Society*. 17:475-488.
- LANDAU, L. D., and E. M. LIFSHITZ. 1987. *Course of Theoretical Physics*, p. 336-343. *In: Fluid Mechanics*. Vol. 6. Pergamon Press.
- LAUGA, E., and D. BARTOLO. 2008. No many-scallop theorem: Collective locomotion of reciprocal swimmers. *Physical Review E (Statistical, Nonlinear, and Soft Matter Physics)*. 78:030901-4.
- LEHMANN, F.-O., S. P. SANE, and M. DICKINSON. 2005. The aerodynamic effects of wing-wing interaction in flapping insect wings. *J Exp Biol*. 208:3075-3092.

- LIGHTHILL, J. 1976. Flagellar Hydrodynamics. *SIAM Review*. 18:161-230.
- LIGHTHILL, M. J. 1973. On the Weis-Fogh mechanism of lift generation. *Journal of Fluid Mechanics*. 60:1-17
- MALKIEL, E., J. SHENG, J. KATZ, and J. R. STRICKLER. 2003. The three-dimensional flow field generated by a feeding calanoid copepod measured using digital holography. *J Exp Biol*. 206:3657-3666.
- MAXWORTHY, T. 1979. Experiments on the Weis-Fogh mechanism of lift generation by insects in hovering flight. Part 1. Dynamics of the. *Journal of Fluid Mechanics Digital Archive*. 93:47-63.
- MCHENRY, M. J., E. AZIZI, and J. A. STROTHER. 2003. The hydrodynamics of locomotion at intermediate Reynolds numbers: undulatory swimming in ascidian larvae (*Botrylloides* sp.). *Journal of Experimental Biology*. 206:327-343.
- MILLER, L. A., and C. S. PESKIN. 2004. When vortices stick: an aerodynamic transition in tiny insect flight. *J Exp Biol*. 207:3073-3088.
- . 2005. A computational fluid dynamics of 'clap and fling' in the smallest insects. *J Exp Biol*. 208:195-212.
- MORTON, B. R. 1984. The generation and decay of vorticity. *Geophysical & Astrophysical Fluid Dynamics*. 28:277 - 308.
- MOTANI, R. 2002. Scaling effects in caudal fin propulsion and the speed of ichthyosaurs. *Nature*. 415:309-312.
- NAUEN, J. C., and R. E. SHADWICK. 2001. The dynamics and scaling of force production during the tail-flip escape response of the California spiny lobster *Panulirus interruptus*. *J Exp Biol*. 204:1817-1830.
- POELMA, C., W. DICKSON, and M. DICKINSON. 2006. Time-resolved reconstruction of the full velocity field around a dynamically-scaled flapping wing. *Experiments in Fluids*. 41:213-225.
- PURCELL, E. M. 1977. Life at low Reynolds number. *American Journal of Physics*. 45:3-11
- RAYNER, J. M. V. 1979. A new approach to animal flight mechanics. *Journal of Experimental Biology*. 80:17-54.
- RIISGÅRD, H. U., and A. GOLDSOHN. 1997. Minimal scaling of the lophophore filter-pump in ectoprocts (Bryozoa) excludes physiological regulation of filtration rate to nutritional needs. Test of hypothesis. *Mar. Ecol. Prog. Ser.* . 156:109-120.
- SANE, S. P., and M. H. DICKINSON. 2002. The aerodynamic effects of wing rotation and a revised quasi-steady model of flapping flight. *J Exp Biol*. 205:1087-1096.
- SENENIG, A. T., J. W. SHULTZ, and K. KIGER. in press 2009. The rowing-to-flapping transition: ontogenetic changes in gill-plate kinematics in the nymphal mayfly *Centroptilum triangulifer* (Ephemeroptera, Baetidae). *Biological Journal of the Linnean Society*.
- SHAPIRO, A. H. 1961. *Shape and flow: The fluid dynamics of drag*. Anchor Books.
- SOMPS, C., and M. LUTTGES. 1985. Dragonfly Flight: Novel Uses of Unsteady Separated Flows. *Science*. 228:1326-1329.
- SPEEDING, G. R., and T. MAXWORTHY. 1986. The generation of circulation and lift in a rigid two-dimensional fling. *Journal of Fluid Mechanics*. 165:247-272

- SPEDDING, G. R., M. ROSEN, and A. HEDENSTROM. 2003. A family of vortex wakes generated by a thrush nightingale in free flight in a wind tunnel over its entire natural range of flight speeds. *J Exp Biol.* 206:2313-2344.
- STRATHMANN, R. R. 1993. Hypotheses on the Origins of Marine Larvae. *Annual Review of Ecology and Systematics.* 24:89-117.
- SWEENEY, B., D. FUNK, and L. STANDLEY. 1992. Use of the stream mayfly *Cloeon triangulifer* as a bioassay organism : life history response and body burden following exposure to technical chlordane. *Environmental toxicology and chemistry.* 12:115-125.
- TAYLOR, G. 1951. Analysis of the Swimming of Microscopic Organisms. *Proceedings of the Royal Society of London. Series A, Mathematical and Physical Sciences (1934-1990).* 209:447-461.
- THOMPSON, D. A. W. 1917. *On growth and form.* Cambridge University Press, Cambridge.
- TONY, S. Y., L. ERIC, and A. E. HOSOI. 2006. Experimental investigations of elastic tail propulsion at low Reynolds number. *Physics of Fluids.* 18:091701.
- TYTELL, E. D. 2004. The hydrodynamics of eel swimming II. Effect of swimming speed. *J Exp Biol.* 207:3265-3279.
- USHERWOOD, J. R., and C. P. ELLINGTON. 2002. The aerodynamics of revolving wings I. Model hawkmoth wings. *J Exp Biol.* 205:1547-1564.
- USHERWOOD, J. R., and F.-O. LEHMANN. 2008. Phasing of dragonfly wings can improve aerodynamic efficiency by removing swirl. *Journal of The Royal Society Interface.* 5:1303-1307.
- VAN DUREN, L. A., and J. J. VIDELER. 2003. Escape from viscosity: the kinematics and hydrodynamics of copepod foraging and escape swimming. *Journal of Experimental Biology.* 206:269-279.
- VIDELER, J. J., and D. WEIHS. 1982. Energetic advantages of burst-and-coast swimming of fish at high speeds. *Journal of Experimental Biology.* 97:169-178.
- VOGEL, S. 1992. *Vital circuits: on pumps, pipes, and the workings of circulatory systems.* Oxford University, Oxford.
- WALKER, J. A. 2002. Functional Morphology and Virtual Models: Physical Constraints on the Design of Oscillating Wings, Fins, Legs, and Feet at Intermediate Reynolds Numbers. *Integr. Comp. Biol.* 42:232-242.
- WALKER, J. A., and M. W. WESTNEAT. 2002. Kinematics, Dynamics, and Energetics of Rowing and Flapping Propulsion in Fishes. *Integr. Comp. Biol.* 42:1032-1043.
- WANG, Z. J. 2000. Vortex shedding and frequency selection in flapping flight. *Journal of Fluid Mechanics.* 410:323-341.
- WEBB, P. W., and D. WEIHS. 1986. Functional Locomotor Morphology of Early Life History Stages of Fishes. *Transactions of the American Fisheries Society.* 115:115-127.
- WEIHS, D. 1974. Energetic advantages of burst swimming of fish. *Journal of Theoretical Biology.* 48:215-229.
- WEIS-FOGH, T. 1973. Quick Estimates of Flight Fitness in Hovering Animals, Including Novel Mechanisms for Lift Production. *J Exp Biol.* 59:169-230.

- WESTNEAT, M., and J. WALKER. 1997. Motor patterns of labriform locomotion: kinematic and electromyographic analysis of pectoral fin swimming in the labrid fish *Gomphosus varius*. *J Exp Biol.* 200:1881-1893.
- WIGGINS, C. H., and R. E. GOLDSTEIN. 1998. Flexive and Propulsive Dynamics of Elastica at Low Reynolds Number. *Physical Review Letters.* 80:3879.
- WILLIAMS, T. A. 1994a. Locomotion in Developing *Artemia* Larvae: Mechanical Analysis of Antennal Propulsors Based on Large-Scale Physical Models, p. 156-163. Vol. 187. MBL.
- . 1994b. A Model of Rowing Propulsion and the Ontogeny of Locomotion in *Artemia* Larvae, p. 164-173. Vol. 187. MBL.
- WINGFIELD, C. A. 1939. The Function of the Gills of Mayfly Nymphs from Different Habitats. *Journal of Experimental Biology.* 16:363-373.
- WOMERSLEY, J. R. 1955. Method for the calculation of velocity, rate flow, and viscous drag in arteries when the pressure gradient is known. *Journal of Physiology.* 127:553-563.
- WOOTTON, R. J. 1981. Support and deformability in insect wings. *J. Zool., Lond.* 193:447-468.
- . 1999. Invertebrate paraxial locomotory appendages: design, deformation and control. *J Exp Biol.* 202:3333-3345.
- WU, J. 1981 Theory for aerodynamic force and moment in viscous flows. *AIAA J.* 19:432 -441.